



**JOHANNES KEPLER
UNIVERSITY LINZ**

Submitted by
**Dipl.-Ing.
Simon Gerhard Hubmer,
Bakk. Techn.**

Submitted at
**Doktoratskolleg
"Computational
Mathematics"**

Supervisor and
First Examiner
**Univ.-Prof. Dr.
Ronny Ramlau**

Second Examiner
**Univ.-Prof. Dr.
Bernd Hofmann**

March 2018

Fast Gradient-Based Iterative Regularization Methods for Nonlinear Ill-Posed Problems - Theory and Applications



Doctoral Thesis
to obtain the academic degree of
Doktor der technischen Wissenschaften
in the Doctoral Program
Technische Wissenschaften

**JOHANNES KEPLER
UNIVERSITY LINZ**
Altenbergerstraße 69
4040 Linz, Österreich
www.jku.at
DVR 0093696

Abstract

In this thesis, we investigate a class of fast gradient-based iterative regularization methods for nonlinear Inverse and Ill-Posed Problems based on Landweber iteration and Nesterov's acceleration scheme. These so-called Two Point Gradient (TPG) methods have been found to be very useful in practical applications, since they are both easy to implement and lead to a great speedup compared to standard gradient-based methods. While methods utilizing second-order information, which are known for their fast convergence, often become infeasible when dealing with large datasets, gradient-based methods are usually more flexible and able to deal with large datasets, at the disadvantage of requiring a large number of iterations. TPG methods have the potential to bridge the apparent gap between these two classes of methods, being both fast, flexible, and able to deal with large datasets, which are important requirements for any iterative regularization method used for solving inverse problems.

This thesis provides a convergence analysis of TPG methods under the common assumption of a tangential cone condition, and covers some well-known choices of commonly used stepsizes. Furthermore, a convergence analysis with the tangential cone condition being replaced by a local convexity assumption more natural to Nesterov's original acceleration idea is performed. These results provide the first successful convergence analysis for TPG methods for the solution of nonlinear ill-posed problems.

Apart from these theoretical results, this thesis presents a number of numerical examples showing the usefulness of TPG methods in practical applications. In a number of academic examples, the assumptions required for convergence are considered in detail, and precise comparisons between several TPG methods and standard gradient-based methods are performed. Afterwards, TPG methods are applied to two problems arising in Medical Imaging. The first of these two problems is the imaging technique of Single Photon Emission Computed Tomography (SPECT), where TPG methods are shown to lead to a large speedup in the reconstruction process. The second problem concerns Magnetic Resonance Advection Imaging (MRAI), which is a novel imaging technique for mapping the pulse wave velocity in brain vessel from Magnetic Resonance Imaging (MRI) measurements. For this problem, for which a precise modelling is performed, TPG methods are essential due to the large datasets involved.

Zusammenfassung

In dieser Arbeit betrachten wir eine Klasse von Gradienten-Basierten Iterativen Methoden für Inverse und Schlecht-Gestellte Probleme basierend auf der Landweber Iteration und Nesterov's Beschleunigungsschema. Diese sogenannten Zwei-Punkt Gradienten (TPG) Methoden sind sehr nützlich in praktischen Anwendungen, da sie einfach zu implementieren sind und zu einer großen Beschleunigung gegenüber Gradienten-Basierten Standardverfahren führen. Während Methoden zweiter Ordnung, die für ihre schnelle Konvergenz bekannt sind, bei großen Datenmengen oft undurchführbar werden, sind Gradienten-Basierte Methoden normalerweise flexibler und erlauben auch die Behandlung großer Datensätze, mit dem Nachteil, dass sie eine größere Anzahl an Iterationen benötigen. TPG Methoden haben das Potential, die Lücke zwischen diesen beiden Klassen von Methoden zu füllen, da sie schnell und flexibel sind und mit großen Datensätzen arbeiten können, was wichtige Voraussetzungen für alle Iterative Regularisierungsverfahren für Inverse Probleme sind.

Diese Arbeit beinhaltet eine Konvergenzanalyse von TPG Methoden unter der Standardannahme einer Tangentialkegel-Bedingung, und umfasst einige bekannte Fälle von oft benutzten Schrittweiten. Darüberhinaus beinhaltet diese Arbeit eine Konvergenzanalyse, bei der die Tangentialkegel-Bedingung durch eine Lokale Konvexitätsannahme ersetzt wird. Diese Resultate stellen die erste erfolgreiche Konvergenzanalyse von TPG Methoden für die Lösung von nichtlinearen schlecht-gestellten Problemen dar.

Neben diesen theoretischen Resultaten beinhaltet diese Arbeit auch eine Reihe von numerischen Beispielen, welche den Nutzen von TPG Methoden in praktischen Anwendungen verdeutlichen. In einer Reihe von akademischen Beispielen werden die Annahmen der Konvergenzanalyse im Detail betrachtet, und genau Vergleiche zwischen verschiedenen TPG Methoden und Gradienten-Basierten Standardmethoden durchgeführt. Anschliessend werden TPG Methoden auf zwei Probleme angewendet, die in der medizinischen Bildbearbeitung auftreten. Das erste dieser zwei Probleme ist das bildgebende Verfahren der Einzelphotonen-Emissionscomputertomographie (SPECT), für das TPG Methoden zu einer großen Beschleunigung im Rekonstruktionsprozess führen. Das zweite Problem behandelt Magnet Resonanz Advektions Tomographie (MRAI), das ein neues bildgebendes Verfahren zur Bestimmung der Pulswellen Geschwindigkeit in Blutgefäßen im Gehirn durch Magnet Resonanz Tomographie (MRI) Daten ist. Für dieses Problem, für das eine genaue Modellierung durchgeführt wird, sind TPG Methoden essentiell, aufgrund der dabei auftretenden großen Datensätze.

Acknowledgments

First of all, I would like to thank my supervisor Prof. Ronny Ramlau, for everything he has done for me so far, be it the opportunity to work under his expert guidance, the interesting topics he suggested, the fruitful discussions we had, as well as the freedom he gave me to pursue my own ideas and his interest in where they eventually led. For all he did for me and allowed me to do, and especially for taking care of many things in the background of which I can only be partly aware, I am most grateful to him.

Next, I would like to thank the supervisor of my master thesis, Prof. Andreas Neubauer, for all the discussions we had over the years, for his valuable support especially during the early stages of my PhD, and for continuing to answer all of my many questions.

Furthermore, I would like to thank Prof. Bernd Hofmann for kindly agreeing to review this thesis and Prof. Per Christian Hansen for allowing me to have a productive and joyful two months stay with him at the Technical University of Denmark.

My PhD would not have been possible without the Doctoral Program “Computational Mathematics” (W1214), sponsored by the Austrian Science Fund (FWF). Apart from financing my PhD, this institute under the former and current speakers Prof. Peter Paule and Dr. Veronika Pillwein, respectively, provided the perfect academic and warm-hearted environment for fruitful work, for which I am very thankful. Of my many colleagues there, I would especially like to thank Antonio Jiménez Pastor, MSc, for many interesting interdisciplinary discussions, lunch and coffee breaks.

Being under the supervision of Prof. Ramlau, I naturally had lots of contact with the many cheerful and open-hearted members of the Industrial Mathematics Institute, to whom I hereby send my many thanks. I would especially like to thank Dr. Stefan Kindermann for many an interesting exchange of ideas on more than one occasion.

My gratitude also goes to all my study and work colleagues, especially to Dr. Andreas Thalhammer and DI Mario Neumüller, and to the many people inhabiting Science Park 2, and my office colleagues DI Katharina Rafetseder and Agnes Seiler, MSc.

Finally, I would like to express my deepest gratitude to all my family and friends.

Simon Hubmer
Linz, March 2018

Contents

1	Introduction	1
1.1	Motivation	1
1.2	Organization of the Thesis	2
2	Theoretical Background	3
2.1	Nonlinear Ill-Posed Problems	3
2.2	Tikhonov Regularization	4
2.3	Iterative Regularization Methods	4
2.4	Nesterov's Acceleration Scheme	7
2.5	Further Topics	9
I	Analysis of TPG Methods	11
3	Convergence under a Tangential Cone Condition	12
3.1	Convergence Analysis I	12
3.2	Examples of TPG methods based on the Steepest Descent and the Minimal Error stepsize	24
4	Convergence under a Local Convexity Condition	33
4.1	Convergence Analysis II	34
4.2	Convergence Analysis III	47
4.3	Strong Convexity and Nonlinearity Conditions	49
II	Application of TPG Methods	51
5	Application and Comparison of General TPG Methods	52
5.1	Nonlinear Hammerstein Operator	52
5.2	Single Photon Emission Computed Tomography	55
6	Applications of Specific TPG Methods	61
6.1	Nonlinear Diagonal Operator	61
6.2	Auto-Convolution Problem	64

6.3	Magnetic Resonance Advection Imaging	68
6.3.1	Medical Background	69
6.3.2	Mathematical Model	71
6.3.3	Discretization	72
6.3.4	Solution Approach	82
6.3.5	Numerical Results	84
6.3.6	Discussion of Results	95
6.4	Further Examples	97
7	Conclusion and Outlook	99
7.1	Conclusion	99
7.2	Outlook	100
	List of Figures	102
	List of Tables	103
	Curriculum Vitae	111

Chapter 1

Introduction

1.1 Motivation

Many important problems of practical significance in science and industry fall within the area of *Inverse Problems*. In general terms, this field can be described as being concerned with finding causes for observed effects from often noisy or incomplete data. Popular examples of inverse problems are prominent in medicine, especially in the various forms of tomographic imaging techniques, where the aim is to take a look “inside” an object, or part of a body, without damaging or destroying it. Well known medical imaging techniques include for example *Magnetic Resonance Imaging (MRI)* or *Computerized Tomography (CT)*, among many others. The basic principles of tomography also find application in other areas of science, for example in *Atmospheric Tomography*, used to enhance the imaging quality of ground based telescopes, as well as in non-destructive testing of materials or seismic imaging.

A multitude of reconstruction techniques exist for solving the various inverse problems considered today. In general, those techniques can be divided into variational and iterative methods. While for the successful application of variational methods, by far the most prominent of which being *Tikhonov regularization*, iterative optimization methods are required as well, the approach of directly using so-called *iterative regularization methods* has a number of advantages, especially in the case of large scale inverse problems, which are becoming more and more commonplace in recent years.

Iterative regularization methods divide quite naturally into two main classes, on the one hand, so-called *first-order* or *gradient-based methods* such as the well-known *Landweber iteration* and its various variants and, on the other hand, *second-order methods* such as the *Levenberg-Marquardt* or the *iteratively regularized Gauss-Newton method*. While second-order methods are known to require much less iterations than gradient-based methods to arrive at suitable reconstructions, this advantage is often lost in practise in the case of large datasets, for which second-order methods are often at a disadvantage or even become infeasible. Furthermore, the convergence analysis of second-order methods usually requires much stronger assumptions than the analysis

of gradient-based methods. On the other hand, gradient-based methods, which are known for their simplicity, ease of implementation, and capacity to deal with large datasets, often require too many iterations to be practically feasible as well.

To deal with this apparent gap, various strategies have been proposed so far. On the one hand, there are ways to improve the feasibility of second-order methods by using certain *inexact Newton methods*, while on the other hand, there are acceleration techniques to speed up first-order methods. Unfortunately, many of those techniques developed for the linear case, like the ν -methods of Brakhage, do not readily translate to the nonlinear case, while other methods, although working well in practise, have as of yet no proofs of convergence. One acceleration technique giving very promising results in practise is *Nesterov's acceleration strategy*, which has a long tradition of both analysis and application for solving convex, well-posed optimization problems and also forms the basis of the well-known FISTA algorithm. Being very intuitive and exceedingly simple to implement, this technique has already been successfully employed in solving both linear and nonlinear inverse problems, even though so far only the linear case has been theoretically investigated, and this only quite recently.

Therefore, in this thesis, we investigate some accelerated gradient-based methods based on Nesterov's acceleration strategy, proving convergence under various standard assumptions as well as providing a number of applications showing the usefulness of these methods in practise.

1.2 Organization of the Thesis

This thesis, which is based on and uses parts of our work from [37–39], is structured as follows. First, we provide some important mathematical background in the theory of nonlinear Inverse Problems (Chapter 2), focusing especially on iterative regularization methods. Following this, in Part I we provide a convergence analysis of the considered methods under a standard tangential cone condition (Chapter 3) and a local convexity assumption (Chapter 4). Afterwards, in Part II we provide a number of applications of general TPG methods on examples of a Hammerstein operator and a problem from Single Photon Emission Computed Tomography (Chapter 5) and of specific TPG methods on examples of a nonlinear diagonal operator, an auto-convolution problem, and the parameter estimation problem of Magnetic Resonance Advection Imaging (Chapter 6). Finally, we provide a conclusion and a short outlook (Chapter 7).

Chapter 2

Theoretical Background

In this chapter, we provide the necessary mathematical background and context required for this thesis. After a short general introduction into the field of nonlinear Inverse and Ill-Posed Problems, we present various ways of solving them, focusing especially on iterative regularization methods of relevance to this thesis. Furthermore, we present some important results on Nesterov's accelerated gradient method for well-posed convex minimization problems. This chapter is mainly based on the well-known monographs [21, 26, 46, 53, 73] and the research article [3].

2.1 Nonlinear Ill-Posed Problems

In this section, we introduce the general form of nonlinear inverse problems considered throughout this thesis. For this, we consider the general operator equation

$$F(x) = y, \quad (2.1)$$

where $F : \mathcal{D}(F) \subset \mathcal{X} \rightarrow \mathcal{Y}$ is a continuously Fréchet-differentiable, nonlinear operator between real Hilbert spaces \mathcal{X} and \mathcal{Y} . The general goal in Inverse Problems is to recover a solution x_* of (2.1), where instead of the true data y only noisy measurement data y^δ are given. A common assumption on the noisy data y^δ which we assume to hold throughout this thesis is that

$$\|y - y^\delta\| \leq \delta, \quad (2.2)$$

where δ denotes the *noise level*. Such problems as these are usually ill-posed in the sense of Hadamard [28], since either one or more of the following well-posedness criteria are violated:

- For every right-hand side y there exists a solution of (2.1).
- For every right-hand side y the solution of (2.1) is unique.
- The solution of (2.1) depends continuously on the data y .

While all three of the above criteria are important, violation of the third condition usually leads to the most severe problems, since it implies that arbitrarily small changes in the data can lead to arbitrarily large changes in the reconstructions. In order to counter this instability issue, one has to employ so-called *regularization methods* to obtain stable reconstructions of the sought for solutions. These methods can in general be divided into the two main classes of *variational* and *iterative regularization methods*, the two most prominent examples of those classes being *Tikhonov regularization* and *Landweber iteration*, respectively.

2.2 Tikhonov Regularization

By far the most prominent regularization method is the so-called *Tikhonov* or *Tikhonov-Phillips regularization*. Here, one attempts to approximate an x_0 -*minimum-norm solution* x^\dagger of (2.1), defined by

$$x^\dagger = \arg \min_{x \in \mathcal{D}(F)} \{ \|x - x_0\| \mid F(x) = y \} ,$$

through minimizing the functional

$$\mathcal{T}_\alpha^\delta(x) := \|F(x) - y^\delta\|^2 + \alpha \|x - x_0\|^2 , \quad (2.3)$$

where α is a suitably chosen regularization parameter. Under very mild assumptions on F , it can be shown that the minimizers of $\mathcal{T}_\alpha^\delta$, usually denoted by x_α^δ , converge subsequentially to a minimum norm solution x^\dagger as $\delta \rightarrow 0$, given that the *regularization parameter* $\alpha = \alpha(\delta)$ and the noise level δ are coupled in an appropriate way [21], e.g.,

$$\lim_{\delta \rightarrow 0} \alpha(\delta) = \lim_{\delta \rightarrow 0} \frac{\delta^2}{\alpha(\delta)} = 0 .$$

While for linear operators $F = T$ the minimization of $\mathcal{T}_\alpha^\delta$ is straightforward, requiring only the solution of the linear equation

$$(T^*T + \alpha I)x = T^*y^\delta + \alpha x_0 ,$$

in the case of nonlinear operators F the computation of x_α^δ requires the global minimization of the then also nonlinear functional $\mathcal{T}_\alpha^\delta$. This global minimization can be very costly and difficult and is usually done using various iterative optimization algorithms, which motivates the direct application of iterative algorithms to (2.1).

2.3 Iterative Regularization Methods

One of the most well-known iterative regularization method is the so-called *Landweber iteration*, given by

$$\begin{aligned} x_{k+1}^\delta &= x_k^\delta + \omega F'(x_k^\delta)^*(y^\delta - F(x_k^\delta)) , \\ x_0^\delta &= x_0 , \end{aligned} \quad (2.4)$$

where ω is a scaling parameter and x_0 is again a given initial guess. Seen in the context of classical optimization algorithms, Landweber iteration is nothing else than the gradient descent method applied to the functional

$$\Phi^\delta(x) := \frac{1}{2} \|F(x) - y^\delta\|^2, \quad (2.5)$$

and therefore, due to the ill-posedness issue, in order to arrive at a convergent regularization method, one has to use a suitable stopping rule to terminate the iteration. A very prominent stopping rule is Morozov's *discrepancy principle*, which suggests to stop the iteration after k_* steps, where k_* is the smallest integer such that

$$\|y^\delta - F(x_{k_*}^\delta)\| \leq \tau\delta < \|y^\delta - F(x_k^\delta)\|, \quad 0 \leq k < k_*, \quad (2.6)$$

with a suitable constant $\tau > 1$. For proving convergence of Landweber iteration, strong assumptions are generally required on the underlying operator F such as the (strong) tangential cone condition

$$\|F(x) - F(\tilde{x}) - F'(x)(x - \tilde{x})\| \leq \eta \|F(x) - F(\tilde{x})\|, \quad \eta < \frac{1}{2}, \quad (2.7)$$

$$x, \tilde{x} \in \mathcal{B}_{2\rho}(x_0),$$

where $\mathcal{B}_{2\rho}(x_0)$ denotes the closed ball of radius 2ρ around x_0 . Furthermore, the scaling parameter ω needs to satisfy

$$\omega \|F'(x)\|^2 \leq 1, \quad \forall x \in \mathcal{B}_{2\rho}(x_0) \subset \mathcal{D}(F). \quad (2.8)$$

If these conditions are satisfied and τ in (2.6) is chosen such that

$$\tau > 2 \frac{1 + \eta}{1 - 2\eta}, \quad (2.9)$$

then the following convergence result can be proven (see, e.g., [46, Theorem 2.6]).

Theorem 2.3.1. *Assume that (2.7) and (2.8) are satisfied and let $k_* = k_*(\delta, y^\delta)$ be chosen according to the stopping rule (2.6), (2.9). Then the Landweber iterates $x_{k_*}^\delta$ converge to a solution of (2.1) for $\delta \rightarrow 0$. Moreover, if $\mathcal{N}(F'(x^\dagger)) \subset \mathcal{N}(F'(x))$ for all $x \in \mathcal{B}_\rho(x^\dagger)$, then $x_{k_*}^\delta$ converges to x^\dagger as $\delta \rightarrow 0$.*

Since condition (2.7) poses strong restrictions on the nonlinearity of F which are not always satisfied, attempts have been made to use weaker conditions instead [71]. For example, assuming only the weak tangential cone condition

$$\langle F(x) - F(x_*) - F'(x)(x - x_*), F(x) - F(x_*) \rangle \leq \eta \|F(x) - F(x_*)\|^2, \quad (2.10)$$

$$\forall x \in \mathcal{B}_\rho(x_0), \quad 0 < \eta < 1,$$

to hold, one can show weak convergence of the Landweber iteration [71]. Similarly, if the residual functional $\Phi^0(x)$ defined by (2.5) is (locally) convex, weak subsequential convergence of the iterates of Landweber iteration to a stationary point of Φ^0 can be

proven. Even though they both lead to convergence in the weak topology, besides some results presented in [71], the connections between the local convexity of the residual functional and the (weak) tangential cone condition remain largely unexplored. In his recent paper [47], Kindermann showed that both the local convexity of the residual functional and the weak tangential cone condition imply another condition, which he termed $NC(0, \beta > 0)$, and which is sufficient to guarantee weak subsequential convergence of the iterates.

Apart from convergence itself, the speed of convergence, in the form of convergence rates, is an important issue in Inverse Problems. For nonlinear inverse problems, source conditions of the form

$$x^\dagger - x_0 \in (F'(x^\dagger)^* F'(x^\dagger))^\mu v, \quad v \in \mathcal{N}(F'(x^\dagger))^\perp, \quad (2.11)$$

play an important role and, together with further restrictions on the nonlinearity of the operator F , often lead to order optimal results of the form

$$k_* = \mathcal{O}\left(\delta^{-\frac{2}{2\mu+1}}\right) \quad \text{and} \quad \|x_k^\delta - x^\dagger\| = \mathcal{O}\left(\delta^{\frac{2\mu}{2\mu+1}}\right). \quad (2.12)$$

These results can also be generalized to the case when instead of a constant stepsize ω one uses for example the steepest-descent stepsize

$$\omega_k^\delta := \frac{\|s_k^\delta\|^2}{\|F'(x_k^\delta) s_k^\delta\|^2},$$

or the minimal error stepsize

$$\omega_k^\delta := \frac{\|y^\delta - F(x_k^\delta)\|^2}{\|s_k^\delta\|^2},$$

where $s_k^\delta := F'(x_k^\delta)^*(y^\delta - F(x_k^\delta))$, see for example [60, 72]. This can also be generalized to a broader class of stepsizes [60].

As is well known, in general Landweber iteration is quite slow. Hence, acceleration strategies have to be used in order to speed it up in order to make it applicable in practise. Acceleration methods and their analysis for linear problems like the ν -methods can be found for example in [21] and [29]. Unfortunately, since their convergence proofs are mainly based on spectral theory, their analysis cannot be generalized to nonlinear problems immediately. However, there are some acceleration strategies for Landweber iteration for nonlinear ill-posed problems, for example Landweber iteration in Hilbert scales [58] or approximate Landweber methods [65].

As an alternative to (accelerated) Landweber-type methods, one can use second order iterative methods for solving (2.1), such as the Levenberg-Marquardt method [30, 43]

$$x_{k+1}^\delta = x_k^\delta + (F'(x_k^\delta)^* F'(x_k^\delta) + \alpha_k I)^{-1} F'(x_k^\delta)^*(y^\delta - F(x_k^\delta)), \quad (2.13)$$

or the iteratively regularized Gauss-Newton method [9, 45]

$$x_{k+1}^\delta = x_k^\delta + (F'(x_k^\delta)^* F'(x_k^\delta) + \alpha_k I)^{-1} (F'(x_k^\delta)^* (y^\delta - F(x_k^\delta)) + \alpha_k (x_0 - x_k^\delta)). \quad (2.14)$$

The advantage of those methods is that they require much less iterations to meet their respective stopping criteria compared to Landweber iteration or the steepest descent method. However, each update step of those iterations can take considerably longer than one step of Landweber iteration, due to the fact that in both cases a linear system involving the operator

$$F'(x_k^\delta)^* F'(x_k^\delta) + \alpha_k I,$$

has to be solved. In practical applications, this usually means that a huge linear system of equations has to be solved, which often proves to be costly, if not infeasible, even if those systems are only solved approximately for example with the conjugate gradient method, which gives rise to so-called *inexact Newton methods* [68]. Hence, accelerated Landweber type methods avoiding this drawback are desirable in practise.

2.4 Nesterov's Acceleration Scheme

In case that the residual functional $\Phi^\delta(x)$ is locally convex, one can think of using methods from convex optimization to minimize $\Phi^\delta(x)$, instead of using the gradient method like in Landweber iteration. One of those methods, which works remarkably well for nonlinear, convex and well-posed optimization problems of the form

$$\min\{\Phi(x) \mid x \in \mathcal{X}\}, \quad (2.15)$$

was first introduced by Nesterov in [57] and is given by

$$\begin{aligned} z_k &= x_k + \frac{k-1}{k+\alpha-1} (x_k - x_{k-1}), \\ x_{k+1} &= z_k - \omega (\nabla \Phi(z_k)), \end{aligned} \quad (2.16)$$

where again ω is a given scaling parameter and $\alpha \geq 3$ (with $\alpha = 3$ being common practise). This so-called *Nesterov acceleration scheme* is of particular interest, since not only is it extremely easy to implement, but Nesterov himself was also able to prove that it generates a sequence of iterates x_k for which there holds

$$\|\Phi(x_k) - \Phi(x_*)\| = \mathcal{O}(k^{-2}), \quad (2.17)$$

where x_* is any minimizer of (2.15). This is a big improvement over the classical rate $\mathcal{O}(k^{-1})$. The even further improved rate $\mathcal{O}(k^{-2})$ for $\alpha > 3$ was recently proven in [3] and it is known that the iterates x_k converge weakly to a minimizer of (2.15). Furthermore, Nesterov's acceleration scheme can also be used to solve compound optimization problems of the form

$$\min\{\Phi(x) + \Psi(x) \mid x \in \mathcal{X}\}, \quad (2.18)$$

where both $\Phi(x)$ and $\Psi(x)$ are convex functionals, and is in this case given by

$$\begin{aligned} z_k &= x_k + \frac{k-1}{k+\alpha-1}(x_k - x_{k-1}), \\ x_{k+1} &= \text{prox}_{\omega\Psi}(z_k - \omega(\nabla\Phi(z_k))), \end{aligned} \quad (2.19)$$

where the proximal operator $\text{prox}_{\omega\Psi}(\cdot)$ is defined by

$$\text{prox}_{\omega\Psi}(x) := \arg \min_u \left\{ \omega\Psi(u) + \frac{1}{2} \|x - u\|^2 \right\}. \quad (2.20)$$

If in addition to being convex, Ψ is also proper and lower-semicontinuous and Φ is continuously Fréchet differentiable with a Lipschitz continuous gradient, then it was again shown in [3] that the sequence defined by (2.19) satisfies

$$\|(\Phi - \Psi)(x_k) - (\Phi - \Psi)(x_*)\| = \mathcal{O}(k^{-2}), \quad (2.21)$$

or even $\mathcal{O}(k^{-2})$ if $\alpha > 3$, which is again much faster than ordinary gradient-based methods for minimizing (2.18). This accelerating property was exploited in the highly successful FISTA algorithm [7], designed for the fast solution of linear ill-posed problems with sparsity constraints. Since for linear operators, the residual functional Φ^δ is globally convex, minimizing the resulting Tikhonov functional (2.3) exactly fits into the category of minimization problems considered in (2.18).

Motivated by the above considerations, one can think of applying Nesterov's acceleration scheme (2.16) to the residual functional Φ^δ , which leads to the algorithm

$$\begin{aligned} z_k^\delta &= x_k^\delta + \frac{k-1}{k+\alpha-1}(x_k^\delta - x_{k-1}^\delta), \\ x_{k+1}^\delta &= z_k^\delta + \omega F'(z_k^\delta)^*(y^\delta - F(z_k^\delta)), \\ x_0^\delta &= x_{-1}^\delta = x_0, \end{aligned} \quad (2.22)$$

which in this form was first proposed in [44] to accelerate the Landweber iteration for solving (nonlinear) ill-posed problems. Although no convergence analysis for (2.22) could be given, the numerical examples presented in [44] clearly show its usefulness and acceleration effect. Motivated by this, a slightly modified version of (2.22) promoting sparsity was used in [37] and one of the authors of that paper went on to show [61] that for linear operators $F = T$ and given the source condition $x^\dagger \in \mathcal{R}((T^*T)^\mu)$, using an a priori stopping rule one gets for $0 \leq \mu \leq 1/2$ that

$$k_* = \mathcal{O}(\delta^{-\frac{1}{2\mu+1}}), \quad \text{and} \quad \|x_{k_*}^\delta - x^\delta\| = \mathcal{O}\left(\delta^{\frac{2\mu}{2\mu+1}}\right),$$

while for $\mu > 1/2$,

$$k_* = \mathcal{O}(\delta^{-\frac{2}{2\mu+3}}), \quad \text{and} \quad \|x_{k_*}^\delta - x^\delta\| = \mathcal{O}\left(\delta^{\frac{2\mu+1}{2\mu+3}}\right).$$

Similar results can also be obtained if the iteration is stopped by the discrepancy principle. This should be compared to the results for classical Landweber iteration (2.12), which shows that asymptotically much less iterations are required.

The above considerations strongly suggest to consider the following generalization of Nesterov's acceleration scheme, termed *Two-Point Gradient (TPG) methods*:

$$\begin{aligned} z_k^\delta &= x_k^\delta + \lambda_k^\delta(x_k^\delta - x_{k-1}^\delta), \\ x_{k+1}^\delta &= z_k^\delta + \alpha_k^\delta s_k^\delta, \quad s_k^\delta := F'(z_k^\delta)^*(y^\delta - F(z_k^\delta)), \\ x_0^\delta &= x_{-1}^\delta = x_0, \end{aligned} \quad (2.23)$$

which we analyse in detail in this thesis. Note that (2.23) can also be rewritten in terms of z_k^δ , leading to

$$\begin{aligned} z_{k+1}^\delta &= (1 + \lambda_{k+1}^\delta)(z_k^\delta + \alpha_k^\delta s_k^\delta) - \lambda_{k+1}^\delta(z_{k-1}^\delta + \alpha_{k-1}^\delta s_{k-1}^\delta) \\ &= z_k^\delta + \lambda_{k+1}^\delta(z_k^\delta - z_{k-1}^\delta) + (1 + \lambda_{k+1}^\delta)\alpha_k^\delta s_k^\delta - \lambda_{k+1}^\delta\alpha_{k-1}^\delta s_{k-1}^\delta, \end{aligned} \quad (2.24)$$

which structurally differs from the iteration methods considered by Scherzer in [72] by the additional term $\lambda_{k+1}^\delta(z_k^\delta - z_{k-1}^\delta)$. However, many of his ideas and arguments for proving convergence of those methods were re-used in the proofs in Chapter 3.

2.5 Further Topics

The above discussion is obviously far away from giving a comprehensive overview of the field of Inverse Problems as a whole. Hence, although not strictly necessary for the understanding of the topics considered in this thesis, we devote this section to indicate a number of extensions of the theory as well as some alternative lines of investigations and interesting topics in connection with Inverse Problems.

First of all, besides variational and iterative regularization methods, there also exists a number of different solution methods fitting into neither of these two categories. Among those are for example certain spectral theory based methods like the truncated singular value decomposition, or the method of the approximate inverse [53] for linear problems, as well as derivative free or asymptotic methods for general (non-linear) problems. Another popular but problem dependent approach is the use of explicit solution formulas such as filtered back-projection employed in tomography or the method of complex geometric optics (CGO) solutions, which is for example used in Electrical Impedance Tomography (EIT).

Especially in connection with explicit solution formulas, questions of existence and uniqueness of solutions, identifiability of parameters, and stability estimates form an important branch of the field of Inverse Problems. There is a rich theory in connection with these topics for parameter identification problems with PDE models [41], where often so-called Carleman estimates [48] are used for addressing the uniqueness question.

On the technical side, the extension of regularization theory from the Hilbert space to the Banach space setting has been an important topic in recent years [73, 74]. For example, instead of classical Tikhonov regularization (2.3), one can consider

$$\min_{x \in \mathcal{X}} \|F(x) - y^\delta\|_Y^p + \alpha \mathcal{R}(u), \quad (2.25)$$

where \mathcal{R} is a general regularization functional and \mathcal{X}, \mathcal{Y} are Banach spaces in this case. Under general assumptions, the convergence analysis for classical Tikhonov regularization can be carried over to the above setting. This allows one to work for example in L^p spaces for $1 \leq p \leq \infty$, where however the interesting border cases L^1 and L^∞ are still not satisfactorily analysed due to non-reflexivity and other technical difficulties. It is also possible to prove convergence rates in the Banach space setting, which are usually obtained in the so-called Bregman distance

$$D_{\mathcal{R}}(x, \tilde{x}) := \mathcal{R}(\tilde{x}) - \mathcal{R}(x) - \mathcal{R}'(x, \tilde{x} - x),$$

where $\mathcal{R}'(x, \tilde{x} - x)$ denotes the one-sided directional derivative of \mathcal{R} at x in the direction $\tilde{x} - x$. For this, one uses generalizations of the source condition (2.11) in the form of variational inequalities like

$$\langle \xi^*, x^\dagger - x \rangle_{\mathcal{X}^*, \mathcal{X}} \leq \beta_1 D_{\xi^*}(x, x^\dagger) + \beta_2 \|F(x) - F(x^\dagger)\|, \quad (2.26)$$

where β_1 and β_2 are suitable constants and $\xi^* \in \partial\mathcal{R}(x^\dagger)$, i.e., is an element of the subdifferential of \mathcal{R} at x^\dagger . If for example $\alpha(\delta) \sim \delta^{1-\varepsilon}$ is chosen in (2.25), then it can be shown that for the corresponding minimizers x_α^δ there holds

$$D_{\xi^*}(x_\alpha^\delta, x^\dagger) = \mathcal{O}(\delta^{1-\varepsilon}), \quad \|F(x_\alpha^\delta) - y^\delta\| = \mathcal{O}(\delta).$$

Also iterative regularization methods can be transferred to the Banach space setting [74]. For example, an equivalent for Landweber iteration in Banach spaces is given by

$$x_{k+1}^\delta = J_{q^*}^{\mathcal{X}^*} \left(J_q^{\mathcal{X}}(x_k^\delta) - \mu_k F'(x_k^\delta)^* j_p^{\mathcal{Y}}(F(x_k^\delta) - y^\delta) \right),$$

where here $F'(x)^*$ denotes the Banach space adjoint of $F'(x)$, the functionals $J_{q^*}^{\mathcal{X}^*}, J_q^{\mathcal{X}}$ are (set-valued) duality mappings and $j_p^{\mathcal{Y}}$ is a singled valued selection of the duality functional $J_p^{\mathcal{Y}}$. For this method, convergence under suitable assumptions, most notably (a Banach space generalization of) the tangential cone condition (2.7), can be shown, and these results can be extended to second-order methods as well.

Important special cases of regularization in Banach spaces include for example bounded variation (BV) and total variation (TV) regularization, as well as regularization in ℓ^p spaces. Although those cases can be fit into the Banach space setting by for example by using the BV, TV, or ℓ^p norm for $\mathcal{R}(x)$ in (2.25), respectively, special theory has been developed for these cases due to their peculiarities and practical importance. Especially ℓ^p regularization for small p , which is used to promote sparsity in regularized solutions, has attracted lots of attention (see for example [14, 66, 67]).

As the last of the many further possible topics in Inverse Problems presented here, we mention that attempts have been made to further generalize the source conditions (2.11) and (2.26) using the concept of index functions, which leads to the concept of generalized source conditions and includes the important special case of logarithmic source conditions used for severely ill-posed problems. The concept of variational inequalities mentioned above, as well as approximate source conditions [35] are also important theoretical developments in this research direction.

Part I

Analysis of TPG Methods

Chapter 3

Convergence under a Tangential Cone Condition

In this chapter, which is mainly based on [38], we perform a convergence analysis of the TPG methods (2.23), i.e.,

$$\begin{aligned} z_k^\delta &= x_k^\delta + \lambda_k^\delta (x_k^\delta - x_{k-1}^\delta), \\ x_{k+1}^\delta &= z_k^\delta + \alpha_k^\delta s_k^\delta, \quad s_k^\delta := F'(z_k^\delta)^*(y^\delta - F(z_k^\delta)), \\ x_0^\delta &= x_{-1}^\delta = x_0, \end{aligned}$$

under the assumption of a tangential cone condition of the form (3.1). The main part of the analysis, which is based on the classical convergence analysis of gradient-based iterative regularization methods (see [46, 72]) is presented in detail in Section 3.1. Thereby, certain abstract conditions on λ_k^δ and α_k^δ are required, which we show to be satisfied for a constant stepsize as well as the steepest descent and the minimal error stepsizes and suitable choices of λ_k^δ in Section 3.2. For multiple numerical examples treating various versions of TPG methods see Part II of this thesis.

3.1 Convergence Analysis I

For the following analysis of TPG methods of the form (2.23), we need a few assumptions which are quite similar to the assumptions needed for the analysis of Landweber iteration or the steepest descent method [72]. Firstly, we need the following version of the tangential cone condition (2.7):

$$\begin{aligned} \|F(x) - F(\tilde{x}) - F'(x)(x - \tilde{x})\| &\leq \eta \|F(x) - F(\tilde{x})\|, \quad \eta < \frac{1}{2}, \\ x, \tilde{x} &\in \mathcal{B}_{4\rho}(x_0) \subset \mathcal{D}(F), \end{aligned} \tag{3.1}$$

where $\mathcal{B}_{4\rho}(x_0)$ denotes the closed ball around x_0 with radius 4ρ . Assuming this condition to hold allows the application of the following:

Lemma 3.1.1. *Let $\rho, \varepsilon > 0$ be such that*

$$\begin{aligned} \|F(x) - F(\tilde{x}) - F'(x)(x - \tilde{x})\| &\leq c(x, \tilde{x}) \|F(x) - F(\tilde{x})\|, \\ x, \tilde{x} &\in \mathcal{B}_\rho(x_0) \subset \mathcal{D}(F), \end{aligned} \quad (3.2)$$

where $c(x, \tilde{x}) \geq 0$ and $c(x, \tilde{x}) < 1$ if $\|x - \tilde{x}\| \leq \varepsilon$. If $F(x) = y$ is solvable in $\mathcal{B}_\rho(x_0)$, then a unique x_0 -minimum-norm solution exists. It is characterized as the solution x^\dagger of $F(x) = y$ in $\mathcal{B}_\rho(x_0)$ satisfying the condition

$$x^\dagger - x_0 \in \mathcal{N}(F'(x^\dagger))^\perp. \quad (3.3)$$

Proof. [46, Proposition 2.1] □

It is necessary to place some restrictions on the stepsizes α_k^δ and the combination parameters λ_k^δ . Minimal requirements on their values are:

$$\lambda_0^\delta = 0, \quad 0 \leq \lambda_k^\delta \leq 1, \quad \forall k \in \mathbb{N}, \quad \alpha_k^\delta \geq 0, \quad \forall k \in \mathbb{N}. \quad (3.4)$$

With this, we can prove the following important:

Proposition 3.1.2. *Assume that (3.1) and (3.4) hold and that equation $F(x) = y$ has a solution x_* in $\mathcal{B}_\rho(x_0) = \mathcal{B}_\rho(x_{-1})$ and let $x_k^\delta, x_{k-1}^\delta \in \mathcal{B}_\rho(x_*)$. Let*

$$\|y^\delta - F(z_k^\delta)\| > \tau\delta, \quad (3.5)$$

with τ satisfying

$$\tau > 2 \frac{1 + \eta}{1 - 2\eta}. \quad (3.6)$$

Setting

$$\Delta_k := \|x_k^\delta - x_*\|^2 - \|x_{k-1}^\delta - x_*\|^2, \quad (3.7)$$

and

$$\Psi := (1 - 2\eta) - 2\tau^{-1}(1 + \eta) > 0, \quad (3.8)$$

there holds

$$\Delta_{k+1} \leq \lambda_k^\delta \Delta_k + \lambda_k^\delta (\lambda_k^\delta + 1) \|x_k^\delta - x_{k-1}^\delta\|^2 - (1 + \Psi) \alpha_k^\delta \|y^\delta - F(z_k^\delta)\|^2 + (\alpha_k^\delta)^2 \|s_k^\delta\|^2. \quad (3.9)$$

Proof. Since $x_k^\delta, x_{k-1}^\delta \in \mathcal{B}_\rho(x_*)$, using the triangle inequality and $x_* \in \mathcal{B}_\rho(x_0)$, we get that $x_k^\delta, x_{k-1}^\delta \in \mathcal{B}_{2\rho}(x_0)$. Together with $\lambda_k^\delta \leq 1$, this implies

$$\begin{aligned} \|z_k^\delta - x_0\| &\leq \|z_k^\delta - x_k^\delta\| + \|x_k^\delta - x_0\| = \lambda_k^\delta \|x_k^\delta - x_{k-1}^\delta\| + \|x_k^\delta - x_0\| \\ &\leq \lambda_k^\delta \|x_k^\delta - x_*\| + \lambda_k^\delta \|x_* - x_{k-1}^\delta\| + \|x_k^\delta - x_0\| \leq 2\lambda_k^\delta \rho + 2\rho \leq 4\rho. \end{aligned} \quad (3.10)$$

which shows that $z_k^\delta \in \mathcal{B}_{4\rho}(x_0)$. Hence, we can apply (3.1), which leads to

$$\begin{aligned}
 \|x_{k+1}^\delta - x_*\|^2 - \|z_k^\delta - x_*\|^2 &= \|x_{k+1}^\delta - z_k^\delta + z_k^\delta - x_*\|^2 - \|z_k^\delta - x_*\|^2 \\
 &= 2 \langle x_{k+1}^\delta - z_k^\delta, z_k^\delta - x_* \rangle + \|x_{k+1}^\delta - z_k^\delta\|^2 \\
 &\stackrel{(2.23)}{=} 2\alpha_k^\delta \langle y^\delta - F(z_k^\delta), F'(z_k^\delta)(z_k^\delta - x_*) \rangle + (\alpha_k^\delta)^2 \|s_k^\delta\|^2 \\
 &= 2\alpha_k^\delta \langle y^\delta - F(z_k^\delta), y^\delta - y \rangle + 2\alpha_k^\delta \langle y^\delta - F(z_k^\delta), F(z_k^\delta) - y^\delta \rangle \\
 &\quad + 2\alpha_k^\delta \langle y^\delta - F(z_k^\delta), y - F(z_k^\delta) + F'(z_k^\delta)(z_k^\delta - x_*) \rangle + (\alpha_k^\delta)^2 \|s_k^\delta\|^2 \\
 &\leq 2\alpha_k^\delta \|y^\delta - F(z_k^\delta)\| \delta - 2\alpha_k^\delta \|y^\delta - F(z_k^\delta)\|^2 + (\alpha_k^\delta)^2 \|s_k^\delta\|^2 \\
 &\quad + 2\alpha_k^\delta \|y^\delta - F(z_k^\delta)\| \|y - F(z_k^\delta) + F'(z_k^\delta)(z_k^\delta - x_*)\| \\
 &\stackrel{(3.1)}{\leq} 2\alpha_k^\delta \|y^\delta - F(z_k^\delta)\| \delta - 2\alpha_k^\delta \|y^\delta - F(z_k^\delta)\|^2 + (\alpha_k^\delta)^2 \|s_k^\delta\|^2 \\
 &\quad + 2\alpha_k^\delta \eta \|y^\delta - F(z_k^\delta)\| \|F(x_*) - F(z_k^\delta)\| \\
 &\leq 2\alpha_k^\delta \|y^\delta - F(z_k^\delta)\| \delta - 2\alpha_k^\delta \|y^\delta - F(z_k^\delta)\|^2 + (\alpha_k^\delta)^2 \|s_k^\delta\|^2 \\
 &\quad + 2\alpha_k^\delta \eta \|y^\delta - F(z_k^\delta)\| (\|F(z_k^\delta) - y^\delta\| + \delta) \\
 &= \alpha_k^\delta \|y^\delta - F(z_k^\delta)\| (2\delta(1 + \eta) - (1 - 2\eta) \|y^\delta - F(z_k^\delta)\|) \\
 &\quad - \alpha_k^\delta (\|F(z_k^\delta) - y^\delta\|^2 - \alpha_k^\delta \|s_k^\delta\|^2) \\
 &\stackrel{(3.5)}{\leq} \alpha_k^\delta \|y^\delta - F(z_k^\delta)\|^2 (2\tau^{-1}(1 + \eta) - (1 - 2\eta)) \\
 &\quad - \alpha_k^\delta (\|F(z_k^\delta) - y^\delta\|^2 - \alpha_k^\delta \|s_k^\delta\|^2)
 \end{aligned} \tag{3.11}$$

Hence, using (3.8), we arrive at the estimate

$$\|x_{k+1}^\delta - x_*\|^2 \leq \|z_k^\delta - x_*\|^2 - (1 + \Psi)\alpha_k^\delta \|F(z_k^\delta) - y^\delta\|^2 + (\alpha_k^\delta)^2 \|s_k^\delta\|^2. \tag{3.12}$$

Now, using the above inequality, we get

$$\begin{aligned}
 \Delta_{k+1} &= \|x_{k+1}^\delta - x_*\|^2 - \|x_k^\delta - x_*\|^2 \\
 &\stackrel{(3.12)}{\leq} \|z_k^\delta - x_*\|^2 - \|x_k^\delta - x_*\|^2 - (1 + \Psi)\alpha_k^\delta \|F(z_k^\delta) - y^\delta\|^2 + (\alpha_k^\delta)^2 \|s_k^\delta\|^2 \\
 &= 2 \langle z_k^\delta - x_k^\delta, x_k^\delta - x_* \rangle + \|z_k^\delta - x_k^\delta\|^2 - (1 + \Psi)\alpha_k^\delta \|F(z_k^\delta) - y^\delta\|^2 + (\alpha_k^\delta)^2 \|s_k^\delta\|^2 \\
 &\stackrel{(2.23)}{=} -2\lambda_k^\delta \langle x_{k-1}^\delta - x_k^\delta, x_k^\delta - x_* \rangle + (\lambda_k^\delta)^2 \|x_k^\delta - x_{k-1}^\delta\|^2 \\
 &\quad - (1 + \Psi)\alpha_k^\delta \|F(z_k^\delta) - y^\delta\|^2 + (\alpha_k^\delta)^2 \|s_k^\delta\|^2 \\
 &= -\lambda_k^\delta \left(\|x_{k-1}^\delta - x_k^\delta + x_k^\delta - x_*\|^2 - \|x_k^\delta - x_*\|^2 - \|x_k^\delta - x_{k-1}^\delta\|^2 \right) \\
 &\quad + (\lambda_k^\delta)^2 \|x_k^\delta - x_{k-1}^\delta\|^2 - (1 + \Psi)\alpha_k^\delta \|F(z_k^\delta) - y^\delta\|^2 + (\alpha_k^\delta)^2 \|s_k^\delta\|^2 \\
 &= -\lambda_k^\delta \left(\|x_{k-1}^\delta - x_*\|^2 - \|x_k^\delta - x_*\|^2 \right) + \lambda_k^\delta (\lambda_k^\delta + 1) \|x_k^\delta - x_{k-1}^\delta\|^2 \\
 &\quad - (1 + \Psi)\alpha_k^\delta \|F(z_k^\delta) - y^\delta\|^2 + (\alpha_k^\delta)^2 \|s_k^\delta\|^2 \\
 &= \lambda_k^\delta \Delta_k + \lambda_k^\delta (\lambda_k^\delta + 1) \|x_k^\delta - x_{k-1}^\delta\|^2 - (1 + \Psi)\alpha_k^\delta \|F(z_k^\delta) - y^\delta\|^2 + (\alpha_k^\delta)^2 \|s_k^\delta\|^2,
 \end{aligned}$$

which yields the assertion. \square

In order to stop the iteration, we use the *discrepancy principle* (see (2.6)), but here with respect to z_k^δ instead of x_k^δ , i.e., we stop the iteration after k_* iterations, where $k_* = k_*(\delta, y^\delta)$ is the smallest integer such that

$$\|y^\delta - F(z_{k_*}^\delta)\| \leq \tau\delta < \|y^\delta - F(z_k^\delta)\|, \quad 0 \leq k < k_*, \quad (3.13)$$

and use $z_{k_*}^\delta$ as approximation of x^\dagger . For the constant τ , as suggested by Proposition 3.1.2, we use the condition (compare with (2.9))

$$\tau > 2 \frac{1 + \eta}{1 - 2\eta}. \quad (3.14)$$

In the convergence analysis of Landweber iteration, one uses the fact that $\Delta_{k+1} \leq 0$ for all $k < k_*$, i.e., that x_{k+1}^δ is a better approximation of x_* than x_k^δ as long as the discrepancy principle (2.6) is not yet satisfied. We would like our TPG methods to share this property. Hence, in view of (3.9), we use the following *coupling condition*:

$$\lambda_k^\delta (\lambda_k^\delta + 1) \|x_k^\delta - x_{k-1}^\delta\|^2 - \left(1 + \frac{\Psi}{\mu}\right) \alpha_k^\delta \|F(z_k^\delta) - y^\delta\|^2 + (\alpha_k^\delta)^2 \|s_k^\delta\|^2 \leq 0. \quad (3.15)$$

which has to hold for all $0 \leq k < k_*$ with k_* determined by (3.13) and where μ is a constant satisfying $\mu > 1$. This implies $\Delta_{k+1} \leq \lambda_k^\delta \Delta_k$ and therefore, in view of $\lambda_0^\delta = 0$ and $\lambda_k^\delta \geq 0$ for all k , we inductively get that $\Delta_{k+1} \leq 0$.

Condition (3.15) essentially yields restrictions on the parameters λ_k^δ and α_k^δ . As a result, one has to ask if there exist choices of λ_k^δ and α_k^δ such that (3.15) is satisfied. For all stepsizes α_k^δ considered below, we are going to see that there holds

$$\alpha_k^\delta \|s_k^\delta\|^2 \leq \|F(z_k^\delta) - y^\delta\|^2, \quad (3.16)$$

and hence, a sufficient condition for (3.15) to hold is given by

$$\lambda_k^\delta (\lambda_k^\delta + 1) \|x_k^\delta - x_{k-1}^\delta\|^2 \leq \frac{\Psi}{\mu} \alpha_k^\delta \|F(z_k^\delta) - y^\delta\|^2. \quad (3.17)$$

Obviously, $\lambda_k^\delta = 0$ satisfies this inequality, which corresponds to classical Landweber type iterations. In finding other admissible choices of λ_k^δ and α_k^δ , one has to be careful, since both α_k^δ and z_k^δ might depend on λ_k^δ . Even for constant stepsizes $\alpha_k^\delta = \omega$ one is left with

$$\lambda_k^\delta (\lambda_k^\delta + 1) \|x_k^\delta - x_{k-1}^\delta\|^2 \leq \frac{\Psi}{\mu} \omega \|F(z_k^\delta) - y^\delta\|^2, \quad (3.18)$$

where it is not immediately clear how to choose λ_k^δ such that this inequality is satisfied. From the discrepancy principle (3.13), one can derive the sufficient condition

$$\lambda_k^\delta (\lambda_k^\delta + 1) \|x_k^\delta - x_{k-1}^\delta\|^2 \leq \frac{\Psi}{\mu} \omega (\tau\delta)^2, \quad (3.19)$$

which leads to the choice

$$\lambda_k^\delta = \min \left\{ -\frac{1}{2} + \sqrt{\frac{1}{4} + \frac{\Psi\omega(\tau\delta)^2}{\mu \|x_k^\delta - x_{k-1}^\delta\|^2}}, 1 \right\}, \quad (3.20)$$

where the minimum with 1 is taken in order to guarantee $0 \leq \lambda_k^\delta \leq 1$. As the numerical examples presented in Part II show, this choice indeed leads to a speedup compared to classical Landweber iteration which, however, decreases as $\delta \rightarrow 0$, which could be expected, since for $\delta = 0$, we get $\lambda_k^\delta = \lambda_k^0 = 0$ and hence, we recover classical Landweber iteration, known to be slow.

One possibility for finding a sequence λ_k^δ , based on a backtracking search procedure, which takes nonzero values also for $\delta = 0$, satisfies condition (3.15) and leads to a considerable acceleration effect is presented in Section 3.2.

We now continue the convergence analysis of the TPG methods (2.23) by deducing the following proposition based on Proposition 3.1.2 and the coupling condition (3.15):

Proposition 3.1.3. *Assume that (3.1) and (3.4) hold and that equation $F(x) = y$ has a solution x_* in $\mathcal{B}_\rho(x_0) = \mathcal{B}_\rho(x_{-1})$. Let $k_* = k(\delta, y^\delta)$ be chosen according to the stopping rule (3.13), (3.14) and assume that (3.15) holds for all $0 \leq k < k_*$. Then x_k^δ as in (2.23) is well-defined and*

$$\|x_{k+1}^\delta - x_*\| \leq \|x_k^\delta - x_*\|, \quad \forall (-1) \leq k < k_*. \quad (3.21)$$

Moreover, $x_k^\delta \in \mathcal{B}_\rho(x_*) \subset \mathcal{B}_{2\rho}(x_0)$ for all $(-1) \leq k \leq k_*$ and

$$\left(\min_{0 \leq k < k_*} \{\alpha_k^\delta\} \right) k_*(\tau\delta)^2 \leq \sum_{k=0}^{k_*-1} \alpha_k^\delta \|y^\delta - F(z_k^\delta)\|^2 \leq (\bar{\mu}\Psi)^{-1} \|x_0^\delta - x_*\|^2, \quad (3.22)$$

where $\bar{\mu} = (\mu - 1)/\mu > 0$.

Proof. From (3.9) it follows for $k = 0$ that

$$\Delta_1 \leq \lambda_0^\delta \Delta_0 + \lambda_0^\delta (\lambda_0^\delta + 1) \|x_0^\delta - x_{-1}^\delta\|^2 - (1 + \Psi)\alpha_0^\delta \|y^\delta - F(z_0^\delta)\|^2 + (\alpha_0^\delta)^2 \|s_0^\delta\|^2.$$

Using (3.15) and $\lambda_0^\delta = 0$, we can deduce that

$$\begin{aligned} \Delta_1 &\leq \lambda_0^\delta (\lambda_0^\delta + 1) \|x_0^\delta - x_{-1}^\delta\|^2 - (1 + \Psi)\alpha_0^\delta \|y^\delta - F(z_0^\delta)\|^2 + (\alpha_0^\delta)^2 \|s_0^\delta\|^2 \\ &\stackrel{(3.15)}{\leq} -\frac{\mu - 1}{\mu} \Psi \alpha_0^\delta \|y^\delta - F(z_0^\delta)\|^2 = -\bar{\mu} \Psi \alpha_0^\delta \|y^\delta - F(z_0^\delta)\|^2 \leq 0, \end{aligned} \quad (3.23)$$

from which we get that $x_1^\delta \in \mathcal{B}_\rho(x_*)$. Now, we proceed inductively to show that

$$\Delta_{k+1} \leq -\bar{\mu} \Psi \alpha_k^\delta \|y^\delta - F(z_k^\delta)\|^2 \leq 0, \quad (3.24)$$

and $x_{k+1}^\delta \in \mathcal{B}_\rho(x_*)$ for all $0 \leq k < k_*$. To do so, we assume that this holds for all $0 \leq m \leq k$. Again using (3.9), we deduce that

$$\Delta_{k+1} \leq \lambda_k^\delta \Delta_k + \lambda_k^\delta (\lambda_k^\delta + 1) \|x_k^\delta - x_{k-1}^\delta\|^2 - (1 + \Psi) \alpha_k^\delta \|F(z_k^\delta) - y^\delta\|^2 + (\alpha_k^\delta)^2 \|s_k^\delta\|^2, \quad (3.25)$$

which, together with (3.15) and the induction hypothesis yields (3.24). From this, we can deduce $x_{k+1}^\delta \in \mathcal{B}_\rho(x_*) \subset \mathcal{B}_{2\rho}(x_0)$, which completes the induction.

Furthermore, from (3.24) we can deduce that

$$\bar{\mu} \Psi \alpha_k^\delta \|y^\delta - F(z_k^\delta)\|^2 \leq \|x_k^\delta - x_*\|^2 - \|x_{k+1}^\delta - x_*\|^2, \quad (3.26)$$

and hence, also

$$\sum_{k=0}^{k_*-1} \bar{\mu} \Psi \alpha_k^\delta \|y^\delta - F(z_k^\delta)\|^2 \leq \|x_0^\delta - x_*\|^2 - \|x_{k_*}^\delta - x_*\|^2 \leq \|x_0^\delta - x_*\|^2. \quad (3.27)$$

From this, we get the estimate

$$\left(\min_{0 \leq k < k_*} \{\alpha_k^\delta\} \right) k_* (\tau \delta)^2 \leq \sum_{k=0}^{k_*-1} \alpha_k^\delta \|y^\delta - F(z_k^\delta)\|^2 \leq (\bar{\mu} \Psi)^{-1} \|x_0^\delta - x_*\|^2, \quad (3.28)$$

which yields the assertion. \square

From the above proposition, we get the following simple:

Corollary 3.1.4. *Under the assumptions of Proposition 3.1.3, we have*

$$k_* \leq \left(\min_{0 \leq k < k_*} \{\alpha_k^\delta\} \right)^{-1} \frac{\|x_0^\delta - x_*\|^2}{\bar{\mu} \Psi (\tau \delta)^2}. \quad (3.29)$$

If we are given exact data $y^\delta = y$, i.e., if $\delta = 0$, then (3.22) implies

$$\sum_{k=0}^{\infty} \alpha_k \|y - F(z_k)\|^2 < \infty, \quad (3.30)$$

as in this case $k_* = \infty$. Note that this only holds if $F(z_k) \neq y$ for all $k \in \mathbb{N}$, since otherwise the sum terminates in a finite number of steps. However, this is not a restriction, since if $F(z_k) = y$ for some k , then a solution is found and the iteration is terminated.

Combining (3.30) together with (3.15), we furthermore get that

$$\sum_{k=0}^{\infty} \lambda_k^0 (\lambda_k^0 + 1) \|x_k - x_{k-1}\|^2 < \infty, \quad (3.31)$$

and

$$\sum_{k=0}^{\infty} (\alpha_k)^2 \|s_k\|^2 < \infty, \quad (3.32)$$

from which there obviously follows

$$\begin{aligned} \lim_{k \rightarrow \infty} \alpha_k \|y - F(z_k)\|^2 &= 0, \\ \lim_{k \rightarrow \infty} \lambda_k^0 (\lambda_k^0 + 1) \|x_k - x_{k-1}\|^2 &= 0, \\ \lim_{k \rightarrow \infty} (\alpha_k)^2 \|s_k\|^2 &= 0. \end{aligned} \quad (3.33)$$

If, additionally, α_k^δ is bounded from below, i.e.,

$$0 < \alpha_{\min}^\delta := \min_{k \in \mathbb{N}} \{\alpha_k^\delta\}, \quad (3.34)$$

then it even follows that

$$\lim_{k \rightarrow \infty} \|y - F(z_k)\| = 0. \quad (3.35)$$

If we can show that z_k converges as well, then we get convergence of the iteration to a solution of $F(x) = y$. In order to do this, we first have to show a couple of intermediate results. We start by showing that under certain assumptions, the sequence $\|z_k - x_*\|$ has a finite limit as $k \rightarrow \infty$.

Proposition 3.1.5. *Let x_* be a solution of $F(x) = y$, and let x_k be the iterates (2.23) with exact data, i.e., $\delta = 0$. Assume that $\|x_k - x_*\| \rightarrow \varepsilon$ as $k \rightarrow \infty$, where $\varepsilon \geq 0$ is a constant. If $\lambda_k^0 \|x_k - x_{k-1}\| \rightarrow 0$ and $\alpha_k \|s_k\| \rightarrow 0$ as $k \rightarrow \infty$, then there holds*

$$\lim_{k \rightarrow \infty} \|z_k - x_*\| = \varepsilon. \quad (3.36)$$

Proof. From the definition of the iterates (2.23), we have the inequality

$$\|z_k - x_*\| = \|x_k - x_* + \lambda_k^0 (x_k - x_{k-1})\| \leq \|x_k - x_*\| + \lambda_k^0 \|x_k - x_{k-1}\| \quad (3.37)$$

and

$$\|x_{k+1} - x_*\| = \|z_k - x_* + \alpha_k s_k\| \leq \|z_k - x_*\| + \alpha_k \|s_k\|, \quad (3.38)$$

from which there follows

$$\|x_{k+1} - x_*\| - \alpha_k \|s_k\| \leq \|z_k - x_*\| \leq \|x_k - x_*\| + \lambda_k^0 \|x_k - x_{k-1}\| \quad (3.39)$$

Taking the limit as $k \rightarrow \infty$ now yields the assertion. \square

The following characterisation of the iterates x_k^δ is useful later on:

Lemma 3.1.6. *For the iterates of the TPG methods (2.23) there holds*

$$x_k^\delta = x_0 + \sum_{i=0}^{k-1} \lambda_i^\delta (x_i^\delta - x_{i-1}^\delta) + \sum_{i=0}^{k-1} \alpha_i^\delta s_i^\delta, \quad (3.40)$$

as well as

$$x_l^\delta - x_j^\delta = \sum_{i=j}^{l-1} \lambda_i^\delta (x_i^\delta - x_{i-1}^\delta) + \sum_{i=j}^{l-1} \alpha_i^\delta s_i^\delta, \quad (3.41)$$

and

$$x_i^\delta - x_{i-1}^\delta = \sum_{m=0}^{i-2} \left(\prod_{n=m+1}^{i-1} \lambda_n^\delta \right) \alpha_m^\delta s_m^\delta + \alpha_{i-1}^\delta s_{i-1}^\delta. \quad (3.42)$$

Proof. The first two of the above statements follow immediately from (2.23). Hence, it remains to prove (3.42), which we do by induction. For $i = 1$ the statement follows immediately from (2.23). Assuming now that (3.42) holds for all $1 \leq l \leq i$, we get

$$\begin{aligned} x_{i+1}^\delta - x_i^\delta &\stackrel{(2.23)}{=} \lambda_i^\delta (x_i^\delta - x_{i-1}^\delta) + \alpha_i^\delta s_i^\delta \\ &= \lambda_i^\delta \left(\sum_{m=0}^{i-2} \left(\prod_{n=m+1}^{i-1} \lambda_n^\delta \right) \alpha_m^\delta s_m^\delta + \alpha_{i-1}^\delta s_{i-1}^\delta \right) + \alpha_i^\delta s_i^\delta \\ &= \sum_{m=0}^{i-1} \left(\prod_{n=m+1}^i \lambda_n^\delta \right) \alpha_m^\delta s_m^\delta + \alpha_i^\delta s_i^\delta, \end{aligned} \quad (3.43)$$

which concludes the induction and hence the lemma is shown. \square

Lemma 3.1.7. *Assume that (3.1) holds, let $x_* \in \mathcal{B}_{4\rho}(x_0)$ be a solution of $F(x) = y$ and let $x_1, x_2 \in \mathcal{B}_{4\rho}(x_0)$. Then there holds*

$$\|F'(x_1)(x_* - x_2)\| \leq 2(1 + \eta) \|F(x_1) - y\| + (1 + \eta) \|F(x_2) - y\|. \quad (3.44)$$

Proof. The proof of this lemma was already done in [72] and is re-stated here for the sake of completeness. Using (3.1), it follows that

$$\begin{aligned} \|F'(x_1)(x_* - x_2)\| &= \|F'(x_1)(x_* - x_1 + x_1 - x_2)\| \\ &\leq \|-F(x_*) + F(x_1) + F'(x_1)(x_* - x_1) - F(x_1) + F(x_*)\| \\ &\quad + \|F(x_2) - F(x_1) + F'(x_1)(x_1 - x_2) - F(x_2) + F(x_1)\| \\ &\leq (1 + \eta) \|F(x_1) - y\| + (1 + \eta) \|F(x_1) - F(x_2)\| \\ &\leq 2(1 + \eta) \|F(x_1) - y\| + (1 + \eta) \|F(x_2) - y\|, \end{aligned} \quad (3.45)$$

which yields the assertion. \square

In order to prove convergence in the case of exact data in Theorem 3.1.8 below, we need the following additional assumption on the combination parameters λ_k^0 :

$$\sum_{k=0}^{\infty} \lambda_k^0 \|x_k - x_{k-1}\| < \infty. \quad (3.46)$$

Since under the previous assumptions $\|x_k - x_{k-1}\|$ can be bounded (by 2ρ), it follows that a sufficient condition for (3.46) to hold is given by

$$\sum_{k=0}^{\infty} \lambda_k^0 < \infty. \quad (3.47)$$

For λ_k^δ defined by (3.20), condition (3.47) is obviously satisfied. However, it is quite a restrictive condition, since it implies $\lambda_k^0 \rightarrow 0$ as $k \rightarrow \infty$. Comparing this with the classical Nesterov combination parameters $\lambda_k^\delta = (k-1)/(k+\alpha-1)$, which tend to 1 as $k \rightarrow \infty$ even for $\delta = 0$, we see that in order to achieve a non-negligible acceleration effect also for $\delta = 0$, one has to work with condition (3.46) instead of only the sufficient condition (3.47). In Section 3.2, we present an algorithm for choosing λ_k^δ such that (3.46) is satisfied and the numerical examples presented in Part II show that for this sequence, under a suitable choice of parameters, there holds $\lambda_k^\delta \rightarrow 1$ as $k \rightarrow \infty$, leading to the desired acceleration effect. Using (3.46), we can now prove the following:

Theorem 3.1.8. *Assume that (3.1) holds and that equation $F(x) = y$ has a solution x_* in $\mathcal{B}_\rho(x_0) = \mathcal{B}_\rho(x_{-1})$. Let $k_* = k_*(0, y) = \infty$, λ_k^δ and α_k^δ satisfy (3.4), (3.34) and (3.46) and assume that (3.15) holds for all $k \in \mathbb{N}$. Then the iterates z_k defined as in (2.23) with exact data $y^\delta = y$ converge to a solution of $F(x) = y$. If $\mathcal{N}(F'(x^\dagger)) \subset \mathcal{N}(F'(x))$ for all $x \in \mathcal{B}_{4\rho}(x^\dagger)$, then z_k converges to x^\dagger as $k \rightarrow \infty$.*

Proof. This proof closely follows the corresponding proof for Landweber iteration given in [21]. Let x_* be a solution of $F(x) = y$ in $\mathcal{B}_\rho(x_0)$ and define

$$e_k := z_k - x_*. \quad (3.48)$$

From Proposition 3.1.3 it follows that $\|x_k - x_*\|$ converges to some $\varepsilon \geq 0$ and hence, using (3.33) and Proposition 3.1.5, we can deduce that $\|e_k\|$ converges to this same ε as well. We are now going to show that e_k is a Cauchy sequence. Given $j \geq k$, we choose some integer l between k and j with

$$\|y - F(z_l)\| \leq \|y - F(z_i)\|, \quad \forall k \leq i \leq j. \quad (3.49)$$

We have

$$\|e_j - e_k\| \leq \|e_j - e_l\| + \|e_l - e_k\|, \quad (3.50)$$

and

$$\begin{aligned} \|e_j - e_l\|^2 &= 2 \langle e_l - e_j, e_l \rangle + \|e_j\|^2 - \|e_l\|^2, \\ \|e_l - e_k\|^2 &= 2 \langle e_l - e_k, e_l \rangle + \|e_k\|^2 - \|e_l\|^2, \end{aligned} \quad (3.51)$$

For $k \rightarrow \infty$, the last two terms on each of the right hand sides of the above equations converge to $\varepsilon^2 - \varepsilon^2 = 0$. We now show that $\langle e_l - e_k, e_l \rangle$ and $\langle e_l - e_j, e_l \rangle$ also tend to 0 as $k \rightarrow \infty$. For this we first consider:

$$\begin{aligned} |\langle e_l - e_k, e_l \rangle| &= |\langle z_l - z_k, e_l \rangle| = \left| \langle x_l - x_k + \lambda_l^0(x_l - x_{l-1}) - \lambda_k^0(x_k - x_{k-1}), e_l \rangle \right| \\ &\leq |\langle x_l - x_k, e_l \rangle| + \lambda_l^0 |\langle x_l - x_{l-1}, e_l \rangle| + \lambda_k^0 |\langle x_k - x_{k-1}, e_l \rangle| \\ &\leq |\langle x_l - x_k, e_l \rangle| + \lambda_l^0 \|x_l - x_{l-1}\| \|e_l\| + \lambda_k^0 \|x_k - x_{k-1}\| \|e_l\|. \end{aligned} \quad (3.52)$$

Now, using (3.33) and the fact that $\|e_k\|$ converges to ε , we get that

$$\lim_{k \rightarrow \infty} (\lambda_l^0 \|x_l - x_{l-1}\| \|e_l\| + \lambda_k^0 \|x_k - x_{k-1}\| \|e_l\|) = 0. \quad (3.53)$$

Hence, it remains to consider

$$\begin{aligned} |\langle x_l - x_k, e_l \rangle| &\stackrel{(3.41)}{=} \left| \left\langle \sum_{i=k}^{l-1} \lambda_i^0(x_i - x_{i-1}) + \sum_{i=k}^{l-1} \alpha_i s_i, e_l \right\rangle \right| \\ &\leq \sum_{i=k}^{l-1} \lambda_i^0 |\langle x_i - x_{i-1}, e_l \rangle| + \sum_{i=k}^{l-1} \alpha_i |\langle s_i, e_l \rangle|. \end{aligned} \quad (3.54)$$

We now consider the above two sums separately, starting with the second one. By Lemma 3.1.7, we have

$$\begin{aligned} \sum_{i=k}^{l-1} \alpha_i |\langle s_i, e_l \rangle| &= \sum_{i=k}^{l-1} \alpha_i |\langle y - F(z_i), F'(z_i)(z_l - x_*) \rangle| \\ &\leq \sum_{i=k}^{l-1} \alpha_i \|y - F(z_i)\| \|F'(z_i)(z_l - x_*)\| \\ &\stackrel{(3.44)}{\leq} 2(1 + \eta) \sum_{i=k}^{l-1} \alpha_i \|y - F(z_i)\|^2 + (1 + \eta) \sum_{i=k}^{l-1} \alpha_i \|y - F(z_i)\| \|y - F(z_l)\| \\ &\leq 3(1 + \eta) \sum_{i=k}^{l-1} \alpha_i \|y - F(z_i)\|^2 \leq 3(1 + \eta) \sum_{i=k}^{\infty} \alpha_i \|y - F(z_i)\|^2, \end{aligned} \quad (3.55)$$

where we have used (3.49). From this, it follows by using (3.30) that

$$\lim_{k \rightarrow \infty} \left(\sum_{i=k}^{l-1} \alpha_i |\langle s_i, e_l \rangle| \right) = 0. \quad (3.56)$$

Next we consider

$$\sum_{i=k}^{l-1} \lambda_i^0 |\langle x_i - x_{i-1}, e_l \rangle| \leq \sum_{i=k}^{l-1} \lambda_i^0 \|x_i - x_{i-1}\| \|e_l\| \leq \sum_{i=k}^{\infty} \lambda_i^0 \|x_i - x_{i-1}\| \|e_l\|. \quad (3.57)$$

Since $\|e_l\|$ is bounded, it immediately follows from (3.46) that

$$\lim_{k \rightarrow \infty} \left(\sum_{i=k}^{l-1} \lambda_i^0 |\langle x_i - x_{i-1}, e_l \rangle| \right) = 0. \quad (3.58)$$

Combining the above estimates, we arrive at $|\langle x_l - x_k, e_l \rangle| \rightarrow 0$, from which there follows that $|\langle e_l - e_k, e_l \rangle| \rightarrow 0$ as $k \rightarrow \infty$. Since it can similarly be shown that $|\langle e_l - e_j, e_l \rangle| \rightarrow 0$ as $k \rightarrow \infty$, it follows that

$$\lim_{k \rightarrow \infty} \|e_j - e_k\| = 0, \quad (3.59)$$

from which we deduce that e_k and hence, also z_k is a Cauchy sequence and therefore convergent in the Hilbert space \mathcal{X} . Since $\|F(z_k) - y\|$ converges to 0, the limit of z_k is a solution of $F(x) = y$.

Now we turn to the second part of the proof. If $\mathcal{N}(F'(x^\dagger)) \subset \mathcal{N}(F'(x))$ for all $x \in \mathcal{B}_{4\rho}(x^\dagger)$, then by the definition of the iterates (2.23) we have

$$\begin{aligned} z_{k+1} - z_k &= x_{k+1} + \lambda_{k+1}^0(x_{k+1} - x_k) - z_k = \alpha_k s_k + \lambda_{k+1}^0(x_{k+1} - x_k) \\ &= (1 + \lambda_{k+1}^0)\alpha_k s_k + \lambda_{k+1}^0(z_k - x_k) = (1 + \lambda_{k+1}^0)\alpha_k s_k + \lambda_{k+1}^0 \lambda_k^0(x_k - x_{k-1}) \end{aligned}$$

and therefore

$$z_k - z_0 = \sum_{i=0}^{k-1} (z_{i+1} - z_i) = \sum_{i=0}^{k-1} ((1 + \lambda_{i+1}^0)\alpha_i s_i + \lambda_{i+1}^0 \lambda_i^0(x_i - x_{i-1})). \quad (3.60)$$

Since obviously $(1 + \lambda_{i+1}^0)\alpha_i s_i \in \mathcal{R}(F'(z_i)^*)$ and since

$$\mathcal{R}(F'(z_i)^*) \subset \mathcal{N}(F'(z_i))^\perp \subset \mathcal{N}(F'(x^\dagger))^\perp \quad \text{for all } i \in \mathbb{N}, \quad (3.61)$$

it follows that

$$\sum_{i=0}^{k-1} (1 + \lambda_{i+1}^0)\alpha_i s_i \in \mathcal{N}(F'(x^\dagger))^\perp. \quad (3.62)$$

Similarly as above, it can be seen by using Lemma 3.1.6 that also

$$\sum_{i=0}^{k-1} \lambda_{i+1}^0 \lambda_i^0(x_i - x_{i-1}) \in \mathcal{N}(F'(x^\dagger))^\perp, \quad (3.63)$$

and we therefore conclude that

$$z_k - z_0 \in \mathcal{N}(F'(x^\dagger))^\perp \quad \text{for all } k \in \mathbb{N}. \quad (3.64)$$

Since this also holds for the limit of z_k and since x^\dagger is the unique solution for which this condition holds (cf. Lemma 3.1.1), this proves that $z_k \rightarrow x^\dagger$ as $k \rightarrow \infty$. \square

In the next corollary, we deduce the convergence of x_k given the convergence of z_k .

Corollary 3.1.9. *Under the assumptions of Theorem 3.1.8, we get that x_k converges to x_* , where x_* is the limit of z_k as $k \rightarrow \infty$.*

Proof. The statement follows immediately from

$$\|x_{k+1} - x_*\| \leq \|z_k - x_*\| + \alpha_k \|s_k\|, \quad (3.65)$$

together with (3.33). \square

Next, we show that using the discrepancy principle (3.13) as a stopping rule, our TPG method (2.23) becomes a convergent regularization method, if we additionally assume that λ_k^δ depends continuously on δ for $\delta \rightarrow 0$.

Theorem 3.1.10. *Assume that (3.1) holds and that equation $F(x) = y$ has a solution x_* in $\mathcal{B}_\rho(x_0) = \mathcal{B}_\rho(x_{-1})$. Let $k_* = k_*(\delta, y^\delta)$ be chosen according to the discrepancy principle (3.13), (3.14) and assume that (3.15) holds for all $0 \leq k < k_*$. Assume that λ_k^δ and α_k^δ satisfy (3.4), (3.34) and (3.46) and that $\lambda_k^\delta \rightarrow \lambda_k^0$ as $\delta \rightarrow 0$. Then the iterates $z_{k_*}^\delta$ defined by (2.23) converge to a solution of $F(x) = y$, as $\delta \rightarrow 0$. If $\mathcal{N}(F'(x^\dagger)) \subset \mathcal{N}(F'(x))$ for all $x \in \mathcal{B}_{4\rho}(x^\dagger)$, then $z_{k_*}^\delta$ converges to x^\dagger as $\delta \rightarrow 0$.*

Proof. Again this proof closely follows the corresponding proof for Landweber iteration given in [21]. Let x_* be the limit point of z_k (and hence, by Corollary 3.1.9, also of x_k) given exact data y and let δ_n be a sequence converging to 0 as $n \rightarrow \infty$. Let furthermore $y_n := y^{\delta_n}$ be a sequence of noisy data with $\|y - y_n\| \leq \delta_n$ and let $k_n := k_*(\delta_n, y_n)$ be the stopping index determined by the discrepancy principle applied to the pair (δ_n, y_n) . There are two cases. First, assume that k is a finite accumulation point of k_n . Without loss of generality, we can assume that $k_n = k$ for all $n \in \mathbb{N}$. Thus, from the definition of the discrepancy principle, it follows that

$$\|y_n - F(z_k^{\delta_n})\| \leq \tau \delta_n. \quad (3.66)$$

As k is fixed, z_k^δ depends continuously on the data y^δ and we can take the limit $n \rightarrow \infty$ in the above inequality, which yields

$$z_k^{\delta_n} \rightarrow z_k, \quad F(z_k^{\delta_n}) \rightarrow F(z_k) = y, \quad \text{as } n \rightarrow \infty. \quad (3.67)$$

In other words, the k th iterate of Landweber iteration with exact data is a solution of $F(x) = y$ and hence, the iteration terminates with $z_k = x_*$, and $z_{k_n}^{\delta_n} \rightarrow x_*$ for this subsequence as $\delta_n \rightarrow 0$.

For the second case, assume that $k_n \rightarrow \infty$ as $n \rightarrow \infty$. For some k and $k_n > k + 1$, Proposition 3.1.3 and $0 \leq \lambda_k^\delta \leq 1$ yield

$$\begin{aligned} \|z_{k_n}^{\delta_n} - x_*\| &\leq \|x_{k_n}^{\delta_n} - x_*\| + \lambda_k^\delta \|x_{k_n}^{\delta_n} - x_*\| + \lambda_k^\delta \|x_{k_n-1}^{\delta_n} - x_*\| \\ &\leq \|x_k^{\delta_n} - x_*\| + \lambda_k^\delta \|x_k^{\delta_n} - x_*\| + \lambda_k^\delta \|x_k^{\delta_n} - x_*\| \\ &\leq 3 \|x_k^{\delta_n} - x_*\| \leq 3 \|x_k^{\delta_n} - x_k\| + 3 \|x_k - x_*\|. \end{aligned} \quad (3.68)$$

If we fix some $\varepsilon > 0$, it follows from Proposition 3.1.2 and from Corollary 3.1.9 that we can fix some $k = k(\varepsilon)$ such that $\|x_k - x_*\| \leq \varepsilon/6$. Since, for fixed k , the iterates depend continuously on the data, there is an $n = n(\varepsilon, k)$ such that $\|x_k^{\delta_n} - x_k\| \leq \varepsilon/6$ for all $n > n(\varepsilon, k)$. Thus if we choose n sufficiently large, such that also $k_n > k + 1$, we get that

$$\|z_{k_n}^{\delta_n} - x_*\| \leq 3 \|x_k^{\delta_n} - x_*\| \leq 3 \|x_k^{\delta_n} - x_k\| + 3 \|x_k - x_*\| \leq 3 \frac{\varepsilon}{6} + 3 \frac{\varepsilon}{6} = \varepsilon, \quad (3.69)$$

and therefore $z_{k_n}^{\delta_n} \rightarrow x_*$ as $n \rightarrow \infty$, which shows the first part of the assertion. If $\mathcal{N}(F'(x^\dagger)) \subset \mathcal{N}(F'(x))$ for all $x \in \mathcal{B}_{4\rho}(x^\dagger)$, then x_* can be chosen as $x_* = x^\dagger$, in which case Theorem 3.1.8 guarantees convergence of $z_k \rightarrow x^\dagger$ (and then also $x_k \rightarrow x^\dagger$). Thus the above arguments apply to that case as well, which yields the assertion. \square

We can now apply the above result to the TPG method (2.23) with constant stepsize $\alpha_k^\delta = \omega$ and λ_k^δ defined by (3.20). For this, we need the additional assumption

$$\sup_{x \in \mathcal{B}_{4\rho}(x_0)} \|F'(x)\| \leq \bar{\omega} < \infty. \quad (3.70)$$

Theorem 3.1.11. *Assume that (3.1) and (3.70) hold and that equation $F(x) = y$ has a solution x_* in $\mathcal{B}_\rho(x_0) = \mathcal{B}_\rho(x_{-1})$. Let $k_* = k_*(\delta, y^\delta)$ be chosen according to the discrepancy principle (3.13), (3.14). Assume that $\alpha_k^\delta = \omega \leq 1/\bar{\omega}^2$, where $\bar{\omega}$ satisfies (3.70) and that λ_k^δ is defined by (3.20), for some $\mu > 1$ and Ψ defined by (3.8). Then the iterates $z_{k_*}^\delta$ defined by (2.23) converge to a solution of $F(x) = y$, as $\delta \rightarrow 0$. If $\mathcal{N}(F'(x^\dagger)) \subset \mathcal{N}(F'(x))$ for all $x \in \mathcal{B}_{4\rho}(x^\dagger)$, then $z_{k_*}^\delta$ converges to x^\dagger as $\delta \rightarrow 0$.*

Proof. Due to $\alpha_k^\delta = \omega \leq 1/\bar{\omega}^2$ and (3.70), there holds

$$\alpha_k^\delta \|s_k^\delta\|^2 \leq \|F(z_k^\delta) - y^\delta\|^2, \quad (3.71)$$

and hence, due to the discrepancy principle (3.13) and the definition of λ_k^δ by (3.20), we get that (3.15) is satisfied for all $0 \leq k < k_*$. Obviously, (3.4) and (3.34) hold, λ_k^δ depends continuously on δ for fixed k and, since $\lambda_k^0 = 0$, also (3.46) is trivially satisfied. Hence, Theorem 3.1.10 is applicable, which immediately yields the desired results. \square

3.2 Examples of TPG methods based on the Steepest Descent and the Minimal Error stepsize

In this section, we introduce two TPG methods (2.23) based on the steepest descent and on the minimal error stepsize and show that, under some assumptions, they lead to convergent regularization methods. If we again denote

$$s_k^\delta := F'(z_k^\delta)^*(y^\delta - F(z_k^\delta)), \quad (3.72)$$

then the *steepest descent* stepsize α_k^{SD} is defined by

$$\alpha_k^{\text{SD}} := \alpha_k^{\text{SD}}(z_k^\delta) := \frac{\|s_k^\delta\|^2}{\|F'(z_k^\delta)s_k^\delta\|^2}, \quad (3.73)$$

and the *minimal error* stepsize α_k^{ME} is defined by

$$\alpha_k^{\text{ME}} := \alpha_k^{\text{ME}}(z_k^\delta) := \frac{\|y^\delta - F(z_k^\delta)\|^2}{\|s_k^\delta\|^2}. \quad (3.74)$$

The choice of the steepest descent stepsize α_k^{SD} is motivated by line-search procedures for optimization methods, where one tries to find an α_k^δ such that the functional

$$\frac{1}{2} \|F(z_k^\delta + \alpha_k^\delta s_k^\delta) - y^\delta\|^2 \quad (3.75)$$

is minimized. The stepsize α_k^{SD} minimizes the linearisation of this functional, i.e.,

$$\alpha_k^{\text{SD}} = \arg \min_{\alpha_k^\delta} \frac{1}{2} \|F(z_k^\delta) + \alpha_k^\delta F'(z_k^\delta)s_k^\delta - y^\delta\|^2. \quad (3.76)$$

As for the minimal error stepsize α_k^{ME} , note that in the proof of Proposition 3.1.2 we showed the following inequality:

$$\|x_{k+1}^\delta - x_*\|^2 \leq \|z_k^\delta - x_*\|^2 - \alpha_k^\delta \left(\|F(z_k^\delta) - y^\delta\|^2 - \alpha_k^\delta \|s_k^\delta\|^2 \right). \quad (3.77)$$

Now, in order to ensure that $\|x_{k+1}^\delta - x_*\| \leq \|z_k^\delta - x_*\|$, the stepsize α_k^δ has to satisfy

$$\alpha_k^\delta \|s_k^\delta\|^2 \leq \|F(z_k^\delta) - y^\delta\|^2, \quad (3.78)$$

and the choice of $\alpha_k^\delta = \alpha_k^{\text{ME}}$ is the largest stepsize fulfilling that requirement.

In the following proposition we show that α_k^{SD} and α_k^{ME} are well defined. The proof is almost completely similar to the one of [46, Proposition 3.20].

Proposition 3.2.1. *Assume that (3.1) holds and that equation $F(x) = y$ has a solution x_* in $\mathcal{B}_\rho(x_0)$. Assume that $x_k^\delta, x_{k-1}^\delta \in \mathcal{B}_\rho(x_*)$ for an arbitrary $k \in \mathbb{N} \cup \{0\}$ and*

$$\|y^\delta - F(z_k^\delta)\| > 2 \frac{1 + \eta}{1 - 2\eta} \delta \quad (3.79)$$

holds. Then $s_k^\delta \neq 0$ and $F'(z_k^\delta)s_k^\delta \neq 0$ and consequently, α_k^{SD} and α_k^{ME} defined by (3.73) and (3.74) are well-defined.

Proof. Since $x_k^\delta, x_{k-1}^\delta \in \mathcal{B}_\rho(x_*)$ it follows as in Proposition 3.1.2 that $z_k \in \mathcal{B}_{4\rho}(x_0)$ and hence (3.1) is applicable. Assume now that $s_k^\delta = 0$. Then we have

$$\begin{aligned}
 0 &= \langle s_k^\delta, z_k^\delta - x_* \rangle = \langle F'(z_k^\delta)^*(y^\delta - F(z_k^\delta)), z_k^\delta - x_* \rangle \\
 &= \langle y^\delta - F(z_k^\delta), F'(z_k^\delta)(z_k^\delta - x_*) \rangle \\
 &= \langle y^\delta - F(z_k^\delta), y^\delta - y + y - y^\delta + F(z_k^\delta) - F(z_k^\delta) + F'(z_k^\delta)(z_k^\delta - x_*) \rangle \quad (3.80) \\
 &= \langle y^\delta - F(z_k^\delta), y^\delta - y \rangle - \|y^\delta - F(z_k^\delta)\|^2 \\
 &\quad - \langle y^\delta - F(z_k^\delta), F(z_k^\delta) - F(x_*) - F'(z_k^\delta)(z_k^\delta - x_*) \rangle .
 \end{aligned}$$

Using (2.2) and (3.1), we get

$$\begin{aligned}
 \|y^\delta - F(z_k^\delta)\|^2 &\leq \|y^\delta - F(z_k^\delta)\| \delta + \eta \|y^\delta - F(z_k^\delta)\| \|F(z_k^\delta) - F(x_*)\| \\
 &\leq \|y^\delta - F(z_k^\delta)\| \delta + \eta \|y^\delta - F(z_k^\delta)\| (\|y^\delta - F(z_k^\delta)\| + \delta) \quad (3.81) \\
 &= \|y^\delta - F(z_k^\delta)\| (\delta + \eta(\delta + \|y^\delta - F(z_k^\delta)\|)) ,
 \end{aligned}$$

and therefore

$$\|y^\delta - F(z_k^\delta)\| \leq \frac{1 + \eta}{1 - \eta} \delta, \quad (3.82)$$

which is a contradiction to (3.79). Hence, $s_k^\delta \neq 0$.

Now assume that $F'(z_k^\delta)s_k^\delta = 0$. Then obviously $s_k^\delta \in \mathcal{N}(F'(z_k^\delta))$. By the definition of s_k^δ , we also have that $s_k^\delta \in \mathcal{R}(F'(z_k^\delta)^*) \subset \mathcal{N}(F'(z_k^\delta))^\perp$. Hence, we have $s_k^\delta = 0$, which is a contradiction to what we have shown above. Hence, $F'(z_k^\delta)s_k^\delta \neq 0$ and therefore α_k^{SD} and α_k^{ME} are well-defined. \square

We now want to prove that all conditions on the stepsize α_k^δ used in the previous section also hold for α_k^{SD} and α_k^{ME} . We start by considering condition (3.34). Assuming (3.70) to hold, it then obviously follows that $\alpha_k^{\text{SD}} \geq 1/\bar{\omega}^2$ and $\alpha_k^{\text{ME}} \geq 1/\bar{\omega}^2$ and hence, condition (3.34) is satisfied. Now we state another helpful result due to [72]:

Lemma 3.2.2. *For the stepsizes $\alpha_k^\delta = \alpha_k^{\text{SD}}, \alpha_k^{\text{ME}}$ defined by (3.73) and (3.74), respectively, there holds*

$$\alpha_k^\delta \|s_k^\delta\|^2 \leq \|y^\delta - F(z_k^\delta)\|^2, \quad (3.83)$$

where equality holds for $\alpha_k^\delta = \alpha_k^{\text{ME}}$ in the above inequality.

Proof. According to its definition, the statement is trivial for α_k^{ME} . For α_k^{SD} , it follows immediately from

$$\alpha_k^{\text{SD}} \|s_k^\delta\|^2 = \frac{\langle F'(z_k^\delta)s_k^\delta, y^\delta - F(z_k^\delta) \rangle^2}{\|F'(z_k^\delta)s_k^\delta\|^2} \leq \|y^\delta - F(z_k^\delta)\|^2. \quad (3.84)$$

\square

We now turn back to the very important condition (3.15). Due to Lemma 3.2.2, if we use $\alpha_k^\delta = \alpha_k^{\text{SD}}$ or $\alpha_k^\delta = \alpha_k^{\text{ME}}$, then a sufficient condition for (3.15) to hold is given by

$$\lambda_k^\delta (\lambda_k^\delta + 1) \|x_k^\delta - x_{k-1}^\delta\|^2 \leq \frac{\Psi}{\mu} \alpha_k^\delta \|F(z_k^\delta) - y^\delta\|^2. \quad (3.85)$$

As we previously noted in Section 3.1, the choice $\lambda_k^\delta = 0$ satisfies this inequality, which, however, corresponds to the classical steepest descent or minimal error method, respectively. Another possibility which, using (3.70), can be derived analogously to (3.20), is given by

$$\lambda_k^\delta = \min \left\{ -\frac{1}{2} + \sqrt{\frac{1}{4} + \frac{\Psi(\tau\delta)^2}{\mu \bar{\omega}^2 \|x_k^\delta - x_{k-1}^\delta\|^2}}, 1 \right\}. \quad (3.86)$$

Note that this is the same as (3.20), given that the optimal stepsize $\omega = 1/\bar{\omega}^2$ is being used. For λ_k^δ as in (3.86), we can deduce the following:

Theorem 3.2.3. *Assume that (3.1) and (3.70) hold and that equation $F(x) = y$ has a solution x_* in $\mathcal{B}_\rho(x_0) = \mathcal{B}_\rho(x_{-1})$. Let $k_* = k_*(\delta, y^\delta)$ be chosen according to the discrepancy principle (3.13), (3.14). Assume that either $\alpha_k^\delta = \alpha_k^{\text{SD}}$ or $\alpha_k^\delta = \alpha_k^{\text{ME}}$, defined by (3.73) or (3.74), respectively. Furthermore, let λ_k^δ be defined by (3.86), for some $\mu > 1$, Ψ defined by (3.8) and $\bar{\omega}$ satisfying (3.70). Then the iterates $z_{k_*}^\delta$ defined by (2.23) converge to a solution of $F(x) = y$, as $\delta \rightarrow 0$. If $\mathcal{N}(F'(x^\dagger)) \subset \mathcal{N}(F'(x))$ for all $x \in \mathcal{B}_{4\rho}(x^\dagger)$, then $z_{k_*}^\delta$ converges to x^\dagger as $\delta \rightarrow 0$.*

Proof. From Lemma 3.2.2, we get that

$$\alpha_k^\delta \|s_k^\delta\|^2 \leq \|F(z_k^\delta) - y^\delta\|^2. \quad (3.87)$$

Together with $\alpha_k^{\text{SD}}, \alpha_k^{\text{ME}} \geq 1/\bar{\omega}^2$, the statements of the theorem now follow from Theorem 3.1.10, analogously as in the proof of Theorem 3.1.11. \square

As for λ_k^δ defined by (3.20), for λ_k^δ defined by (3.86) there also holds $\lambda_k^\delta = 0$ for $\delta = 0$. Since this corresponds to classical Landweber iteration, the steepest descent or minimal error method, the acceleration effect due to those choices of λ_k^δ decrease for $\delta \rightarrow 0$. Since for small values of δ acceleration is needed most, other choices of λ_k^δ also have to be considered.

The crucial conditions which a pair $(\lambda_k^\delta, \alpha_k^\delta)$ has to satisfy in order for Theorem 3.1.10 to be applicable are the conditions (3.15) and (3.46). We have already seen that $\lambda_k^\delta = 0$ and λ_k^δ defined by either (3.20) or (3.86), and hence, all sequences in between those two, satisfy the coupling condition (3.15). Given a stepsize α_k^δ , one could think of choosing $\lambda_k^\delta \leq 1$ as large as possible such that the coupling condition (3.15) is satisfied. However, one also has to guarantee that condition (3.46) is satisfied as well.

One possibility is to choose λ_k^δ as a subsequence of a summable sequence like $(cq^k)_{k \in \mathbb{N}}$, $0 \leq q < 1$, in such a way that (3.15) is satisfied, which, together with the boundedness

of $\|x_k^\delta - x_{k-1}^\delta\|$, guarantees (3.46). Unfortunately, the resulting sequence λ_k^δ tends to 0 as $k \rightarrow \infty$, which in turn only leads to a negligible acceleration effect. However, note that for condition (3.46) to be satisfied, it suffices that the sequence $\lambda_k^0 \|x_k - x_{k-1}\|$ is summable. Hence, we propose the following strategy:

Given a stepsize α_k^δ , define the combination parameters λ_k^δ by

$$\lambda_k^\delta = \begin{cases} 0, & k = 0, \\ \min \left\{ \frac{q_k^\delta}{\|x_k^\delta - x_{k-1}^\delta\|}, 1 \right\}, & k \geq 1, \end{cases}, \quad (3.88)$$

where $(q_k^\delta)_{k \in \mathbb{N}}$ is a decreasing sequence depending continuously on δ for fixed k , satisfying

$$\sum_{k=0}^{\infty} q_k^\delta < \infty, \quad (3.89)$$

and chosen such that condition (3.15) holds. If the sequence $(q_k^\delta)_{k \in \mathbb{N}}$ can be chosen in such a way that it converges to 0 fast enough to satisfy (3.89) but slower than $\|x_k^\delta - x_{k-1}^\delta\|$, the resulting sequence λ_k^δ stays away from 0 and possibly even tend towards 1 as $k \rightarrow \infty$.

Finding a sequence $(q_k^\delta)_{k \in \mathbb{N}}$ satisfying all the required properties such that the resulting TPG method indeed gives rise to a convergent regularization method and how to compute a viable sequence λ_k^δ in practise is the topics of the remainder of this section. First, we consider the problem of finding a suitable sequence $(q_k^\delta)_{k \in \mathbb{N}}$, or alternatively, λ_k^δ , by what in the following we call the *backtracking search (BTS) algorithm*:

Algorithm 3.2.1. [Backtracking search (BTS) algorithm for λ_k^δ , $k > 1$]

- **Given:** $x_k^\delta, x_{k-1}^\delta, \Psi, \mu, y^\delta, F, q : \mathbb{R}_0^+ \rightarrow \mathbb{R}_0^+, m_{k-1}^\delta \in \mathbb{R}$.
- Calculate $\|x_k^\delta - x_{k-1}^\delta\|$ and define

$$\beta_k^\delta(m) := \min \left\{ \frac{q(m)}{\|x_k^\delta - x_{k-1}^\delta\|}, 1 \right\}. \quad (3.90)$$

- Define the functions

$$\begin{aligned} \tilde{\lambda}_k^\delta(m) &:= \beta_k^\delta(m_{k-1}^\delta + 1 + m), \\ \tilde{z}_k^\delta(m) &:= x_k^\delta + \tilde{\lambda}_k^\delta(m)(x_k^\delta - x_{k-1}^\delta), \\ \tilde{\alpha}_k^\delta(m) &:= \alpha_k^\delta(\tilde{z}_k^\delta(m)). \end{aligned} \quad (3.91)$$

- Calculate

$$\begin{aligned} \tilde{m}_k^\delta = \inf \left\{ m \geq 0 \mid \tilde{\lambda}_k^\delta(m)(\tilde{\lambda}_k^\delta(m) + 1) \|x_k^\delta - x_{k-1}^\delta\|^2 \right. \\ \left. \leq \frac{\Psi}{\mu} \tilde{\alpha}_k^\delta(m) \|y^\delta - F(\tilde{z}_k^\delta(m))\|^2 \right\}. \end{aligned} \quad (3.92)$$

- Define $\lambda_k^\delta := \tilde{\lambda}_k^\delta(\tilde{m}_k^\delta)$, $z_k^\delta := \tilde{z}_k^\delta(\tilde{m}_k^\delta)$ and $m_k^\delta := m_{k-1}^\delta + 1 + \tilde{m}_k^\delta$.
- **Output:** $\lambda_k^\delta, z_k^\delta, m_k^\delta$.

In order to carry out the above algorithm, a function $q : \mathbb{R}_0^+ \rightarrow \mathbb{R}_0^+$ needs to be specified. In order to prove convergence of our iteration method with λ_k^δ chosen by Algorithm 3.2.1, we have to make the following assumptions on this function:

$$q(m_1) \leq q(m_2) \quad \forall m_1 > m_2, \quad \sum_{k=0}^{\infty} q(k) < \infty. \quad (3.93)$$

Concerning the calculation of \tilde{m}_k^δ , note first that it is possible that $\tilde{\alpha}_k^\delta(m)$ is not well-defined for certain values of m . However, by Proposition 3.2.1 this can only happen if $\tilde{z}_k^\delta(m)$ is such that (3.79) holds, i.e., that the stopping criterion (3.13) is satisfied, and we therefore consider the inequality in (3.92) to be satisfied for those m . Furthermore, if there is no $m \geq 0$ such that the inequality

$$\tilde{\lambda}_k^\delta(m)(\tilde{\lambda}_k^\delta(m) + 1) \|x_k^\delta - x_{k-1}^\delta\|^2 \leq \frac{\Psi}{\mu} \tilde{\alpha}_k^\delta(m) \|y^\delta - F(\tilde{z}_k^\delta(m))\|^2 \quad (3.94)$$

is satisfied, then $\tilde{m}_k^\delta = \inf \emptyset = \infty$ and hence $\tilde{\lambda}_k^\delta(\tilde{m}_k^\delta)$ and $\tilde{z}_k^\delta(\tilde{m}_k^\delta)$ have to be understood in the limit sense, i.e.,

$$\tilde{\lambda}_k^\delta(\infty) := \lim_{m \rightarrow \infty} \tilde{\lambda}_k^\delta(m) = 0, \quad \tilde{z}_k^\delta(\infty) := \lim_{m \rightarrow \infty} \tilde{z}_k^\delta(m) = x_k^\delta. \quad (3.95)$$

However, since by (3.90) and (3.93) there holds $\tilde{\lambda}_k^\delta(m) \rightarrow 0$ as $m \rightarrow 0$ and since α_k^δ is bounded away from 0 in this case, $\tilde{m}_k^\delta = \infty$ can only happen if $\|y^\delta - F(\tilde{z}_k^\delta(m))\| \rightarrow 0$ as $m \rightarrow \infty$. By the continuity of the involved quantities, this in turn implies $\|y^\delta - F(\tilde{z}_k^\delta(\infty))\| = 0$ and hence, due to the discrepancy principle, the TPG method is terminated with $z_k^\delta = \tilde{z}_k^\delta(\infty)$ after the current iteration.

Combining the above considerations, for TPG methods (2.23) combined with the BTS algorithm (3.2.1) for determining a suitable sequence λ_k^δ we can now prove the following convergence result:

Theorem 3.2.4. *Assume that (3.1) and (3.70) hold and that equation $F(x) = y$ has a solution x_* in $\mathcal{B}_\rho(x_0) = \mathcal{B}_\rho(x_{-1})$. Let x_k^δ, z_k^δ be defined by (2.23) with α_k^δ being given by either (3.73) or (3.74). Let λ_k^δ be defined by Algorithm 3.2.1 with $\lambda_0^\delta = 0, m_0^\delta = 0, \mu > 1, \Psi$ as in (3.8) and $q : \mathbb{R}_0^+ \rightarrow \mathbb{R}_0^+$ satisfying (3.93). Let $k_* = k_*(\delta, y^\delta)$ be chosen according to the discrepancy principle (3.13), (3.14). Then the following statements hold:*

1. *If $y = y^\delta$, i.e., if $\delta = 0$, and if $k_* = k_*(0, y) = \infty$ then the iterates z_k and x_k converge to a solution of $F(x) = y$ as $k \rightarrow \infty$. If $\mathcal{N}(F'(x^\dagger)) \subset \mathcal{N}(F'(x))$ for all $x \in \mathcal{B}_{4\rho}(x^\dagger)$, then z_k and x_k converge to x^\dagger as $k \rightarrow \infty$.*

2. For all $(-1) \leq k < k_*$ there holds $\|x_{k+1}^\delta - x_*\| \leq \|x_k^\delta - x_*\|$. Furthermore, if, for fixed k , \tilde{m}_k^δ defined by (3.92) depends continuously on the data as $\delta \rightarrow 0$ then $z_{k_*}^\delta$ converges to a solution of $F(x) = y$ as $\delta \rightarrow 0$. If additionally $\mathcal{N}(F'(x^\dagger)) \subset \mathcal{N}(F'(x))$ for all $x \in \mathcal{B}_{4\rho}(x^\dagger)$, then $z_{k_*}^\delta$ converges to x^\dagger as $\delta \rightarrow 0$.

Proof. From Algorithm 3.2.1 it is obvious that $m_k^\delta \geq m_{k-1}^\delta + 1$ and therefore $m_k^\delta \geq k$. Using this together with (3.93), we get that

$$\begin{aligned} \sum_{k=0}^{\infty} \lambda_k^0 \|x_k - x_{k-1}\| &\leq \sum_{k=0}^{\infty} \beta_k^0(m_k^0) \|x_k - x_{k-1}\| = \sum_{k=0}^{\infty} \min \{q(m_k^0), \|x_k - x_{k-1}\|\} \\ &\leq \sum_{k=0}^{\infty} q(m_k^0) \leq \sum_{k=0}^{\infty} q(k) < \infty, \end{aligned} \tag{3.96}$$

from which it follows that (3.46) holds. Furthermore, condition (3.85) follows directly from the definition of $\lambda_k^\delta = \tilde{\lambda}_k^\delta(\tilde{m}_k^\delta)$ and due to (3.90), also $0 \leq \lambda_k^\delta \leq 1$ holds. Together with the observations made above, the first part of this theorem follows immediately from Theorem 3.1.8 and Corollary 3.1.9, as does the monotonicity result in the second part of the theorem. Furthermore, if \tilde{m}_k^δ depends continuously on the data, i.e., if, for fixed k , $\tilde{m}_k^\delta \rightarrow \tilde{m}_k^0$ as $\delta \rightarrow 0$, then by the continuity of the involved quantities, also the sequence λ_k^δ defined by Algorithm 3.2.1 depends continuously on δ for $\delta \rightarrow 0$ and fixed k . Using this, the remaining statements of the theorem now follow immediately from Theorem 3.1.10. \square

Concerning the convergence analysis above, note that we require that \tilde{m}_k^δ depends continuously on δ as $\delta \rightarrow 0$. Comparing this with the definition (3.92) of \tilde{m}_k^δ , we see that it is equivalent to requiring that the first point of intersection of the two functions

$$f^\delta(m) := \tilde{\lambda}_k^\delta(m)(\tilde{\lambda}_k^\delta(m) + 1) \|x_k^\delta - x_{k-1}^\delta\|^2 \quad \text{and} \quad g^\delta(m) := \frac{\Psi}{\mu} \tilde{\alpha}_k^\delta(m) \|y^\delta - F(\tilde{z}_k^\delta(m))\|^2$$

depends continuously on δ as $\delta \rightarrow 0$. Although this might not always necessarily be true due to pathological cases, it is reasonable to expect this to be true in practise.

The BTS algorithm 3.2.1 has one disadvantage, namely the fact that one has to calculate an infimum for determining \tilde{m}_k^δ . While this might be possible analytically for very specific problems, in general one cannot hope to be able to resolve the infimum explicitly. In order to avoid having to approximate this infimum numerically by some potentially very costly numerical routine, we introduce a numerically feasible version of the BTS algorithm, which we call *discrete backtracking search (DBTS) algorithm*. It is based on the same ideas as the BTS algorithm and takes the following form:

Algorithm 3.2.2. [Discrete backtracking search (DBTS) algorithm for λ_k^δ , $k > 1$]

- **Given:** $x_k^\delta, x_{k-1}^\delta, \tau, \Psi, \mu, y^\delta, F, q : \mathbb{R}_0^+ \rightarrow \mathbb{R}_0^+, i_{k-1} \in \mathbb{N}, j_{\max} \in \mathbb{N}$.

- Calculate $\|x_k^\delta - x_{k-1}^\delta\|$ and define

$$\beta_k(i) = \min \left\{ \frac{q(i)}{\|x_k^\delta - x_{k-1}^\delta\|}, 1 \right\}. \quad (3.97)$$

- **For:** $j = 1, \dots, j_{\max}$,

Set $\lambda_k^\delta = \beta_k(i_{k-1} + j)$.

Calculate $z_k^\delta = x_k^\delta + \lambda_k^\delta(x_k^\delta - x_{k-1}^\delta)$ and $\alpha_k^\delta = \alpha_k^\delta(z_k^\delta)$.

If: $(\|y^\delta - F(z_k^\delta)\| \leq \tau\delta)$,

$i_k = i_{k-1} + j$,

break.

Elseif: $(\lambda_k^\delta(\lambda_k^\delta + 1) \|x_k^\delta - x_{k-1}^\delta\|^2 \leq \frac{\Psi}{\mu} \alpha_k^\delta \|y^\delta - F(z_k^\delta)\|^2)$,

$i_k = i_{k-1} + j$,

break.

Else: $\lambda_k^\delta = 0$, $i_k = i_{k-1} + j_{\max}$.

End For

- **Output:** λ_k^δ , i_k .

The above algorithm is easy to implement and does not require the computation of an infimum. Furthermore, similarly to above we can show a convergence result:

Theorem 3.2.5. *Assume that (3.1) and (3.70) hold and that equation $F(x) = y$ has a solution x_* in $\mathcal{B}_\rho(x_0) = \mathcal{B}_\rho(x_{-1})$. Let x_k^δ , z_k^δ be defined by (2.23) with α_k^δ being given by either (3.73) or (3.74). Let λ_k^δ be defined by Algorithm 3.2.2 with $\lambda_0^\delta = 0$, $j_{\max} \in \mathbb{N}$, $\mu > 1$, τ as in (3.14), Ψ as in (3.8) and $q: \mathbb{R}_0^+ \rightarrow \mathbb{R}_0^+$ satisfying (3.93). Let $k_* = k_*(\delta, y^\delta)$ be chosen according to the discrepancy principle (3.13), (3.14). Then there holds:*

1. *If $y = y^\delta$, i.e., if $\delta = 0$, and if $k_* = k_*(0, y) = \infty$ then the iterates z_k and x_k converge to a solution of $F(x) = y$ as $k \rightarrow \infty$. If $\mathcal{N}(F'(x^\dagger)) \subset \mathcal{N}(F'(x))$ for all $x \in \mathcal{B}_{4\rho}(x^\dagger)$, then z_k and x_k converge to x^\dagger as $k \rightarrow \infty$.*
2. *For all $(-1) \leq k < k_*$ there holds $\|x_{k+1}^\delta - x_*\| \leq \|x_k^\delta - x_*\|$. Furthermore, if $k_*(0, y) = \infty$ and if for all $k \in \mathbb{N}$ there holds*

$$\lambda_k^0(\lambda_k^0 + 1) \|x_k - x_{k-1}\|^2 < \frac{\Psi}{\mu} \alpha_k^0 \|y - F(z_k)\|^2, \quad (3.98)$$

then $z_{k_}^\delta$ converges to a solution of $F(x) = y$ as $\delta \rightarrow 0$. If additionally $\mathcal{N}(F'(x^\dagger)) \subset \mathcal{N}(F'(x))$ for all $x \in \mathcal{B}_{4\rho}(x^\dagger)$, then $z_{k_*}^\delta$ converges to x^\dagger as $\delta \rightarrow 0$.*

Proof. The proof of this theorem is analogous to the proof of Theorem 3.2.4. Note that due to checking whether $\|y^\delta - F(z_k^\delta)\| \leq \tau\delta$, the stepsize α_k^δ is guaranteed to be well defined during the search procedure and the iteration. Furthermore, the assumption that $k_*(0, y) = \infty$ together with (3.98) and the continuity of the involved quantities implies that for fixed k , $\lambda_k^\delta \rightarrow \lambda_k^0$ as $\delta \rightarrow 0$. \square

Note that the analysis carried out above in Theorem 3.2.4 and Theorem 3.2.5 also applies to constant stepsizes $\alpha_k^\delta = \omega$, as long as $\omega \leq 1/\bar{\omega}^2$ with $\bar{\omega}$ satisfying (3.70), since for that choice, as we have already seen in the proof of Theorem 3.1.11, the results of Lemma 3.2.2 hold as well. Furthermore, in this case, the If branch in the DBTS algorithm which checks whether $\|y^\delta - F(z_k^\delta)\| \leq \tau\delta$ can be dropped, since the stepsize is now always well-defined. Consequently, also the requirement that $k_*(0, y) = \infty$ in the second part of Theorem 3.2.5 can then be removed. Hence, using a TPG method with a constant stepsize combined with the BTS algorithm for λ_k^δ gives rise to a convergent regularization method as well.

Note that in order to apply either of the backtracking search algorithms presented above one needs to have an estimate of the same parameters as for ordinary nonlinear Landweber iteration, that is, of δ and η . Whereas in ordinary Landweber iteration η only plays a role in choosing τ , here it also enters into the BTS and DBTS algorithms by Ψ . For linear problems, $\eta = 0$ can be chosen and therefore

$$\Psi = 1 - 2\tau^{-1}, \quad \text{with } \tau > 2. \quad (3.99)$$

If we take for example $\tau = 4$, then we get $\Psi = 1/2$. Note that one would want to have τ as small and Ψ as big as possible. However, since by the above equation τ and Ψ are direct proportional, one has to settle for a compromise when choosing τ . Note also that usually the exact value of η is not known. In this case, a value for η close to 0.5 is chosen in numerical algorithms requiring η explicitly.

Chapter 4

Convergence under a Local Convexity Condition

The convergence analysis of TPG methods (2.23) based on a tangential cone condition presented in the previous chapter does not cover the coupling parameter

$$\lambda_k^\delta = \frac{k-1}{k+\alpha-1}, \quad (4.1)$$

i.e., the choice originally proposed by Nesterov and the one which shows by far the best results numerically (see [37, 38, 44] and Part II of this thesis). The main reason for this is that the proof technique employed there works with the monotonicity of the iteration, i.e., the iterate x_{k+1}^δ always has to be a better approximation of a solution x_* than x_k^δ , which is not necessarily satisfied for the choice (4.1). Hence, in this chapter, we consider a different approach for proving convergence of TPG methods using the combination parameter (4.1). For this, it is necessary to replace the tangential cone condition by a local convexity assumption on the residual functional

$$\Phi^\delta(x) := \frac{1}{2} \|F(x) - y^\delta\|^2, \quad (4.2)$$

which is more natural in connection with the choice (4.1). Furthermore, we use the extended Nesterov's acceleration scheme (2.19) instead of (2.16), which leads to a slight adaptation of the TPG methods (2.23); see below.

As a motivation, note that the key ingredient for proving the fast rates (2.17) and (2.21) is the convexity of the functional $\Phi^\delta(x)$. Since, except for linear operators, we cannot hope that this holds globally, we assume that $\Phi^0(x)$, i.e., the functional $\Phi^\delta(x)$ defined by (2.5) with exact data $y = y^\delta$, corresponding to $\delta = 0$, is convex in a neighbourhood of the initial guess. This neighbourhood has to be sufficiently large encompassing the sought solution x_* , or equivalently, the initial guess x_0 has to be sufficiently close to the solution x_* . Assuming that $F(x) = y$ has a solution x_* in $\mathcal{B}_\rho(x_0)$, where, as above, $\mathcal{B}_\rho(x_0)$ denotes the closed ball with radius ρ around x_0 , the key assumption is that Φ^0 is convex in $\mathcal{B}_{6\rho}(x_0)$. As mentioned before, Nesterov's acceleration scheme yields

a non-monotonous sequence of iterates, which might possibly leave the ball $\mathcal{B}_{6\rho}(x_0)$. However, by assumption the sought for solution x_* lies in the ball $\mathcal{B}_\rho(x_0)$. Hence, defining the functional

$$\Psi(x) := \begin{cases} 0, & x \in \mathcal{B}_{2\rho}(x_0), \\ \infty, & x \notin \mathcal{B}_{2\rho}(x_0), \end{cases} \quad (4.3)$$

we can, instead of using (2.16), which would lead to algorithm (2.22), use (2.19), noting that still the fast rate (2.21) can be expected for $\delta = 0$. This leads to the algorithm

$$\begin{aligned} z_k^\delta &= x_k^\delta + \frac{k-1}{k+\alpha-1}(x_k^\delta - x_{k-1}^\delta), \\ x_{k+1}^\delta &= \text{prox}_{\omega\Psi} \left(z_k^\delta + \omega F'(z_k^\delta)^*(y^\delta - F(z_k^\delta)) \right), \\ x_0^\delta &= x_{-1}^\delta = x_0, \end{aligned} \quad (4.4)$$

which we consider throughout this chapter. The presented research is taken from [39].

4.1 Convergence Analysis II

In this section, we provide a convergence analysis of method (4.4). Concerning notation, whenever we consider the noise-free case $y = y^\delta$ corresponding to $\delta = 0$, we replace δ by 0 in all variables depending on δ , e.g., we write Φ^0 instead of Φ^δ . For carrying out the analysis, we have to make a set of assumptions, already indicated above.

Assumption 4.1.1. Let ρ be a positive number such that $\mathcal{B}_{6\rho}(x_0) \subset \mathcal{D}(F)$.

1. The operator $F : \mathcal{D}(F) \subset \mathcal{X} \rightarrow \mathcal{Y}$ is continuously Fréchet differentiable between the real Hilbert spaces \mathcal{X} and \mathcal{Y} with inner products $\langle \cdot, \cdot \rangle$ and norms $\|\cdot\|$. Furthermore, let F be weakly sequentially closed on $\mathcal{B}_{2\rho}(x_0)$.
2. The equation $F(x) = y$ has a solution $x_* \in \mathcal{B}_\rho(x_0)$.
3. The data y^δ satisfies $\|y - y^\delta\| \leq \delta$.
4. The functional Φ^0 defined by (2.5) with $\delta = 0$ is convex and has a Lipschitz continuous gradient $\nabla\Phi^0$ with Lipschitz constant L on $\mathcal{B}_{6\rho}(x_0)$, i.e.,

$$\Phi^0(\lambda x_1 + (1 - \lambda)x_2) \leq \lambda\Phi^0(x_1) + (1 - \lambda)\Phi^0(x_2), \quad \forall x_1, x_2 \in \mathcal{B}_{6\rho}(x_0), \quad (4.5)$$

$$\|\nabla\Phi^0(x_1) - \nabla\Phi^0(x_2)\| \leq L \|x_1 - x_2\|, \quad \forall x_1, x_2 \in \mathcal{B}_{6\rho}(x_0). \quad (4.6)$$

5. For α in (4.4) there holds $\alpha > 3$ and the scaling parameter ω satisfies $0 < \omega < \frac{1}{L}$.

Note that since $\mathcal{B}_{2\rho}(x_0)$ is weakly closed and given the continuity of F , a sufficient condition for the weak sequential closedness assumption to hold is that F is compact. We now turn to the convergence analysis of Nesterov's accelerated gradient method (4.4). Throughout this analysis, if not explicitly stated otherwise, Assumption 4.1.1

is in force. Note first that from F being continuously Fréchet differentiable, we can derive that there exists an $\bar{\omega}$ such that

$$\|F'(x)\| \leq \bar{\omega}, \quad \forall x \in \mathcal{B}_{6\rho}(x_0). \quad (4.7)$$

Next, note that since $\mathcal{B}_{2\rho}(x)$ denotes a closed ball around x , the functional Ψ , in addition to being proper and convex, is also lower-semicontinuous, an assumption required in the proofs in [3], which we need in various places of this chapter. Furthermore, it immediately follows from the definition (2.20) of the proximal operator $\text{prox}_{\omega\Psi}(\cdot)$ that

$$\text{prox}_{\omega\Psi}(x) = \arg \min_{u \in \mathcal{X}} \left\{ \omega\Psi(u) + \frac{1}{2} \|x - u\|^2 \right\} = \arg \min_{u \in \mathcal{B}_{2\rho}(x_0)} \left\{ \frac{1}{2} \|x - u\|^2 \right\}, \quad (4.8)$$

since Ψ defined by (4.3) is equal to ∞ outside $\mathcal{B}_{2\rho}(x_0)$. Hence, since obviously $\mathcal{B}_{2\rho}(x_0)$ is a convex set, $\text{prox}_{\omega\Psi}(\cdot)$ is nothing else than the metric projection onto $\mathcal{B}_{2\rho}(x_0)$, and is therefore Lipschitz continuous with Lipschitz constant smaller or equal to 1. Consequently, given an estimate of ρ , the implementation of $\text{prox}_{\omega\Psi}(\cdot)$ is exceedingly simple in this setting, and therefore, one iteration step of (4.4) and (2.4) require roughly the same amount of computational effort.

Finally, note that due to the convexity of Φ^0 , the set S defined by

$$\mathcal{S} := \{x \in \mathcal{B}_{2\rho}(x_0) \mid F(x) = y\}, \quad (4.9)$$

is a convex subset of $\mathcal{B}_{2\rho}(x_0)$ and hence, there exists a unique x_0 -minimum-norm solution x^\dagger , which is defined by

$$x^\dagger := \arg \min_{x \in \mathcal{S}} \|x - x_0\|, \quad (4.10)$$

which is nothing else than the orthogonal projection of x_0 onto the set \mathcal{S} .

The following convergence analysis is largely based on the ideas of the paper [3] of Attouch and Peypouquet, which we reference from frequently throughout this analysis. Following their arguments, we start by making the following

Definition 4.1.1. For Φ^δ and Ψ defined by (2.5) and (4.3), we define

$$\Theta^\delta(x) := \Phi^\delta(x) + \Psi(x). \quad (4.11)$$

The energy functional \mathcal{E}^δ is defined by

$$\mathcal{E}^\delta(k) := \frac{2\omega}{\alpha - 1} (k + \alpha - 2)^2 (\Theta^\delta(x_k^\delta) - \Theta^\delta(x_*)) + (\alpha - 1) \|w_k^\delta - x_*\|^2, \quad (4.12)$$

where the sequence w_k^δ is defined by

$$w_k^\delta := \frac{k + \alpha - 1}{\alpha - 1} z_k^\delta - \frac{k}{\alpha - 1} x_k^\delta = x_k^\delta + \frac{k - 1}{\alpha - 1} (x_k^\delta - x_{k-1}^\delta). \quad (4.13)$$

Furthermore, we introduce the operator $G_\omega^\delta : \mathcal{D}(F) \subset \mathcal{X} \rightarrow \mathcal{Y}$, given by

$$G_\omega^\delta(x) := \frac{1}{\omega} (x - \text{prox}_{\omega\Psi}(x - \omega\nabla\Phi^\delta(x))). \quad (4.14)$$

Using Definition 4.1.1, we can now write to update step for x_{k+1}^δ in the form

$$x_{k+1}^\delta = z_k^\delta - \omega G_\omega^\delta(z_k^\delta),$$

and furthermore, it is possible to write

$$w_{k+1}^\delta = \frac{k + \alpha - 1}{\alpha - 1} (z_k^\delta - \omega G_\omega^\delta(z_k^\delta)) - \frac{k}{\alpha - 1} x_k^\delta = w_k^\delta - \frac{\omega}{\alpha - 1} (k + \alpha - 1) G_\omega^\delta(z_k^\delta). \quad (4.15)$$

As a first result, we show that both z_k^δ and x_k^δ stay within $\mathcal{B}_{6\rho}(x_0)$ during the iteration.

Lemma 4.1.1. *Under the Assumption 4.1.1, the sequence of iterates x_k^δ and z_k^δ defined by (4.4) is well-defined. Furthermore, $x_k^\delta \in \mathcal{B}_{2\rho}(x_0)$ and $z_k^\delta \in \mathcal{B}_{6\rho}(x_0)$ for all $k \in \mathbb{N}$.*

Proof. This follows by induction from $x_0^\delta = x_{-1}^\delta = x_0 \in \mathcal{B}_\rho(x_0)$, the observation

$$\begin{aligned} \|z_k^\delta - x_0\| &\leq \left(1 + \frac{k-1}{k+\alpha-1}\right) \|x_k^\delta - x_0\| + \frac{k-1}{k+\alpha-1} \|x_{k-1}^\delta - x_0\| \\ &\leq 2 \|x_k^\delta - x_0\| + \|x_{k-1}^\delta - x_0\|, \end{aligned}$$

and the fact that by the definition of $\text{prox}_{\omega\Psi}(x)$, x_k^δ is always an element of $\mathcal{B}_{2\rho}(x_0)$. \square

Since the functional Θ^0 is assumed to be convex in $\mathcal{B}_{6\rho}(x_0)$, we can deduce:

Lemma 4.1.2. *Under Assumption 4.1.1, for all $x, z \in \mathcal{B}_{6\rho}(x_0)$ there holds*

$$\Theta^0(z - \omega G_\omega^0(z)) \leq \Theta^0(x) + \langle G_\omega^0(z), z - x \rangle - \frac{\omega}{2} \|G_\omega^0(z)\|^2.$$

Proof. This lemma is also used in [3]. However, the sources for it cited there do not exactly cover our setting with Φ^δ being defined on $\mathcal{D}(F) \subset \mathcal{X}$ only. Hence, we here give an elementary proof of the assertion. Note first that due to the Lipschitz continuity of Φ^0 in $\mathcal{B}_{6\rho}(x_0)$ and the fact that $\omega < 1/L$ we have

$$\Phi^0(u) \leq \Phi^0(v) + \langle \nabla \Phi^0(v), u - v \rangle + \frac{1}{2\omega} \|u - v\|^2, \quad \forall u, v \in \mathcal{B}_{6\rho}(x_0).$$

Now since Φ^0 is convex on $\mathcal{B}_{6\rho}(x_0)$, also have [6]

$$\Phi^0(v) + \langle \nabla \Phi^0(v), w - v \rangle \leq \Phi^0(w), \quad \forall v, w \in \mathcal{B}_{6\rho}(x_0),$$

and therefore, combining the above two inequalities, we get

$$\Phi^0(u) \leq \Phi^0(w) + \langle \nabla \Phi^0(v), u - w \rangle + \frac{1}{2\omega} \|u - v\|^2, \quad \forall u, v, w \in \mathcal{B}_{6\rho}(x_0).$$

Using this result for $u = z - \omega G_\omega^0(z)$, $v = z$, $w = x$, noting that for $x, z \in \mathcal{B}_{6\rho}(x_0)$ there holds $u, v, w \in \mathcal{B}_{6\rho}(x_0)$, we get

$$\Phi^0(z - \omega G_\omega^0(z)) \leq \Phi^0(x) + \langle \nabla \Phi^0(z), z - \omega G_\omega^0(z) - x \rangle + \frac{\omega}{2} \|G_\omega^0(z)\|^2. \quad (4.16)$$

Next, note that since $z - \omega G_\omega^0(z) = \text{prox}_{\omega\Psi}(z - \omega\nabla\Phi^0(z))$, a standard result from proximal operator theory [6, Proposition 12.26] implies that there holds

$$\begin{aligned} \Psi(z - \omega G_\omega^0(z)) &\leq \Psi(x) + \frac{1}{\omega} \langle (z - \omega G_\omega^0(z)) - x, (z - \omega\nabla\Phi^0(z)) - (z - \omega G_\omega^0(z)) \rangle \\ &= \Psi(x) + \langle z - \omega G_\omega^0(z) - x, -\nabla\Phi^0(z) + G_\omega^0(z) \rangle \\ &= \Psi(x) - \langle z - \omega G_\omega^0(z) - x, \nabla\Phi^0(z) \rangle + \langle z - x, G_\omega^0(z) \rangle - \omega \|G_\omega^0(z)\|^2. \end{aligned}$$

Adding this inequality to (4.16) and using the fact that by definition $\Theta^0 = \Phi^0 + \Psi$ immediately yields the assertion. \square

We want to derive a similar inequality also for the functionals Θ^δ . The following lemma is of vital importance for doing that:

Lemma 4.1.3. *Let Assumption 4.1.1 hold, let $x, z \in \mathcal{B}_{6\rho}(x_0)$ and define*

$$\begin{aligned} R_1 &:= \Theta^0(z - \omega G_\omega^\delta(z)) - \Theta^0(z - \omega G_\omega^0(z)), \\ R_2 &:= \Theta^\delta(z - \omega G_\omega^\delta(z)) - \Theta^0(z - \omega G_\omega^\delta(z)), \\ R_3 &:= \Theta^0(x) - \Theta^\delta(x), \quad R_4 := \langle G_\omega^0(z) - G_\omega^\delta(z), z - x \rangle, \\ R_5 &:= \frac{\omega}{2} \left(\|G_\omega^\delta(z)\|^2 - \|G_\omega^0(z)\|^2 \right), \end{aligned} \tag{4.17}$$

as well as

$$R := R_1 + R_2 + R_3 + R_4 + R_5. \tag{4.18}$$

Then there holds

$$\Theta^\delta(z - \omega G_\omega^\delta(z)) \leq \Theta^\delta(x) + \langle G_\omega^\delta(z), z - x \rangle - \frac{\omega}{2} \|G_\omega^\delta(z)\|^2 + R.$$

Proof. Using Lemma 4.1.2 we get

$$\begin{aligned} \Theta^\delta(z - \omega G_\omega^\delta(z)) &= \Theta^0(z - \omega G_\omega^0(z)) + R_1 + R_2 \\ &\leq \Theta^0(x) + \langle G_\omega^0(z), z - x \rangle - \frac{\omega}{2} \|G_\omega^0(z)\|^2 + R_1 + R_2 \\ &= \Theta^\delta(x) + \langle G_\omega^\delta(z), z - x \rangle - \frac{\omega}{2} \|G_\omega^\delta(z)\|^2 + R_1 + R_2 + R_3 + R_4 + R_5, \end{aligned}$$

from which the statement of the theorem immediately follows. \square

Next, we show that the R_i and hence, also R , can be bounded in terms of $\delta + \delta^2$.

Proposition 4.1.4. *Let Assumption 4.1.1 hold, let $x \in \mathcal{B}_{2\rho}(x_0)$ and $z \in \mathcal{B}_{6\rho}(x_0)$ and let the R_1, \dots, R_5 be defined by (4.18). Then there holds*

$$\begin{aligned} R_1 &\leq \frac{1}{2}\bar{\omega}^4\omega^2\delta^2 + 2\bar{\omega}^3\omega\rho\delta, \\ R_2 &\leq \frac{3}{2}\delta^2 + 2\rho\bar{\omega}\delta, \\ R_3 &\leq \frac{3}{2}\delta^2 + 2\rho\bar{\omega}\delta, \\ R_4 &\leq 8\rho\bar{\omega}\delta, \\ R_5 &\leq \frac{\omega}{2}\bar{\omega}^2\delta^2 + 8\rho\bar{\omega}\delta. \end{aligned}$$

Proof. The following somewhat long but elementary proof uses mainly the boundedness and Lipschitz continuity assumptions made above. For the following, let $x \in \mathcal{B}_{2\rho}(x_0)$ and $z \in \mathcal{B}_{6\rho}(x_0)$. We treat each of the R_i terms separately, starting with

$$\begin{aligned}
 R_1 &= \Theta^0(z - \omega G_\omega^\delta(z)) - \Theta^0(z - \omega G_\omega^0(z)) \\
 &= \frac{1}{2} \|F(z - \omega G_\omega^\delta(z)) - y\|^2 - \frac{1}{2} \|F(z - \omega G_\omega^0(z)) - y\|^2 \\
 &= \frac{1}{2} \|F(z - \omega G_\omega^\delta(z)) - F(z - \omega G_\omega^0(z))\|^2 \\
 &\quad - \langle F(z - \omega G_\omega^\delta(z)) - F(z - \omega G_\omega^0(z)), F(z - \omega G_\omega^0(z)) - y \rangle \\
 &\leq \frac{1}{2} \|F(z - \omega G_\omega^\delta(z)) - F(z - \omega G_\omega^0(z))\|^2 \\
 &\quad + \|F(z - \omega G_\omega^\delta(z)) - F(z - \omega G_\omega^0(z))\| \|F(z - \omega G_\omega^0(z)) - y\|.
 \end{aligned}$$

Since we have

$$\begin{aligned}
 \|F(z - \omega G_\omega^\delta(z)) - F(z - \omega G_\omega^0(z))\| &\leq \bar{\omega} \|\omega G_\omega^\delta(z) - \omega G_\omega^0(z)\| \\
 &\leq \bar{\omega} \|\text{prox}_{\omega\Psi}(z - \omega\nabla\Phi^\delta(z)) - \text{prox}_{\omega\Psi}(z - \omega\nabla\Phi(z))\| \\
 &\leq \bar{\omega} \omega \|\nabla\Phi^\delta(z) - \nabla\Phi(z)\| \\
 &= \bar{\omega} \omega \|F'(z)^*(y - y^\delta)\| \leq \bar{\omega}^2 \omega \|y - y^\delta\| \leq \bar{\omega}^2 \omega \delta,
 \end{aligned}$$

and

$$\|F(z - \omega G_\omega^0(z)) - y\| \leq \bar{\omega} \|\text{prox}_{\omega\Psi}(z - \omega\nabla\Phi^\delta(z)) - x_*\| \leq 2\rho\bar{\omega},$$

there holds

$$R_1 \leq \frac{1}{2}(\bar{\omega}^2 \omega \delta)^2 + (\bar{\omega}^2 \omega \delta)2\rho\bar{\omega} = \left(\frac{1}{2}\bar{\omega}^4 \omega^2\right) \delta^2 + (2\bar{\omega}^3 \omega \rho) \delta.$$

Next, we look at

$$\begin{aligned}
 R_2 &= \Theta^\delta(z - \omega G_\omega^\delta(z)) - \Theta^0(z - \omega G_\omega^\delta(z)) \\
 &= \frac{1}{2} \|y - y^\delta\|^2 + \langle F(z - \omega G_\omega^\delta(z)) - y^\delta, y - y^\delta \rangle \\
 &= \frac{3}{2} \|y - y^\delta\|^2 + \langle F(z - \omega G_\omega^\delta(z)) - y, y - y^\delta \rangle \\
 &\leq \frac{3}{2} \delta^2 + \|F(z - \omega G_\omega^\delta(z)) - F(x_*)\| \delta \\
 &\leq \frac{3}{2} \delta^2 + 2\rho\bar{\omega} \delta.
 \end{aligned}$$

Similarly to above, for the next term we get

$$\begin{aligned}
 R_3 &= \Theta^0(x) - \Theta^\delta(x) = \frac{1}{2} \|F(x) - y\|^2 - \frac{1}{2} \|F(x) - y^\delta\|^2 \\
 &= \frac{1}{2} \|y - y^\delta\|^2 + \langle F(x) - y^\delta, y - y^\delta \rangle \\
 &= \frac{3}{2} \|y - y^\delta\|^2 + \langle F(x) - y, y - y^\delta \rangle \\
 &\leq \frac{3}{2} \delta^2 + \|F(x) - F(x_*)\| \delta \\
 &\leq \frac{3}{2} \delta^2 + 2\rho\bar{\omega} \delta.
 \end{aligned}$$

Furthermore, together with the Lipschitz continuity of $\text{prox}_{\omega\Psi}(\cdot)$, we get

$$\begin{aligned}
 R_4 &= \langle G_\omega^0(z) - G_\omega^\delta(z), z - x \rangle \\
 &= \frac{1}{\omega} \langle \text{prox}_{\omega\Psi}(z - \omega\nabla\Phi^\delta(z)) - \text{prox}_{\omega\Psi}(z - \omega\nabla\Phi^0(z)), z - x \rangle \\
 &\leq \frac{1}{\omega} \|\text{prox}_{\omega\Psi}(z - \omega\nabla\Phi^\delta(z)) - \text{prox}_{\omega\Psi}(z - \omega\nabla\Phi^0(z))\| \|z - x\| \\
 &\leq \|\nabla\Phi^\delta(z) - \nabla\Phi^0(z)\| \|z - x\| \leq 8\rho \|F'(z)(y - y^\delta)\| \leq 8\rho\bar{\omega}\delta.
 \end{aligned}$$

Finally, for the last term, we get

$$\begin{aligned}
 R_5 &= \frac{\omega}{2} \left(\|G_\omega^\delta(z)\|^2 - \|G_\omega^0(z)\|^2 \right) \\
 &= \frac{\omega}{2} \|G_\omega^\delta(z) - G_\omega^0(z)\|^2 + \omega \langle G_\omega^\delta(z) - G_\omega^0(z), G_\omega^0(z) \rangle \\
 &\leq \frac{\omega}{2} \|G_\omega^\delta(z) - G_\omega^0(z)\|^2 + \omega \|G_\omega^\delta(z) - G_\omega^0(z)\| \|G_\omega^0(z)\| \\
 &\leq \frac{\omega}{2} \bar{\omega}^2 \delta^2 + \omega \bar{\omega} \delta \|G_\omega^0(z)\| \leq \frac{\omega}{2} \bar{\omega}^2 \delta^2 + 8\rho\bar{\omega}\delta,
 \end{aligned}$$

which concludes the proof. \square

As an immediate consequence, we get the following

Corollary 4.1.5. *Let Assumption 4.1.1 hold and let $x, z \in \mathcal{B}_{6\rho}(x_0)$. If we define*

$$\begin{aligned}
 c_1 &= 2\bar{\omega}^3\omega\rho + 20\rho\bar{\omega}, \\
 c_2 &= 3 + \frac{1}{2}\bar{\omega}^4\omega^2 + \frac{1}{2}\omega\bar{\omega}^2,
 \end{aligned} \tag{4.19}$$

then there holds

$$\Theta^\delta(z - \omega G_\omega^\delta(z)) \leq \Theta^\delta(x) + \langle G_\omega^\delta(z), z - x \rangle - \frac{\omega}{2} \|G_\omega^\delta(z)\|^2 + c_1\delta + c_2\delta^2.$$

Proof. This immediately follows from Lemma 4.1.2 and Proposition 4.1.4. \square

Combining the above, we are now able to arrive at the following important result:

Proposition 4.1.6. *Let Assumption 4.1.1 hold, let the sequence of iterates x_k^δ and z_k^δ be given by (4.4) and let c_1 and c_2 be defined by (4.19). If we define*

$$\Delta(\delta) := c_1\delta + c_2\delta^2, \tag{4.20}$$

then there holds

$$\Theta^\delta(z_k^\delta - \omega G_\omega^\delta(z_k^\delta)) \leq \Theta^\delta(x_k^\delta) + \langle G_\omega^\delta(z_k^\delta), z_k^\delta - x_k^\delta \rangle - \frac{\omega}{2} \|G_\omega^\delta(z_k^\delta)\|^2 + \Delta(\delta), \tag{4.21}$$

$$\Theta^\delta(z_k^\delta - \omega G_\omega^\delta(z_k^\delta)) \leq \Theta^\delta(x_*) + \langle G_\omega^\delta(z_k^\delta), z_k^\delta - x_* \rangle - \frac{\omega}{2} \|G_\omega^\delta(z_k^\delta)\|^2 + \Delta(\delta). \tag{4.22}$$

Proof. This immediately follows from Lemma 4.1.1 and Corollary 4.1.5. \square

Using the above proposition, we are now able to derive the important

Theorem 4.1.7. *Let Assumption 4.1.1 hold and let the sequence of iterates x_k^δ and z_k^δ be given by (4.4) and let $\Delta(\delta)$ be defined by (4.20). Then there holds*

$$\mathcal{E}^\delta(k+1) + \frac{2\omega}{\alpha-1} (k(\alpha-3) (\Theta^\delta(x_k^\delta) - \Theta^\delta(x_*)) - (k+\alpha-1)^2 \Delta(\delta)) \leq \mathcal{E}^\delta(k). \quad (4.23)$$

Proof. This proof is adapted from the corresponding result in [3], the difference being the term $\Delta(\delta)$. We start by multiplying inequality (4.21) by $\frac{k}{k+\alpha-1}$ and inequality (4.22) by $\frac{\alpha-1}{k+\alpha-1}$. Adding the results and using the fact that $x_{k+1}^\delta = z_k^\delta - \omega G_\omega^\delta(z_k^\delta)$, we get

$$\begin{aligned} \Theta^\delta(x_{k+1}^\delta) &\leq \frac{k}{k+\alpha-1} \Theta^\delta(x_k^\delta) + \frac{\alpha-1}{k+\alpha-1} \Theta^\delta(x_*) - \frac{\omega}{2} \|G_\omega^\delta(z_k^\delta)\|^2 + \Delta(\delta) \\ &\quad + \left\langle G_\omega^\delta(z_k^\delta), \frac{k}{k+\alpha-1} (z_k^\delta - x_k^\delta) + \frac{\alpha-1}{k+\alpha-1} (z_k^\delta - x_*) \right\rangle. \end{aligned}$$

Since

$$\frac{k}{k+\alpha-1} (z_k^\delta - x_k^\delta) + \frac{\alpha-1}{k+\alpha-1} (z_k^\delta - x_*) = \frac{\alpha-1}{k+\alpha-1} (w_k^\delta - x_*),$$

we obtain

$$\begin{aligned} \Theta^\delta(x_{k+1}^\delta) &\leq \frac{k}{k+\alpha-1} \Theta^\delta(x_k^\delta) + \frac{\alpha-1}{k+\alpha-1} \Theta^\delta(x_*) - \frac{\omega}{2} \|G_\omega^\delta(z_k^\delta)\|^2 + \Delta(\delta) \\ &\quad + \frac{\alpha-1}{k+\alpha-1} \langle G_\omega^\delta(z_k^\delta), w_k^\delta - x_* \rangle. \end{aligned} \quad (4.24)$$

Next, observe that it follows from (4.15) that

$$w_{k+1}^\delta - x_* = w_k^\delta - x_* - \frac{\omega}{\alpha-1} (k+\alpha-1) G_\omega^\delta(z_k^\delta).$$

After developing

$$\begin{aligned} \|w_{k+1}^\delta - x_*\|^2 &= \|w_k^\delta - x_*\|^2 - 2 \frac{\omega}{\alpha-1} (k+\alpha-1) \langle w_k^\delta - x_*, G_\omega^\delta(z_k^\delta) \rangle \\ &\quad + \frac{\omega^2}{(\alpha-1)^2} (k+\alpha-1)^2 \|G_\omega^\delta(z_k^\delta)\|^2, \end{aligned}$$

and multiplying the above expression by $\frac{(\alpha-1)^2}{2\omega(k+\alpha-1)^2}$, we get

$$\begin{aligned} &\frac{(\alpha-1)^2}{2\omega(k+\alpha-1)^2} \left(\|w_k^\delta - x_*\|^2 - \|w_{k+1}^\delta - x_*\|^2 \right) \\ &= \frac{\alpha-1}{k+\alpha-1} \langle G_\omega^\delta(z_k^\delta), w_k^\delta - x_* \rangle - \frac{\omega}{2} \|G_\omega^\delta(z_k^\delta)\|^2. \end{aligned}$$

Replacing this in inequality (4.24) above, we get

$$\begin{aligned} \Theta^\delta(x_{k+1}^\delta) &\leq \frac{k}{k+\alpha-1} \Theta^\delta(x_k^\delta) + \frac{\alpha-1}{k+\alpha-1} \Theta^\delta(x_*) + \Delta(\delta) \\ &\quad + \frac{(\alpha-1)^2}{2\omega(k+\alpha-1)^2} \left(\|w_k^\delta - x_*\|^2 - \|w_{k+1}^\delta - x_*\|^2 \right). \end{aligned}$$

Equivalently, we can write this as

$$\begin{aligned} \Theta^\delta(x_{k+1}^\delta) - \Theta^\delta(x_*) &\leq \frac{k}{k+\alpha-1} (\Theta^\delta(x_k^\delta) - \Theta^\delta(x_*)) + \Delta(\delta) \\ &\quad + \frac{(\alpha-1)^2}{2\omega(k+\alpha-1)^2} \left(\|w_k^\delta - x_*\|^2 - \|w_{k+1}^\delta - x_*\|^2 \right). \end{aligned}$$

Multiplying by $\frac{2\omega}{\alpha-1}(k+\alpha-1)^2$, we obtain

$$\begin{aligned} \frac{2\omega}{\alpha-1}(k+\alpha-1)^2 (\Theta^\delta(x_{k+1}^\delta) - \Theta^\delta(x_*)) &\leq \frac{2\omega}{\alpha-1} k(k+\alpha-1) (\Theta^\delta(x_k^\delta) - \Theta^\delta(x_*)) \\ &\quad + \frac{2\omega}{\alpha-1} (k+\alpha-1)^2 \Delta(\delta) + (\alpha-1) \left(\|w_k^\delta - x_*\|^2 - \|w_{k+1}^\delta - x_*\|^2 \right), \end{aligned}$$

and therefore, since there holds

$$k(k+\alpha-1) = (k+\alpha-1)^2 - k(\alpha-3) - (\alpha-2)^2 \leq (k+\alpha-1)^2 - k(\alpha-3),$$

we get that

$$\begin{aligned} \frac{2\omega}{\alpha-1}(k+\alpha-1)^2 (\Theta^\delta(x_{k+1}^\delta) - \Theta^\delta(x_*)) &\leq -\frac{2\omega}{\alpha-1} k(\alpha-3) (\Theta^\delta(x_k^\delta) - \Theta^\delta(x_*)) \\ &\quad + \frac{2\omega}{\alpha-1} (k+\alpha-1)^2 (\Theta^\delta(x_k^\delta) - \Theta^\delta(x_*)) + \frac{2\omega}{\alpha-1} (k+\alpha-1)^2 \Delta(\delta) \\ &\quad + (\alpha-1) \left(\|w_k^\delta - x_*\|^2 - \|w_{k+1}^\delta - x_*\|^2 \right). \end{aligned}$$

Together with the definition (4.12) of \mathcal{E}^δ , this implies

$$\mathcal{E}^\delta(k+1) + \frac{2\omega}{\alpha-1} k(\alpha-3) (\Theta^\delta(x_k^\delta) - \Theta^\delta(x_*)) \leq \mathcal{E}^\delta(k) + \frac{2\omega}{\alpha-1} (k+\alpha-1)^2 \Delta(\delta),$$

or equivalently, after rearranging, we get

$$\mathcal{E}^\delta(k+1) + \frac{2\omega}{\alpha-1} (k(\alpha-3) (\Theta^\delta(x_k^\delta) - \Theta^\delta(x_*)) - (k+\alpha-1)^2 \Delta(\delta)) \leq \mathcal{E}^\delta(k),$$

which concludes the proof. \square

Inequality (4.23) is the key ingredient for showing that (4.4), combined with a suitable stopping rule, gives rise to a convergent regularization method. In order to derive a

suitable stopping rule, note first that in the case of exact data, i.e., $\delta = 0$, inequality (4.23) reduces to

$$\mathcal{E}^0(k+1) + \frac{2\omega}{\alpha-1}k(\alpha-3) (\Theta^0(x_k^0) - \Theta^0(x_*)) \leq \mathcal{E}^0(k). \quad (4.25)$$

Since by Assumption 4.1.1 the functional Φ^0 is convex, the arguments used in [3] are applicable, and we can deduce the following:

Theorem 4.1.8. *Let Assumption 4.1.1 hold, let the sequence of iterates x_k^0 and z_k^0 be given by (4.4) with exact data $y = y^\delta$, i.e., $\delta = 0$ and let \mathcal{S} be defined by (4.9). Then the following statements hold:*

- The sequence $(\mathcal{E}^0(k))$ is non-increasing and $\lim_{k \rightarrow \infty} \mathcal{E}^0(k)$ exists.

- For each $k \geq 0$, there holds

$$\|F(x_k^0) - y\|^2 \leq \frac{(\alpha-1)\mathcal{E}^0(0)}{\omega(k+\alpha-2)^2}, \quad \|w_k^0 - x_*\|^2 \leq \frac{\mathcal{E}^0(0)}{\alpha-1}.$$

- There holds

$$\sum_{k=1}^{\infty} k \|F(x_k^0) - y\|^2 \leq \frac{(\alpha-1)\mathcal{E}^0(1)}{\omega(\alpha-3)},$$

as well as

$$\sum_{k=1}^{\infty} k \|x_{k+1}^0 - x_k^0\|^2 \leq \frac{(\alpha-1)\mathcal{E}^0(1)}{\omega(\alpha-3)}.$$

- There holds

$$\liminf_{k \rightarrow \infty} \left(k^2 \ln(k) \|F(x_k^0) - y\|^2 \right) = 0,$$

as well as

$$\liminf_{k \rightarrow \infty} \left(k \ln(k) \|x_{k+1}^0 - x_k^0\|^2 \right) = 0.$$

- There exists an \tilde{x} in \mathcal{S} , such that the sequence (x_k^0) converges weakly to \tilde{x} , i.e.,

$$\lim_{\delta \rightarrow 0} \langle x_k^0, h \rangle = \langle \tilde{x}, h \rangle, \quad \forall h \in \mathcal{X}. \quad (4.26)$$

Proof. The statements follow from Facts 1-4, Remark 2 and Theorem 3 in [3]. \square

Thanks to Theorem 4.1.8, we now know that Nesterov's accelerated gradient method (4.4) converges weakly to a solution \tilde{x} from the solution set \mathcal{S} in case of exact data $y = y^\delta$, i.e., $\delta = 0$.

Hence, it remains to consider the behaviour of (4.4) in the case of inexact data y^δ . As mentioned above, the key for doing so is inequality (4.23). We want to use it to

show that, similarly to the exact data case, the sequence $(\mathcal{E}^\delta(k))$ is non-increasing up to some $k \in \mathbb{N}$. To do this, note first that $\mathcal{E}^\delta(k)$ is positive as long as

$$\Theta^\delta(x_k^\delta) \geq \Theta^\delta(x_*),$$

which is true, as long as

$$\|F(x_k^\delta) - y^\delta\| \geq \delta. \quad (4.27)$$

On the other hand, the term

$$\frac{2\omega}{\alpha - 1} (k(\alpha - 3) (\Theta^\delta(x_k^\delta) - \Theta^\delta(x_*)) - (k + \alpha - 1)^2 \Delta(\delta)) \quad (4.28)$$

in (4.23) is positive, as long as

$$\Theta^\delta(x_k^\delta) - \Theta^\delta(x_*) \geq \frac{(k + \alpha - 1)^2}{k(\alpha - 3)} \Delta(\delta),$$

which is satisfied, as long as

$$\|F(x_k^\delta) - y^\delta\|^2 \geq \frac{2(k + \alpha - 1)^2}{k(\alpha - 3)} \Delta(\delta) + \delta^2, \quad (4.29)$$

which obviously implies (4.27). These considerations suggest, given a small $\tau > 1$, to choose the stopping index $k_* = k_*(\delta, y^\delta)$ as the smallest integer such that

$$\|F(x_{k_*}^\delta) - y^\delta\|^2 \leq \frac{2(k + \alpha - 1)^2}{k(\alpha - 3)} \Delta(\delta) + \tau^2 \delta^2 < \|F(x_k^\delta) - y^\delta\|^2, \quad k_* > k. \quad (4.30)$$

Concerning the well-definedness of k_* , we are able to prove the following

Lemma 4.1.9. *Let Assumption 4.1.1 hold, let the sequence of iterates x_k^δ and z_k^δ be given by (4.4) and let c_1 and c_2 be defined by (4.19). Then the stopping index k_* defined by (4.30) with $\tau > 1$ is well-defined and there holds*

$$k_* = \mathcal{O}(\delta^{-1}), \quad (4.31)$$

Proof. By the definition (4.20) of $\Delta(\delta)$ and due to

$$\|F(x_k^\delta) - y^\delta\|^2 \leq (\|F(x_k^\delta) - y\| + \|y - y^\delta\|)^2 \leq (2\bar{\omega}\rho + \delta)^2,$$

it follows from (4.30) that for all $k < k_*$ there holds

$$\frac{2(k + \alpha - 1)^2}{k(\alpha - 3)} (c_1\delta + c_2\delta^2) + \tau^2\delta^2 \leq (2\bar{\omega}\rho + \delta)^2,$$

which can be rewritten as

$$\frac{(k + \alpha - 1)^2}{k(\alpha - 3)} (c_1\delta + c_2\delta^2) \leq 2\bar{\omega}^2\rho^2 + 2\bar{\omega}\rho\delta + (1 - \tau^2)\delta^2 \leq 2\bar{\omega}^2\rho^2 + 2\bar{\omega}\rho\delta, \quad (4.32)$$

where we have used that $\tau > 1$. Since the left hand side in the above inequality goes to ∞ for $k \rightarrow \infty$, while the right hand side stays bounded, it follows that k_* is finite and hence well-defined for $\delta \neq 0$. Furthermore, since

$$\frac{(k + \alpha - 1)^2}{k(\alpha - 3)} \geq \frac{k}{2(\alpha - 3)},$$

which can see by multiplying the above inequality by $k(\alpha - 3)$, and since (4.32) also holds for $k = k_* - 1$, we get

$$\frac{k_* - 1}{2(\alpha - 3)}(c_1\delta + c_2\delta^2) \leq 2\bar{\omega}^2\rho^2 + 2\bar{\omega}\rho\delta.$$

Reordering the terms, we arrive at

$$k_* \leq 2(\alpha - 3) \left(\frac{2\bar{\omega}^2\rho^2 + 2\bar{\omega}\rho\delta}{c_1\delta + c_2\delta^2} \right) + 1.$$

from which the assertion now immediately follows. \square

The rate $k_* = \mathcal{O}(\delta^{-1})$ given in (4.31) for the iteration method (4.4) should be compared with the corresponding result [46, Corollary 2.3] for Landweber iteration (2.4), where one only obtains $k_* = \mathcal{O}(\delta^{-2})$. In order to obtain the rate $k_* = \mathcal{O}(\delta^{-1})$ for Landweber iteration, apart from others, a source condition of the form

$$x^\dagger - x_0 \in \mathcal{R}(F'(x^\dagger)^*) \quad (4.33)$$

has to hold, which is not required for Nesterov's accelerated gradient method (4.4). Before we turn to our main result, we first prove a couple of important consequences of (4.23) and the stopping rule (4.30).

Proposition 4.1.10. *Let Assumption 4.1.1 be satisfied, let x_k^δ and z_k^δ be defined by (4.4) and let \mathcal{E}^δ be defined by (4.12). Assuming that the stopping index k_* is determined by (4.30) with some $\tau > 1$, then, for all $0 \leq k \leq k_*$, the sequence $(\mathcal{E}^\delta(k))$ is non-increasing and in particular, $\mathcal{E}^\delta(k) \leq \mathcal{E}^\delta(0)$. Furthermore, for all $0 \leq k \leq k_*$ there holds*

$$\Theta^\delta(x_k^\delta) - \Theta^\delta(x_*) \leq \frac{(\alpha - 1)\mathcal{E}^\delta(0)}{2\omega(k + \alpha - 2)^2}, \quad (4.34)$$

as well as

$$\|w_k^\delta - x_*\|^2 \leq \frac{\mathcal{E}^\delta(0)}{(\alpha - 1)}, \quad (4.35)$$

and

$$\sum_{k=1}^{k_*-1} \left(k (\Theta^\delta(x_k^\delta) - \Theta^\delta(x_*)) - \frac{(k + \alpha - 1)^2}{(\alpha - 3)} \Delta(\delta) \right) \leq \frac{(\alpha - 1)\mathcal{E}^\delta(1)}{2\omega(\alpha - 3)}. \quad (4.36)$$

Proof. Due to the definition of the stopping rule (4.30) and the arguments preceding it, the term (4.28) is positive for all $k \leq k_* - 1$. Hence, due to (4.23), $\mathcal{E}^\delta(k)$ is non-increasing for all $k \leq k_*$ and in particular, $\mathcal{E}^\delta(k) \leq \mathcal{E}^\delta(0)$. From this observation, (4.34) and (4.35) immediately follow from the definition (4.12) of $\mathcal{E}^\delta(k)$.

Furthermore, rearranging (4.23) we have

$$\frac{2\omega(\alpha-3)}{\alpha-1} \left(k(\Theta^\delta(x_k^\delta) - \Theta^\delta(x_*)) - \frac{(k+\alpha-1)^2}{(\alpha-3)}\Delta(\delta) \right) \leq \mathcal{E}^\delta(k) - \mathcal{E}^\delta(k+1).$$

Now, summing over this inequality and using telescoping and the fact that $\mathcal{E}^\delta(k_*) \geq 0$ we immediately arrive at (4.36), which concludes the proof. \square

From the above proposition, we are able to deduce two interesting corollaries.

Corollary 4.1.11. *Under the assumptions of Proposition 4.1.10 there holds*

$$\|F(x_k^\delta) - y^\delta\|^2 \leq \frac{2(\alpha-1)\mathcal{E}^\delta(0)}{\omega(k+\alpha-2)^2} + \delta^2, \quad 0 \leq k \leq k_*. \quad (4.37)$$

Proof. Using the fact that both $x_k^\delta, x_* \in \mathcal{B}_{2\rho}(x_0)$, it follows from the definition of Θ^δ that $\Theta^\delta(x_k^\delta) = \Phi^\delta(x_k^\delta)$ and $\Theta^\delta(x_*) = \Phi^\delta(x_*)$. Hence, inequality (4.34) yields

$$\|F(x_k^\delta) - y^\delta\|^2 \leq \frac{2(\alpha-1)\mathcal{E}^\delta(0)}{\omega(k+\alpha-2)^2} + \|y - y^\delta\|^2, \quad 0 \leq k \leq k_*,$$

from which, using $\|y - y^\delta\| \leq \delta$, the statement immediately follows. \square

Corollary 4.1.12. *Under the assumptions of Proposition 4.1.10 there holds*

$$k_*(k_* - 1) \leq \left(\frac{2(\alpha-1)\mathcal{E}^\delta(1)}{\omega(\alpha-3)(\tau^2-1)} \right) \frac{1}{\delta^2}.$$

Proof. Using the fact that both $x_k^\delta, x_* \in \mathcal{B}_{2\rho}(x_0)$, it follows from the definition of Θ^δ that $\Theta^\delta(x_k^\delta) = \Phi^\delta(x_k^\delta)$ and $\Theta^\delta(x_*) = \Phi^\delta(x_*)$. Hence, it follows with $\|y - y^\delta\| \leq \delta$ that

$$\begin{aligned} & k(\Theta^\delta(x_k^\delta) - \Theta^\delta(x_*)) - \frac{(k+\alpha-1)^2}{(\alpha-3)}\Delta(\delta) \\ & \geq \frac{k}{2} \left(\|F(x_k^\delta) - y^\delta\|^2 - \delta^2 \right) - \frac{(k+\alpha-1)^2}{(\alpha-3)}\Delta(\delta). \end{aligned}$$

Together with the definition of the stopping rule (4.30), this implies that for all $k \leq k_* - 1$

$$k(\Theta^\delta(x_k^\delta) - \Theta^\delta(x_*)) - \frac{(k+\alpha-1)^2}{(\alpha-3)}\Delta(\delta) > k \frac{(\tau^2-1)\delta^2}{2}$$

Using this in (4.36) yields

$$\frac{(\tau^2-1)\delta^2}{2} \sum_{k=1}^{k_*-1} k \leq \frac{(\alpha-1)\mathcal{E}^\delta(1)}{2\omega(\alpha-3)},$$

from which the statement now immediately follows. \square

Again, this shows that $k_* = \mathcal{O}(\delta^{-1})$, i.e., $k_* \leq c\delta^{-1}$, however this time the constant c does not depend on c_1 and c_2 , an observation which we use when analysing (4.4) under slightly different assumptions than Assumption 4.1.1 below.

We are now able to prove one of our main results:

Theorem 4.1.13. *Let Assumption 4.1.1 hold and let the iterates x_k^δ and z_k^δ be defined by (4.4). Furthermore, let $k_* = k_*(\delta, y^\delta)$ be determined by (4.30) with some $\tau > 1$ and let the solution set \mathcal{S} be given by (4.9). Then there exists an $\tilde{x} \in \mathcal{S}$ and a subsequence $\tilde{x}_{k_*}^\delta$ of $x_{k_*}^\delta$ which converges weakly to \tilde{x} as $\delta \rightarrow 0$, i.e.,*

$$\lim_{\delta \rightarrow 0} \langle \tilde{x}_{k_*}^\delta, h \rangle = \langle \tilde{x}, h \rangle, \quad \forall h \in \mathcal{X}.$$

If \mathcal{S} is a singleton, then $x_{k_*}^\delta$ converges weakly to the then unique solution $\tilde{x} \in \mathcal{S}$.

Proof. This proof follows some ideas of [32]. Let $y_n := y^{\delta_n}$ be a sequence of noisy data satisfying $\|y - y_n\| \leq \delta_n$. Furthermore, let $k_n := k_*(\delta_n, y_n)$ be the stopping index determined by (4.30) applied to the pair (δ_n, y_n) . There are two cases. First, assume that k is a finite accumulation point of k_n . Without loss of generality, we can assume that $k_n = k$ for all $n \in \mathbb{N}$. Thus, from (4.30), it follows that

$$\|F(x_k^{\delta_n}) - y_n\| < \frac{2(k + \alpha - 1)^2}{k(\alpha - 3)} \Delta(\delta_n) + \tau^2 \delta_n^2,$$

which, together with the triangle inequality, implies

$$\|F(x_k^{\delta_n}) - y\| \leq \|F(x_k^{\delta_n}) - y_n\| + \|y_n - y\| \leq \frac{2(k + \alpha - 1)^2}{k(\alpha - 3)} \Delta(\delta_n) + \tau^2 \delta_n^2 + \delta_n.$$

Since for fixed k the iterates x_k^δ depend continuously on the data y^δ , by taking the limit $n \rightarrow \infty$ in the above inequality we can derive

$$x_k^{\delta_n} \rightarrow x_k^0, \quad F(x_k^{\delta_n}) \rightarrow F(x_k^0) = y, \quad \text{as } n \rightarrow \infty.$$

For the second case, assume that $k_n \rightarrow \infty$ as $n \rightarrow \infty$. Since $x_{k_n}^{\delta_n} \in \mathcal{B}_{2\rho}(x_0)$, it is bounded and hence, has a weakly convergent subsequence $x_{\tilde{k}_n}^{\tilde{\delta}_n}$, corresponding to a subsequence $\tilde{\delta}_n$ of δ_n and $\tilde{k}_n := k_*(\tilde{\delta}_n, y^{\tilde{\delta}_n})$. Denoting the weak limit of $x_{\tilde{k}_n}^{\tilde{\delta}_n}$ by \tilde{x} , it remains to show that $\tilde{x} \in \mathcal{S}$. For this, observe that it follows from (4.37) that

$$\left\| F(x_{\tilde{k}_n}^{\tilde{\delta}_n}) - y^\delta \right\|^2 \leq \frac{2(\alpha - 1)\mathcal{E}^{\tilde{\delta}_n}(0)}{\omega(\tilde{k}_n + \alpha - 2)^2} + \tilde{\delta}_n^2 \rightarrow 0, \quad \text{as } n \rightarrow \infty.$$

where we have used that $\tilde{k}_n \rightarrow \infty$ and $\tilde{\delta}_n \rightarrow 0$ as $n \rightarrow \infty$, which follows from the assumption that so do the sequences k_n and δ_n , and the fact that $\mathcal{E}^\delta(0)$ stays bounded for $\delta \rightarrow 0$. Hence, since we know that $y^\delta \rightarrow y$ as $\delta \rightarrow 0$, we can deduce that

$$F\left(x_{\tilde{k}_n}^{\tilde{\delta}_n}\right) \rightarrow y, \quad \text{as } n \rightarrow \infty,$$

and therefore, using the weak sequential closedness of F on $\mathcal{B}_{2\rho}(x_0)$, we deduce that $F(\tilde{x}) = y$, i.e., $\tilde{x} \in \mathcal{S}$, which was what we wanted to show.

It remains to show that if \mathcal{S} is a singleton then $x_{k_*}^\delta$ converges weakly to \tilde{x} . Since this was already proven above in the case that k_n has a finite accumulation point, it remains to consider the second case, i.e., $k_n \rightarrow \infty$. For this, consider an arbitrary subsequence of $x_{k_*}^\delta$. Since this sequence is bounded, it has a weakly convergent subsequence which, by the same arguments as above, converges to a solution $\tilde{x} \in \mathcal{S}$. However, since we have assumed that \mathcal{S} is a singleton, it follows that $x_{k_*}^\delta$ converges weakly to \tilde{x} , which concludes the proof. \square

Remark. In Theorem 4.1.13, we have shown weak subsequential convergence to an element \tilde{x} in the solution set \mathcal{S} . However, this element might be different from the x_0 -minimum norm solution x^\dagger defined by (4.10), unless of course in case that \mathcal{S} is a singleton.

4.2 Convergence Analysis III

Some simplifications of the above presented convergence analysis are possible if we assume that instead of only Φ^0 , all the functionals Φ^δ are convex. Hence, for the remainder of this section, we work with the following

Assumption 4.2.1. Let ρ be a positive number such that $\mathcal{B}_{6\rho}(x_0) \subset \mathcal{D}(F)$.

1. The operator $F : \mathcal{D}(F) \subset \mathcal{X} \rightarrow \mathcal{Y}$ is continuously Fréchet differentiable between the real Hilbert spaces \mathcal{X} and \mathcal{Y} with inner products $\langle \cdot, \cdot \rangle$ and norms $\|\cdot\|$. Furthermore, let F be weakly sequentially closed on $\mathcal{B}_{2\rho}(x_0)$.
2. The equation $F(x) = y$ has a solution $x_* \in \mathcal{B}_\rho(x_0)$.
3. The data y^δ satisfies $\|y - y^\delta\| \leq \delta$.
4. The functionals Φ^δ are convex and have Lipschitz continuous gradients $\nabla\Phi^\delta$ with uniform Lipschitz constant L on $\mathcal{B}_{6\rho}(x_0)$, i.e.,

$$\Phi^\delta(\lambda x_1 + (1 - \lambda)x_2) \leq \lambda\Phi^\delta(x_1) + (1 - \lambda)\Phi^\delta(x_2), \quad \forall x_1, x_2 \in \mathcal{B}_{6\rho}(x_0), \quad (4.38)$$

$$\|\nabla\Phi^\delta(x_1) - \nabla\Phi^\delta(x_2)\| \leq L \|x_1 - x_2\|, \quad \forall x_1, x_2 \in \mathcal{B}_{6\rho}(x_0).$$

5. For α in (4.4) there holds $\alpha > 3$ and the scaling parameter ω satisfies $0 < \omega < \frac{1}{L}$.

Note that Assumption 4.2.1 is only a special case of Assumption 4.1.1. Hence, the above convergence analysis presented above is applicable and we get weak convergence of the iterates of (4.4). However, the stopping rule (4.30) depends on the constants c_1 and c_2 defined by (4.19), which are not always available in practise. Fortunately, using the Assumption 4.2.1, we can get rid of c_1 and c_2 . The key idea is to observe that the following lemma holds:

Lemma 4.2.1. *Under Assumption 4.2.1, for all $x, z \in \mathcal{B}_{6\rho}(x_0)$ there holds*

$$\Theta^\delta(z - \omega G_\omega^\delta(z)) \leq \Theta^\delta(x) + \langle G_\omega^\delta(z), z - x \rangle - \frac{\omega}{2} \|G_\omega^\delta(z)\|^2.$$

Proof. This follows from the convexity of Θ^δ in the same way as in Lemma 4.1.2. \square

From the above lemma, it follows that the results of Corollary 4.1.5 and Proposition 4.1.6 hold with $\Delta(\delta) = 0$. Therefore, the stopping rule (4.30) simplifies to

$$\|F(x_{k_*}^\delta) - y^\delta\| \leq \tau\delta < \|F(x_k^\delta) - y^\delta\|, \quad k_* \geq k, \quad (4.39)$$

for some $\tau > 1$, which is nothing else than the discrepancy principle (2.6). Note that in contrast to (4.30), only the noise level δ needs to be known in order to determine the stopping index k_* . With the same arguments as above, we are now able to prove our second main result:

Theorem 4.2.2. *Let Assumption 4.2.1 hold and let the iterates x_k^δ and z_k^δ be defined by (4.4). Furthermore, let $k_* = k_*(\delta, y^\delta)$ be determined by (4.39) with some $\tau > 1$ and let the solution set \mathcal{S} be given by (4.9). Then for the stopping index k_* there holds $k_* = \mathcal{O}(\delta^{-1})$. Furthermore, there exists an $\tilde{x} \in \mathcal{S}$ and a subsequence $\tilde{x}_{k_*}^\delta$ of $x_{k_*}^\delta$ which converges weakly to \tilde{x} as $\delta \rightarrow 0$, i.e.,*

$$\lim_{\delta \rightarrow 0} \langle \tilde{x}_{k_*}^\delta, h \rangle = \langle \tilde{x}, h \rangle, \quad \forall h \in \mathcal{X}.$$

If \mathcal{S} is a singleton, then $x_{k_}^\delta$ converges weakly to the then unique solution $\tilde{x} \in \mathcal{S}$.*

Proof. The proof of this theorem is analogous to the proof of Theorem 4.1.13. The only main difference is the well definedness of k_* , which now cannot be derived from Lemma 4.1.9 but follows from (4.36) by Corollary 4.1.12, which also yields $k_* = \mathcal{O}(\delta^{-1})$. \square

Remark. Note that since Theorem 4.2.2 only gives an asymptotic result, i.e., for $\delta \rightarrow 0$, the requirement in Assumption 4.2.1 that the functionals Φ^δ have to be convex for all $\delta > 0$ can be relaxed to $0 \leq \delta \leq \bar{\delta}$, as long as we only consider data y^δ satisfying the noise constraint $\|y - y^\delta\| \leq \delta \leq \bar{\delta}$.

Remark. Note that if the functionals Φ^δ are globally convex and uniformly Lipschitz continuous, which is for example the case if F is a bounded linear operator, then one can choose ρ arbitrarily large in the definition of Ψ . Now, as we have seen above, the proximal mapping $\text{prox}_{\omega\Psi}(\cdot)$ is nothing else than the projection onto $\mathcal{B}_{2\rho}(x_0)$. This implies that for practical purposes, $\text{prox}_{\omega\Psi}(\cdot)$ may be dropped in (4.4), which means that one effectively uses (2.22) instead of (4.4).

4.3 Strong Convexity and Nonlinearity Conditions

In this section, we consider the question of strong convergence of the iterates of (4.4) and comment on the connection between the assumption of local convexity and the (weak) tangential cone condition.

Concerning the strong convergence of the iterates of (4.4) and (2.22), note that it could be achieved if the functional Φ^0 were locally strongly convex, i.e., if

$$\langle F'(x_1)^*(F(x_1) - y) - F'(x_2)^*(F(x_2) - y), x_1 - x_2 \rangle \geq \alpha \|x_1 - x_2\|^2, \quad (4.40)$$

$$\forall x_1, x_2 \in \mathcal{B}_{2\rho}(x_0),$$

since then, for the choice of $x_1 = x_k^0$ and $x_2 = x_*$, one gets

$$\alpha \|x_k^0 - x_*\| \leq \langle F'(x_k^0)^*(F(x_k^0) - y), x_k^0 - x_* \rangle \leq 2\bar{\omega}\rho \|F(x_k^0) - y\|,$$

from which, since we have $\|F(x_k^0) - y\| \rightarrow 0$ as $\delta \rightarrow 0$, it follows that x_k^0 converges strongly to x_* as $\delta \rightarrow 0$. Hence, retracing the proof of Theorem 4.1.13, one would get

$$\lim_{\delta \rightarrow 0} x_{k_*}^\delta = x_*.$$

Unfortunately, already for linear ill-posed operators $F = A$, strong convexity of the form (4.40) cannot be satisfied, since then one would get

$$\|Ax_1 - Ax_2\| \geq \alpha \|x_1 - x_2\|, \quad \forall x_1, x_2 \in \mathcal{B}_{2\rho}(x_0),$$

which already implies the well-posedness of $Ax = y$ in $\mathcal{B}_{2\rho}(x_0)$. However, defining

$$\mathcal{M}_\tau(A) := \{x \in \mathcal{B}_{2\rho} \mid \exists w \in \mathcal{Y}, \|w\| \leq \tau, x - x^\dagger = A^*w\}, \quad (4.41)$$

it was shown in [36, Lemma 3.3] that there holds

$$\|x - x^\dagger\|^2 \leq \tau \|Ax - Ax^\dagger\|, \quad \forall x \in \mathcal{M}_\tau(A),$$

Hence, if one could show that $x_k^0 \in \mathcal{M}_\tau$ for some $\tau > 0$ and all $k \in \mathbb{N}$, then it would follow that

$$\|x_k^0 - x^\dagger\|^2 \leq \tau \|Ax_k^0 - y\|, \quad \forall x \in \mathcal{M}_\tau(A),$$

from which strong convergence of x_k^0 , and consequently also of $x_{k_*}^\delta$ to x^\dagger would follow. In essence, this was done in [61] with tools from spectral theory in the classical framework for analysing linear ill-posed problem [21] under the source condition $x^\dagger \in \mathcal{R}(A^*)$.

Remark. Note that it is sometimes possible, given weak convergence of a sequence $x_k \in \mathcal{X}$ to some element $\tilde{x} \in \mathcal{X}$, to infer strong convergence of x_k to \tilde{x} in a weaker topology. For example, if $x_k \in H^1(\Omega)$ converges weakly to \tilde{x} in the $H^1(\Omega)$ norm, then it follows that x_k converges strongly to \tilde{x} with respect to the $L^2(\Omega)$ norm. Many generalizations of this example are possible. Note further that in finite dimensions, weak and strong convergence coincide.

In the remaining part of this section, we want to comment on the connection of the local convexity assumption (4.5) to other nonlinearity conditions like (3.1) and (2.10) commonly used in the analysis of nonlinear inverse problems.

First of all, note that due to the results of Kindermann [47], we know that both convexity and the (weak) tangential cone condition imply weak convergence of Landweber iteration (2.4). However, it is not entirely clear in which way those conditions are connected.

One connection of the two conditions was given in [71], where it was shown that the nonlinearity condition implies a certain directional convexity condition. Another connection was provided in [47], where it was shown that the tangential cone condition implies a quasi-convexity condition. However, it is not clear whether or not the tangential cone condition implies convexity or not. What we can say is that convexity does not imply the (weak) tangential cone condition, which is shown in the following

Example 4.3.1. Consider the operator $F : H^1[0, 1] \rightarrow L^2[0, 1]$ defined by

$$F(x)(s) := \int_0^s x(t)^2 dt. \quad (4.42)$$

This nonlinear Hammerstein operator was extensively treated as an example problem for nonlinear inverse problems (see for example [32, 59]). It is well known that for this operator the tangential cone condition is satisfied around x^\dagger as long as $x^\dagger \geq c > 0$. However, the (weak) tangential cone condition is not satisfied in case that $x^\dagger \equiv 0$. Moreover, it can easily be seen (for example from (4.43)) that $\Phi^0(x)$ is globally convex, which shows that convexity does not imply the tangential cone condition.

Remark. Note that if F is twice continuously Fréchet differentiable, then convexity of Φ^δ is equivalent to positive semi-definiteness of its second Fréchet derivative [69]. More precisely, we have that (4.38) is equivalent to

$$\|F'(x)h\|^2 + \langle F(x) - y^\delta, F''(x)(h, h) \rangle \geq 0, \quad \forall x \in \mathcal{B}_{6\rho}(x_0), \forall h \in \mathcal{D}(F), \quad (4.43)$$

which we use to prove local convexity for some of the examples considered in Part II.

Part II

Application of TPG Methods

Chapter 5

Application and Comparison of General TPG Methods

In this chapter, we consider the application and comparison of general TPG methods of the form (2.23) based on various stepsizes α_k^δ and combination parameters λ_k^δ . We apply the methods to two problems involving a nonlinear Hammerstein operator and the medical imaging technique of Single Photon Emission Computed Tomography (SPECT), respectively. Numerical examples demonstrate the various acceleration effects of different TPG methods compared to classical Landweber iteration (2.4).

5.1 Nonlinear Hammerstein Operator

As the first example, we consider the nonlinear Hammerstein integral operator

$$F : H^1[0, 1] \rightarrow L^2[0, 1], \quad F(x)(s) := \int_0^s (x(t))^3 dt, \quad (5.1)$$

which is often used in the literature (see for example [32, 58–60]) to illustrate convergence conditions, demonstrate convergence rates and show the effects of different stepsizes and acceleration techniques. Importantly, the operator F is Fréchet differentiable and furthermore, if $x(t) \geq \kappa > 0$ for all $x \in \mathcal{B}_{4\rho}(x_0)$ and $t \in [0, 1]$, then one can show that there exists a family of bounded linear operators $R_x(\tilde{x}) : \mathcal{Y} \rightarrow \mathcal{Y}$ and a constant $c > 0$ such that

$$F'(x) = R_x(\tilde{x})F'(\tilde{x}), \quad \|R_x(\tilde{x}) - I\| \leq c \|x - \tilde{x}\|, \quad (5.2)$$

for all $x, \tilde{x} \in \mathcal{B}_{4\rho}(x_0) \subset \mathcal{D}(F)$, which in particular implies that

$$\|F(x) - F(\tilde{x}) - F'(\tilde{x})(x - \tilde{x})\| \leq \frac{c}{2 - c\|x - \tilde{x}\|} \|x - \tilde{x}\| \|F(x) - F(\tilde{x})\|. \quad (5.3)$$

Hence, if $x^\dagger \in \mathcal{B}_\rho(x_0)$ satisfies $x^\dagger \geq \bar{\kappa} > 0$ and if $\rho > 0$ is small enough such that both $x \geq \kappa > 0$ for all $x \in \mathcal{B}_{6\rho}(x_0)$ and $6c\rho < 1$ are satisfied, then the nonlinearity condition

(3.1) holds with

$$\eta = \frac{2c\rho}{1 - 2c\rho} < \frac{1}{2}. \quad (5.4)$$

Hence, since for this problem the operators $R_x(\tilde{x})$ can be given explicitly by (see [32])

$$R_x(\tilde{x})^* w = - \left(\frac{\phi'(x)}{\phi'(\tilde{x})} \int_0^1 w(t) dt \right)', \quad (5.5)$$

it is possible to determine an η from (5.4) by deriving an estimate of the constant c in (5.2). Since explicit estimates of this constant are usually not sharp enough, one often tries to numerically compute an estimate for c . However, since we do not require c but only η for our tests, we numerically estimate η directly from (3.1).

For our tests we use the same setup as in [60], i.e., we assume that $y = F(x^\dagger)$ with

$$x^\dagger(t) := 1 + 10^{-2}(7 - 3t^2 + 2t^3), \quad (5.6)$$

and that $x_0(t) = 1$. Hence, we have that

$$x^\dagger - x_0 \in \mathcal{R}(F'(x^\dagger)^*) \quad \text{and} \quad \rho = \|x^\dagger - x_0\| = \frac{1}{100} \sqrt{\frac{305}{7}} \approx 0.066. \quad (5.7)$$

Numerical calculations show that the constant c in (5.2) is given by $c \approx 3$, which, by (5.4) would imply that $\eta \approx 0.656 > \frac{1}{2}$. However, numerically estimating η directly via (3.1) shows that η is actually much smaller, i.e., $\eta \approx 0.4$. Moreover, when using classical Landweber iteration, with or without the steepest descent or the minimal error stepsize, condition (3.1) only has to hold on $\mathcal{B}_{2\rho}(x_0)$ (see [46]). Estimating η on this set gives $\eta \approx 0.2$, the choice of which leads to strongly improved results also for our TPG methods. Hence, we use $\eta = 0.2$ in all of the numerical tests below.

In order to discretize the problem, we subdivide the interval $[0, 1]$ into $n = 128$ equally spaced subintervals and replace the operators F , $F'(x)$ and $F'(x)^*$ by finite dimensional approximations defined in the same way as in [58, 60]. The data was created on a finer grid and a random relative data error of 0.001% was added to get y^δ .

The implementation of the problem was done in MATLAB on a stationary computer with a Xeon W3680 CPU (6 cores, 3.33GHz, 12MB cache) and 24GB RAM (6x4GB DDR3, 1333 MHz). This is also the case for all other numerical results in this thesis.

We now want to compare the TPG methods (2.23) based on a constant stepsize ω , the steepest descent stepsize α_k^{SD} and the minimal error stepsize α_k^{ME} , which we introduced in Section 3.2, with their classical, non-accelerated counterparts. For choosing λ_k^δ , we use the Nesterov combination parameter (compare with (4.1)),

$$\lambda_k^N := \frac{k-1}{k+\alpha-1}, \quad (5.8)$$

where we only consider the standard choice $\alpha = 3$, the sequence of λ_k^δ defined by the DBTS algorithm 3.2.2, which we denote by λ_k^B , as well as the sequences given explicitly by (3.20) and (3.86), which are equivalent, since we use $\omega = 1/\bar{\omega}^2$, and which we denote by λ_k^E .

For using the DBTS algorithm, but also for choosing a suitable τ in the discrepancy principle, the approximation for η described above was used. From this, Ψ was calculated by (3.8) and τ was chosen by

$$\tau = 2\tilde{\tau} \frac{1 + \eta}{1 - 2\eta}, \quad (5.9)$$

where $\tilde{\tau} = 1.01$, which ensures that condition (3.14) is satisfied. In the backtracking algorithm for λ_k^B , we use $j_{\max} = 5$ and $\mu = 2$. For the function $q : \mathbb{R}_0^+ \rightarrow \mathbb{R}_0^+$, we use $q(m) = 1/m^{1.1}$, which obviously satisfies the necessary condition (3.93). When using a constant stepsize, we have use the scaling parameter $\omega = 0.3175$, which is chosen by numerically estimating the constant $\bar{\omega}$ in (3.70) and then taking $\omega = 1/\bar{\omega}^2$.

Stepsize	$\lambda_k^\delta = 0$	$\lambda_k^\delta = \lambda_k^E$	$\lambda_k^\delta = \lambda_k^B$	$\lambda_k^\delta = \lambda_k^N$	k_*	Time
Steepest Descent	x				125	79 s
Steepest Descent		x			35	22 s
Steepest Descent			x		41	26 s
Steepest Descent				x	14	9 s
Minimal Error	x				7	4 s
Minimal Error		x			183	116 s
Minimal Error			x		192	135 s
Minimal Error				x	78	45 s
Constant, $\omega = 0.3175$	x				260	178 s
Constant, $\omega = 0.3175$		x			42	29 s
Constant, $\omega = 0.3175$			x		48	33 s
Constant, $\omega = 0.3175$				x	32	22 s

Table 5.1: Comparison of different stepsizes α_k^δ and combination parameters λ_k^δ : Number of iterations k_* and total amount of time necessary to satisfy the discrepancy principle. A relative data error of 0.001% was used.

A summary of the results can be found in Table 5.1. For both the constant and the steepest descent stepsize all three non-zero combination parameters λ_k^δ lead to a considerable decrease in the required number of iterations and computation time to meet the stopping rule. The choices $\lambda_k^\delta = \lambda_k^E$ and $\lambda_k^\delta = \lambda_k^B$ seem to perform equally well, with the explicit choice $\lambda_k^\delta = \lambda_k^E$ requiring slightly less time and iterations in both cases. Furthermore, using the combination parameter $\lambda_k^\delta = \lambda_k^N$ requires the least amount of time and iterations, the necessary time being more than halved in the case

of the steepest descent stepsize. For the minimal error stepsize, the choice $\lambda_k^\delta = \lambda_k^N$ is again the best of all three non-zero combination parameters $\lambda_k^\delta = 0$. However, using $\lambda_k^\delta = 0$, i.e., the pure minimal error method without acceleration, only 7 iterations are required, making it the best reconstruction method for this example. This fact was already observed in [60], where regardless of the discretization and the noise level, a constant number of iterations was required to meet the stopping rule. No explanation for this could be given in [60] for this pathological case and here we only state that in the numerical example treated in the next section, the choice $\lambda_k^\delta = \lambda_k^N$ requires significantly less iterations than the choice $\lambda_k^\delta = 0$ also for the minimal error stepsize.

5.2 Single Photon Emission Computed Tomography

In the second example, we take a look at the medical imaging technique of SPECT, where one aims at reconstructing a radioactive distribution f , termed *activity function*, from radiation measurements outside the body, denoted by y . The usual modelling approach connects f and y by the *attenuated Radon transform* (ATRT), see for example [56], which is given by

$$y = A(f, \mu)(s, \omega) := \int_{\mathbb{R}} f(s\omega^\perp + t\omega) \exp\left(-\int_t^\infty \mu(s\omega^\perp + r\omega) dr\right) dt, \quad (5.10)$$

where $s \in \mathbb{R}$, $\omega \in S^1$. The function μ is called an *attenuation map* and is related to the density of different tissues. If μ is known, then reconstructing f from y is a linear problem. However, unless an additional CT (computerized tomography) scan is performed, which is not preferable due to the increased cost of the medical examination, μ is unknown as well. Hence, we face the nonlinear inverse problem of reconstructing the pair (f, μ) from y , or rather, from a noisy version y^δ of y .

This inverse problem and its numerical treatment, under various additional conditions like sparsity, has already been extensively studied (see for example [15, 16, 63, 67] and the references therein). Considering the definition space of the ATRT operator, it was shown in [15], that if

$$\mathcal{D}(A) := H_0^{s_1}(\Omega) \times H_0^{s_2}(\Omega), \quad (5.11)$$

where $H_0^s(\Omega)$ is the classical Sobolev space of order s over the bounded domain Ω with zero boundary conditions, then, assuming that s_1 and s_2 are chosen large enough, the operator A is twice continuously Fréchet differentiable with a Lipschitz continuous first derivative. Since one expects some discontinuities in (f, μ) , one wants to choose s_1 and s_2 as small as possible. In [15] it was shown that it is possible to use $s_1 > 4/9$ and $s_2 = 1/3$, a choice which also allows a certain amount of non-smoothness of (f, μ) .

For our numerical simulations, we used the so-called MCAT-phantom [42], which is depicted in Figure 5.1. As one can see, the simulated activity function f_* is concentrated in the heart and the attenuation function μ_* models a cut through the thorax. Both functions are given as 80×80 pixel images. The Radon transform, its Fréchet derivative and the adjoint thereof were discretized to work on those pixel images, using 79 angles ω , equally distributed over 360 degrees, and 80 samples for s .

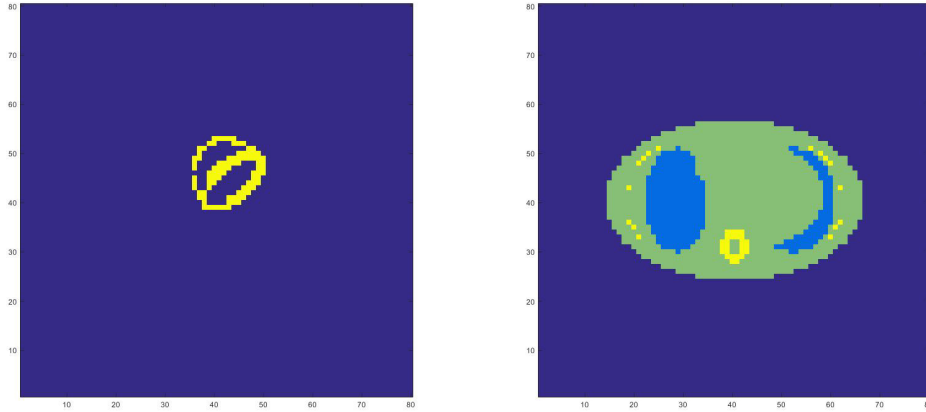


Figure 5.1: Activity function f_* (left) and attenuation function μ_* (right).

The data y was calculated by $y = A(f_*, \mu_*)$, i.e., by applying the discretized version of the attenuated Radon transform to the pair (f_*, μ_*) . The resulting sinogram is depicted in Figure 5.2, once for the already shown attenuation function μ_* and once for $\mu_* = 0$. Afterwards, random data error was added in order to arrive at y^δ .

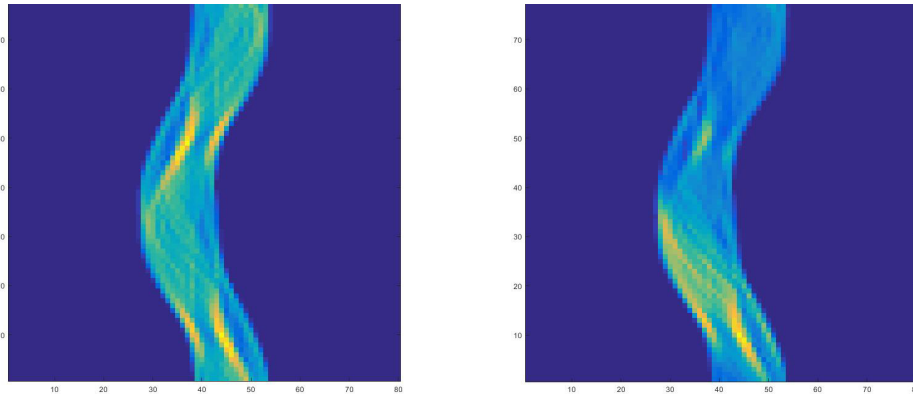


Figure 5.2: The generated data $y = A(f_*, 0)$ (left) and $y = A(f_*, \mu_*)$ (right).

As in the previous section, we now want to compare the TPG methods (2.23) based on a constant stepsize ω , the steepest descent stepsize α_k^{SD} and the minimal error stepsize α_k^{ME} with their classical, non-accelerated counterparts. Again we use the notation λ_k^E , λ_k^B and λ_k^N to distinguish between the different combination parameters λ_k^δ .

Concerning the nonlinearity constant η , it is not clear whether a condition like (3.1) holds for SPECT. Unfortunately, this is the case for almost all nonlinear inverse problems of practical importance. However, a value for η is needed both in the DBTS algorithm and for calculating Ψ and τ . Hence, we used the conservative estimate of $\eta = 0.4$ for obtaining the presented results. From this, Ψ was calculated by (3.8) and τ was chosen by

$$\tau = 2\tilde{\tau} \frac{1 + \eta}{1 - 2\eta}, \quad (5.12)$$

where this time $\tilde{\tau} = 4$ was chosen. The resulting $\tau = 56$ might seem rather large but numerical tests show that decreasing τ for example to the canonical choice $\tau = 2$ leads to numerical instabilities which make it impossible for any of the methods to decrease the residual to the level of $\tau\delta$. Hence, the choice of τ as stated above seems to be at least of optimal order. Furthermore, as noted in the last paragraph of Section 3.2, τ should not be chosen too small since otherwise Ψ would become undesirably small. Concerning the remaining parameters, they were all chosen as in the previous section, with the obvious exception of ω , for which the value $\omega = 4.7 \cdot 10^{-4}$ was found by numerical calculations.

We now compare the effects of combining different choices of λ_k^δ with different stepsizes α_k^δ . For this test, the results of which are presented in Table 5.2, we used a relative data error of 0.25%¹. Note first that independently of the chosen stepsize α_k^δ , using $\lambda_k^\delta = \lambda_k^N$ leads to the smallest number of iterations necessary before meeting the stopping rule, with only about one tenth of iterations and computation time required! For $\lambda_k^\delta = \lambda_k^B$ defined by the DBTS algorithm, we can see that for the constant stepsize $\omega = 10^{-5}$ and the steepest descent stepsize α_k^{SD} , although requiring more iterations and computation time, the overall effort is still significantly lower than when not using any acceleration. The bad behaviour of the combination of λ_k^B with the minimal error stepsize α_k^{ME} can best be explained by the fact that using the minimal error stepsize, the residuals are not decreasing monotonously and hence, the DBTS algorithm has difficulties finding a suitable parameter λ_k^B . As for the choice $\lambda_k^\delta = \lambda_k^E$, one can see that in combination with the steepest descent stepsize α_k^{SD} , about three times as many iterations are required than when using $\lambda_k^\delta = \lambda_k^N$. However, still much less iterations are required than when using no acceleration at all. A similar phenomenon can also be observed for the constant stepsize ω , where the choice $\lambda_k^\delta = \lambda_k^E$ can even compete with the choice $\lambda_k^\delta = \lambda_k^B$, needing only slightly more iterations but significantly less computation time. As was also the case for the choice $\lambda_k^\delta = \lambda_k^B$, the choice $\lambda_k^\delta = \lambda_k^E$ behaves badly in combination with the minimal error stepsize α_k^{ME} . Again the most likely reason is the non-monotone nature of this stepsize choice.

Since the acceleration effect is due to λ_k^δ , it makes sense to look at its evolution over the course of the iteration. The left sub-figure in Figure 5.3 depicts the development of

¹This is a very optimistic estimate for SPECT, since in practice one would expect the relative data error to be upwards of 5%. However, for such a high amount of noise, only a couple of iterations are required to satisfy the stopping criterion (3.13) even for Landweber iteration and hence, no acceleration effect would be observable.

Stepsize	$\lambda_k^\delta = 0$	$\lambda_k^\delta = \lambda_k^E$	$\lambda_k^\delta = \lambda_k^B$	$\lambda_k^\delta = \lambda_k^N$	k_*	Time
Steepest Descent	x				3433	489 s
Steepest Descent		x			631	90 s
Steepest Descent			x		345	77 s
Steepest Descent				x	205	30 s
Minimal Error	x				2021	185 s
Minimal Error		x			6665	603 s
Minimal Error			x		6253	600 s
Minimal Error				x	288	28 s
Constant, $\omega = 4.7 \cdot 10^{-4}$	x				2019	186 s
Constant, $\omega = 4.7 \cdot 10^{-4}$		x			474	46 s
Constant, $\omega = 4.7 \cdot 10^{-4}$			x		467	57 s
Constant, $\omega = 4.7 \cdot 10^{-4}$				x	265	26 s

Table 5.2: Comparison of different stepsizes α_k^δ and combination parameters λ_k^δ : Number of iterations k_* and total amount of time necessary to satisfy the discrepancy principle. A relative data error of 0.25% was used.

λ_k^E , λ_k^B and λ_k^N when used in the TPG method with steepest descent stepsize α_k^{SD} for the SPECT problem considered above. One can see that in all three cases λ_k^δ goes to 1 as the iteration progresses, which is the reason for the acceleration effect. Although seemingly going to 1 with growing k , λ_k^B stays 0 for some of the first iterations and then exhibits a steep jump followed by some small oscillations, before starting to increase monotonously. This can be explained by the backtracking search procedure of the DBTS algorithm, which first has to go through some unsuccessful search cycles before the function $q(m)$ has decreased to the right order of magnitude. Afterwards, a monotonous increase also of λ_k^B can be seen. A similar phenomenon can also be observed when the DBTS algorithm is applied to the TPG method with constant stepsize ω . In the first iterations, λ_k^B is zero, then switches between 0 and 1 before it changes to monotonous increase starting from some value in $[0, 1]$, after which it again drops to some value in $[0, 1]$ and stars yet again to increase monotonously. In combination with the minimal error stepsize, λ_k^B first exhibits the same pattern as with the steepest descent stepsize α_k^{SD} but, after a certain amount of increase, starts to decrease monotonously, which explains why the acceleration effect is lost.

Note that if the function q is chosen such that it decreases too fast, then λ_k^B becomes a decreasing sequence. For example, the function $q(m) = 1/2^m$ often led to a decreasing sequence λ_k^B in our experiments. Hence, in order to profit from an acceleration effect, one has to choose a slowly decreasing function satisfying (3.93), like $q(m) = 1/m^{1+\alpha}$ with a small $\alpha > 0$. Similar restrictions can also be observed for second order methods like the Levenberg-Marquardt or the iteratively regularized Gauss-Newton method.

The right figure in Figure 5.3 depicts the development of the norm of the residuals

during the iterations of the TPG methods using the steepest descent stepsize α_k^{SD} together with the different choices of λ_k^δ considered above. Once again, one can clearly see the acceleration effect due to the three considered parameters λ_k^E , λ_k^B and λ_k^N , which manage to decrease the residual norm much faster than in the case when no acceleration, i.e., $\lambda_k^\delta = 0$, is being used.

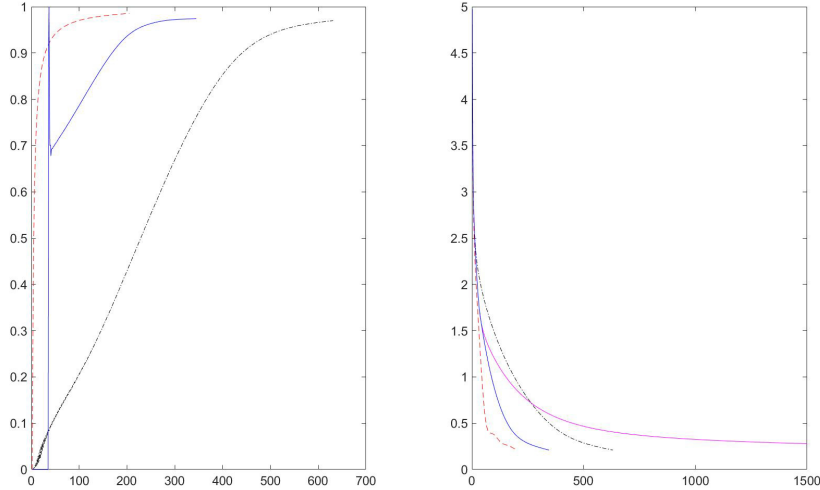


Figure 5.3: Results of using the TPG methods with steepest descent stepsize α_k^{SD} and various choices of λ_k^δ , using a relative data error of 0.25%. Left: Plot of the values of λ_k over the iteration number k . Right: Plot of the residual $\|A(f_k, \mu_k) - y^\delta\|$ over the iteration number k . Dashed red line: $\lambda_k^\delta = \lambda_k^N$, solid blue line: $\lambda_k^\delta = \lambda_k^B$, dash-dotted black line: $\lambda_k^\delta = \lambda_k^E$, solid magenta line in the right sub-figure (extending up to the y-axis value 1500): $\lambda_k^\delta = 0$.

Note that the residual norms decrease monotonously, which is also the case for the other stepsizes, except for the case when the minimal error stepsize α_k^{ME} is used in combination with either $\lambda_k^\delta = \lambda_k^E$ or $\lambda_k^\delta = 0$, in which case oscillations occur.

In Figure 5.4, one can see the results of the reconstruction of the activity and the attenuation function achieved when using the TPG method with steepest descent stepsize α_k^{SD} combined with λ_k^B for the choices of parameters as above and with a relative data error $\delta = 0.25\%$. One can see that the activity function f_* is nicely reconstructed. The attenuation function, however, does not resemble the true attenuation function μ_* at all. This phenomenon is common for SPECT and has already been observed in [67]. The reason for this is the high nonlinearity of the problem, leading to non-uniqueness of the solution and therefore, since the reconstruction algorithm selects a solution with minimal distance to $(f_0, \mu_0) = (0, 0)$, to the reconstruction of μ_* as seen in Figure 5.4. Possible remedies already mentioned in [67] are for example a better initial guess or a coupled tomography approach. In any case, the main reason for including μ in the reconstruction is to arrive at reconstructions conforming to the data. Besides, this chapter does not aim at improving the reconstruction quality of SPECT, but at showing the acceleration effect of TPG methods of the form (2.23).

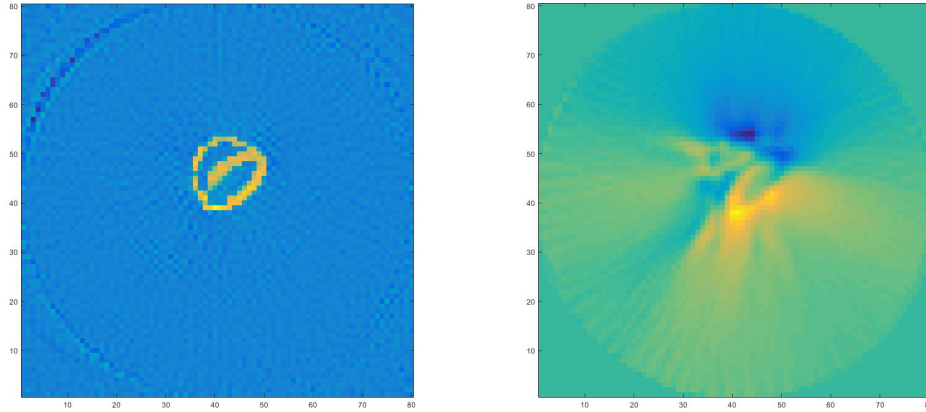


Figure 5.4: Results of the TPG method using the steepest descent stepsize α_k^{SD} together with $\lambda_k^\delta = \lambda_k^B$ for the SPECT example problem with a relative data error of $\delta = 0.25\%$. Activity function f_{k_*} (left) and attenuation function μ_{k_*} (right).

Repeating the comparison of different combinations of α_k^δ and λ_k^δ , with the same parameters as before but now using a slightly smaller relative data error $\delta = 0.2\%$, leads to the results presented in Table 5.3. Again, one can clearly see the strong acceleration effect due to λ_k^N and the somewhat less but still significant acceleration effect due to λ_k^B and λ_k^E , when used together with a constant or the steepest descent stepsize α_k^{SD} , as well as the suboptimal results for combining the minimal error stepsize α_k^{ME} with either λ_k^E or λ_k^B .

Stepsize	$\lambda_k^\delta = 0$	$\lambda_k^\delta = \lambda_k^E$	$\lambda_k^\delta = \lambda_k^B$	$\lambda_k^\delta = \lambda_k^N$	k_*	Time
Steepest Descent	x				5977	856 s
Steepest Descent		x			847	120 s
Steepest Descent			x		431	91 s
Steepest Descent				x	264	40 s
Minimal Error	x				3312	301 s
Minimal Error		x			11600	1039 s
Minimal Error			x		10404	975 s
Minimal Error				x	529	52 s
Constant, $\omega = 4.7 \cdot 10^{-4}$	x				3367	305 s
Constant, $\omega = 4.7 \cdot 10^{-4}$		x			1229	115 s
Constant, $\omega = 4.7 \cdot 10^{-4}$			x		895	96 s
Constant, $\omega = 4.7 \cdot 10^{-4}$				x	326	32 s

Table 5.3: Comparison of different stepsizes α_k^δ and combination parameters λ_k^δ : Number of iterations k_* and total amount of time necessary to satisfy the discrepancy principle. A relative data error of 0.2% was used.

Chapter 6

Applications of Specific TPG Methods

In this chapter, we consider the application of specific versions of TPG method to various ill-posed problems. For the first two examples, based on a nonlinear Hammerstein operator and an auto-convolution problem, we prove the local convexity condition used in Chapter 4 and present numerical examples using the TPG method (2.22). Afterwards, we consider the recently developed medical imaging technique of Magnetic Resonance Advection Imaging (MRAI), for which we present a detailed background and derivation of the underlying parameter estimation problem, and which is then solved by a TPG method based on the extend version of Nesterov's acceleration scheme (2.19). In a final section of this chapter, we survey further problems for which TPG methods have been successfully employed.

6.1 Nonlinear Diagonal Operator

For the first example, we consider the following class of nonlinear diagonal operators

$$F : \ell^2 \rightarrow \ell^2, \quad x := (x_n)_{n \in \mathbb{N}} \mapsto \sum_{n=1}^{\infty} f_n(x_n) e_n$$

where $(e_n)_{n \in \mathbb{N}}$ is the canonical orthonormal basis of ℓ^2 . These operators are reminiscent of the singular value decomposition of compact linear operators. Here we consider the special choice

$$f_n(z) := \frac{1}{n} \cdot \begin{cases} z^2, & n \leq M, \\ z, & n > M, \end{cases} \quad (6.1)$$

for some fixed $M > 0$. For this choice, F takes the form

$$F(x) = \sum_{n=1}^M \frac{1}{n} x_n^2 e_n + \sum_{n=M+1}^{\infty} \frac{1}{n} x_n e_n.$$

It is easy to see that F is a well-defined, twice continuously Fréchet differentiable operator with

$$F'(x)h = 2 \sum_{n=1}^M \frac{1}{n} x_n h_n e_n + 2 \sum_{n=M+1}^{\infty} \frac{1}{n} h_n e_n,$$

$$F''(x)(h, w) = 2 \sum_{n=1}^M \frac{1}{n} h_n w_n e_n.$$

Furthermore, note that solving $F(x) = y$ is equivalent to

$$x_n = n \begin{cases} \sqrt{y_n}, & n \leq M, \\ y_n, & n > M, \end{cases}$$

from which it is easy to see that we are dealing with an ill-posed problem.

We now turn to the convexity of $\Phi^\delta(x)$ around a solution x^\dagger .

Proposition 6.1.1. *Let x^\dagger be a solution of $F(x) = y$ such that $|x_n^\dagger| > 0$ holds for all $n \in \{1, \dots, M\}$. Furthermore, let $\rho > 0$ and $\bar{\delta} \geq 0$ be small enough such that*

$$(x_n^\dagger)^2 \geq 28|x_n^\dagger|\rho + \bar{\delta} (2\|y\|_{\ell^2} + \bar{\delta}), \quad \forall n \in (1, \dots, M), \quad (6.2)$$

and let $x_0 \in \mathcal{B}_\rho(x^\dagger)$. Then for all $0 \leq \delta \leq \bar{\delta}$, the functional $\Phi^\delta(x)$ is convex in $\mathcal{B}_{6\rho}(x_0)$.

Proof. Due to (4.43) it is sufficient to show that

$$0 \leq \|F'(x)h\|^2 + \langle F(x) - y^\delta, F''(x)(h, h) \rangle =$$

$$= \|F'(x)h\|^2 + \langle F(x) - y, F''(x)(h, h) \rangle + \langle y^\delta - y, F''(x)(h, h) \rangle$$

Using the definition of F , the fact that e_n is an orthonormal basis of ℓ^2 and that $F(x^\dagger) = y$, this inequality can be rewritten into

$$2 \left(\sum_{n=1}^M \frac{1}{n^2} x_n^2 h_n^2 + \sum_{n=M+1}^{\infty} \frac{1}{n^2} h_n^2 \right) + 2 \sum_{n=1}^M (x_n^2 - (x_n^\dagger)^2) h_n^2 + 2 \sum_{n=1}^M (y_n^2 - (y_n^\delta)^2) h_n^2 \geq 0,$$

which after simplification, becomes

$$2 \sum_{n=1}^M h_n^2 (2x_n^2 - (x_n^\dagger)^2 + y_n^2 - (y_n^\delta)^2) + 2 \sum_{n=M+1}^{\infty} \frac{1}{n^2} h_n^2 \geq 0.$$

Since the right of the above two sums is always positive, in order for the above inequality to be satisfied it suffices to show that

$$2x_n^2 - (x_n^\dagger)^2 + y_n^2 - (y_n^\delta)^2 \geq 0, \quad \forall n \in \{1, \dots, M\}. \quad (6.3)$$

Now, since by the triangle inequality we have

$$\begin{aligned} |y_n^2 - (y_n^\delta)^2| &= |y_n - y_n^\delta| |y_n + y_n^\delta| \leq \|y - y^\delta\|_{\ell^2} \|y + y^\delta\|_{\ell^2} \\ &\leq \delta (2 \|y\|_{\ell^2} + \|y - y^\delta\|_{\ell^2}) \leq \delta (2 \|y\|_{\ell^2} + \delta), \end{aligned} \quad (6.4)$$

it follows that in order to prove (6.3) it suffices to show

$$2x_n^2 - (x_n^\dagger)^2 - \delta (2 \|y\|_{\ell^2} + \delta) \geq 0, \quad \forall n \in \{1, \dots, M\}.$$

Now, writing $x = x^\dagger + \varepsilon$, this can be rewritten into

$$(x_n^\dagger)^2 + 4x_n^\dagger \varepsilon_n + 2\varepsilon_n^2 - \delta (2 \|y\|_{\ell^2} + \delta) \geq 0, \quad \forall n \in \{1, \dots, M\}.$$

Since $\varepsilon_n^2 \geq 0$, the above inequality is satisfied given that

$$(x_n^\dagger)^2 - 4|x_n^\dagger| |\varepsilon_n| - \delta (2 \|y\|_{\ell^2} + \delta) \geq 0, \quad \forall n \in \{1, \dots, M\}.$$

However, since $|\varepsilon_k| \leq \|\varepsilon\|_{\ell^2} = \|x - x^\dagger\|_{\ell^2} \leq \|x - x_0\|_{\ell^2} + \|x_0 - x^\dagger\|_{\ell^2} \leq 7\rho$, this follows immediately from (6.2), which concludes the proof. \square

Remark. Due to $|x_k^\dagger| \leq \|x_k^\dagger\|_{\ell^2}$, condition (6.2) is satisfied given that

$$\min_{n=1, \dots, M} \{(x_n^\dagger)^2\} \geq 28 \|x^\dagger\|_{\ell^2} \rho + \bar{\delta} (\|y\|_{\ell^2} + \bar{\delta}),$$

which can always be satisfied given that $|x_n^\dagger| > 0$ for all $n \in \{1, \dots, M\}$.

After proving local convexity of the residual functional around the solution, we now proceed to demonstrate the usefulness of method (4.4) based on the following numerical

Example 6.1.1. For this example we choose f_n as in (6.1) with $M = 100$. For the exact solution x^\dagger we take the sequence $x_n^\dagger = 100/n$ which leads to the exact data

$$y_n = F(x^\dagger)_n = \begin{cases} 10^4/n^3, & n \leq 100, \\ 10^2/n^2, & n > 100. \end{cases}$$

Hence, condition (6.3) reads as follows

$$10^4/n^2 \geq 28(10^2/n)\rho + \bar{\delta}(2 \|y\|_{\ell^2} + \bar{\delta}), \quad \forall n \in \{1, \dots, 100\}.$$

Therefore, the functional Φ^0 is convex in $\mathcal{B}_{6\rho}(x_0)$ given that $\rho \leq 1/28 \approx 0.036$, which is for example the case for the choice

$$x_0 = x^\dagger + \left((-1)^n \frac{\rho\sqrt{6}}{\pi n} \right)_{n \in \mathbb{N}}. \quad (6.5)$$

Furthermore, for any noise level $\bar{\delta}$ small enough, one has that for all $\delta \leq \bar{\delta}$ the functional Φ^δ is convex in $\mathcal{B}_{6\rho}(x_0)$ as long as

$$\rho \leq \frac{10^4/n - n\bar{\delta}(2\|y\|_{\ell^2} + \bar{\delta})}{2800}, \quad \forall n \in \{1, \dots, 100\},$$

which for example is satisfied if

$$\rho \leq \frac{1 - \bar{\delta}(2\|y\|_{\ell^2} + \bar{\delta})}{28}.$$

For numerically treating the problem, instead of considering full sequences $x = (x_n)_{n \in \mathbb{N}}$, we only consider $\vec{x} = (x_n)_{n=1, \dots, N}$ where we choose $N = 200$ in this example. This means that we are considering the following discretized version of F :

$$F_n(\vec{x}) = \sum_{n=1}^{100} \frac{1}{n} x_n^2 e_n + \sum_{n=101}^{200} \frac{1}{n} x_n e_n.$$

We now compare the behaviour of method (4.4) with its non-accelerated Landweber counterpart (2.4) when applied to the problem with x^\dagger and x_0 as defined above. For both methods, we choose the same scaling parameter $\omega = 3.2682 \cdot 10^{-5}$ estimated from the norm of $F(x^\dagger)$ and we stop the iteration with the discrepancy principle (2.6) with $\tau = 1$. Furthermore, random noise with a relative noise level of 0.001% was added to the data to arrive at the noisy data y^δ and, following the argument presented after (4.2.2) and since the iterates x_k^δ remain bounded even without it, we drop the proximal operator $\text{prox}_{\omega\Psi}(\cdot)$ in (4.4). The results of the experiments, computed in MATLAB, are displayed in Table 6.1. The speedup both in time and in the number of iterations achieved by Nesterov's acceleration scheme is obvious. Not only does (4.4) satisfy the discrepancy principle much earlier than (2.4), but also the relative error is even a bit smaller for method (4.4).

Method	k_*	Time	$\ x^\dagger - x_k^\delta\ / \ x^\dagger\ $
Landweber	82	0.057 s	0.0109 %
Nesterov	23	0.019 s	0.0108 %

Table 6.1: Comparison of Landweber iteration (2.4) and its Nesterov accelerated version (4.4) when applied to the diagonal operator problem considered in Example 6.1.1.

6.2 Auto-Convolution Problem

For the second example, we look at an inverse problem involving an auto-convolution operator. Due to its importance in laser optics, the auto-convolution problem has been extensively studied in the literature [2, 8, 25], its ill-posedness has been shown

in [11, 23, 27] and its special structure was successfully exploited in [63]. For our purposes, we consider the following version of the auto-convolution operator

$$F : L^2(0, 1) \rightarrow L^2(0, 1), \quad F(x)(s) := (x * x)(s) := \int_0^1 x(s-t)x(t) dt, \quad (6.6)$$

where we interpret functions in $L^2(0, 1)$ as 1-periodic functions on \mathbb{R} . For the following, denote by $(e^{(k)})_{k \in \mathbb{Z}}$ the canonical real Fourier basis of $L^2(0, 1)$, i.e.,

$$e^{(k)}(t) := \begin{cases} 1, & k = 0, \\ \sqrt{2} \sin(2\pi kt), & k \geq 1, \\ \sqrt{2} \cos(2\pi kt), & k \leq -1, \end{cases} \quad t \in (0, 1),$$

and by $x_k := \langle x, e^{(k)} \rangle$ the Fourier coefficients of x . It follows that

$$x * w = \sum_{k \in \mathbb{Z}} x_k w_k e^{(k)}. \quad (6.7)$$

It was shown in [10] that if only finitely many Fourier components x_k are non-zero, then a variational source condition is satisfied leading to convergence rates for Tikhonov regularization. We now use this assumption of a sparse Fourier representation to prove convexity of Φ^δ for the auto-convolution operator in the following

Proposition 6.2.1. *Let x^\dagger be a solution of $F(x) = y$ such that there exists an index set $\Lambda_N \subset \mathbb{Z}$ with $|\Lambda_N| = N$ such that for the Fourier coefficients x_k^\dagger of x^\dagger there holds*

$$x_k^\dagger = 0, \quad \forall k \in \mathbb{Z} \setminus \Lambda_N.$$

Furthermore, let $\rho > 0$ and $\bar{\delta} \geq 0$ be small enough such that

$$(x_k^\dagger)^2 \geq 28|x_k^\dagger| \rho + \bar{\delta} (2\|y\|_{L^2} + \bar{\delta}), \quad \forall k \in \Lambda_N \quad (6.8)$$

and let $x_0 \in \mathcal{B}_\rho(x^\dagger)$. Then for all $0 \leq \delta \leq \bar{\delta}$, the functional $\Phi^\delta(x)$ is convex in $\mathcal{B}_{6\rho}(x_0)$.

Proof. As in the previous example, we want to show that (4.43) is satisfied, which, due to (6.7) and the fact that the $e^{(k)}$ form an orthonormal basis is equivalent to

$$\sum_{k \in \mathbb{Z}} x_k^2 h_k^2 + \sum_{k \in \mathbb{Z}} (x_k^2 - (x_k^\dagger)^2) h_k^2 + \sum_{k \in \mathbb{Z}} ((y_k^\delta)^2 - y_k^2) h_k^2 \geq 0,$$

which, after simplification, becomes

$$\sum_{k \in \mathbb{Z}} h_k^2 \left(2x_k^2 - (x_k^\dagger)^2 + (y_k^\delta)^2 - y_k^2 \right) \geq 0,$$

and hence, it is sufficient to show that

$$2x_k^2 - (x_k^\dagger)^2 + (y_k^\delta)^2 - y_k^2 \geq 0, \quad \forall k \in \mathbb{Z}. \quad (6.9)$$

Note that this is essentially the same condition as (6.3) in the previous example, apart from that here we have to show the inequality for all $k \in \mathbb{Z}$. However, if $k \notin \Lambda_N$, then $x_k^\dagger = y_k = 0$ and hence, (6.9) is trivially satisfied. Hence, it remains to prove (6.9) only for $k \in \Lambda_N$. For this, we write $x_k = x_k^\dagger + \varepsilon_k$, which allows us to rewrite (6.3) into

$$(x_k^\dagger)^2 + 4x_k^\dagger \varepsilon_k + 2\varepsilon_k^2 + (y_k^\delta)^2 - y_k^2 \geq 0 \quad \forall k \in \Lambda_N.$$

Now since we get as in (6.4) that $|y_k^2 - (y_k^\delta)^2| \leq \delta(2\|y\|_{L^2} + \delta)$, it follows that for the above inequality to be satisfied, it suffices to have

$$(x_k^\dagger)^2 - 4|x_k^\dagger| |\varepsilon_k| - \delta(2\|y\|_{L^2} + \delta) \geq 0, \quad \forall k \in \Lambda_N.$$

However, since $|\varepsilon_k| \leq \|\varepsilon\|_{L^2} = \|x - x^\dagger\| \leq \|x - x_0\| + \|x_0 - x^\dagger\| \leq 7\rho$, this immediately follows from (6.8), which completes the proof. \square

Remark. Similarly to the previous example, condition (6.2) is satisfied given that

$$\min_{k \in \Lambda_N} \left\{ (x_k^\dagger)^2 \right\} \geq 28 \|x^\dagger\|_{L^2} \rho + \bar{\delta} (\|y\|_{\ell^2} + \bar{\delta}),$$

which can always be satisfied given that $|x_n^\dagger| > 0$ for all $n \in \{1, \dots, M\}$.

Remark. Note that one could also consider F as an operator from $H^1(0, 1) \rightarrow L^2(0, 1)$, in which case the local convexity of Φ^δ is still satisfied. Since, as noted in Section 4.3, weak convergence in $H^1(0, 1)$ implies strong convergence in $L^2(0, 1)$, the convergence analysis carried out in the previous section then implies strong subsequential $L^2(0, 1)$ convergence of the iterates x_k^δ of (4.4) to an element $\tilde{x} \in \mathcal{S}$ from the solution set.

Example 6.2.1. For this example, we consider the auto-convolution problem with exact solution $x^\dagger(s) := 10 + \sqrt{2} \sin(2\pi s)$. It follows that

$$x_k^\dagger = \langle x^\dagger, e^{(k)} \rangle = \begin{cases} 10, & k = 0, \\ 1, & k = 1, \\ 0, & \text{else.} \end{cases}$$

and therefore, the convexity condition (6.8) simplifies to the following two inequalities

$$100 \geq 280\rho + \bar{\delta} (2\|y\|_{L^2} + \bar{\delta}), \quad 1 \geq 28\rho + \bar{\delta} (2\|y\|_{L^2} + \bar{\delta}).$$

Hence, for the noise-free case (i.e., $\bar{\delta} = 0$) the functional Φ^0 is convex in $\mathcal{B}_{6\rho}(x_0)$ given that $\rho \leq 1/28 \approx 0.036$ and that $x_0 \in \mathcal{B}_\rho(x^\dagger)$, which is for example the case for the choice $x_0 = 10 + \frac{27}{28}\sqrt{2} \sin(2\pi s)$.

For discretizing the problem, we choose a uniform discretization of the interval $[0, 1]$ into $N = 32$ equally spaced subintervals and introduce the standard finite element

hat functions $\{\psi_i\}_{i=0}^N$ on this subdivision, which we use to discretize both \mathcal{X} and \mathcal{Y} . Following the idea used in [58], we discretize F by the finite dimensional operator

$$F_N(x)(s) := \sum_{i=0}^N f_i(x)\psi_i(s), \quad \text{where} \quad f_i(x) := \int_0^1 x\left(\frac{i}{N} - t\right)x(t)dt. \quad (6.10)$$

For computing the coefficients $f_i(x)$, we employ a 4-point Gaussian quadrature rule on each of the subintervals to approximate the integral in (6.10).

Now we again compare method (4.4) with (2.4). This time, the estimated scaling parameter has the value $\omega = 0.005$ and random noise with a relative noise level of 0.01% was added to the data. Again the discrepancy principle (2.6) with $\tau = 1$ was used and the proximal operator $\text{prox}_{\omega\Psi}(\cdot)$ in (4.4) was dropped. The results of the experiments, computed in MATLAB, are displayed in the left part of Table 6.2. Again the results clearly illustrate the advantages of Nesterov's acceleration strategy, which substantially decreases the required number of iterations and computational time, while leading to a relative error of essentially the same size as Landweber iteration.

The initial guess x_0 used for the experiment above is quite close to the exact solution x^\dagger . Although this is necessary for being able to guarantee convergence by our developed theory, it is not very practical. Hence, we want to see what happens if the solution and the initial guess are so far apart that they are no longer within the guaranteed area of convexity. For this, we consider the choice of $x^\dagger(s) = 10 + \sqrt{2}\sin(8\pi s)$ and $x_0(s) = 10 + \sqrt{2}\sin(2\pi s)$. The result can be seen in the right part of Table 6.2. Landweber iteration was stopped after 10000 iterations without having reached the discrepancy principle since no more progress was visible numerically. Consequently, it is clearly outperformed by (4.4), which manages to converge already after 797 iterations, and with a much better relative error. The resulting reconstructions, depicted in Figure 6.1, once again underline the usefulness of (4.4).

As an interesting remark, note that it seems that for the second example Landweber iteration gets stuck in a local minimum, while (4.4), after staying at this minimum for a while, manages to escape it, which is likely due to the combination step in (4.4).

Method	k_*	Time	$\ x^\dagger - x_k^\delta\ / \ x^\dagger\ $
Landweber	526	57 s	0.0244 %
Nesterov	50	6 s	0.0271 %

Method	k_*	Time	$\ x^\dagger - x_k^\delta\ / \ x^\dagger\ $
Landweber	10000	1067 s	9.57 %
Nesterov	797	87 s	0.65%

Table 6.2: Comparison of Landweber iteration (2.4) and its Nesterov accelerated version (4.4) when applied to the auto-convolution problem considered in Example 6.2.1 for the choice $x^\dagger(s) = 10 + \sqrt{2}\sin(2\pi s)$ and $x_0(s) = 10 + \frac{27}{28}\sqrt{2}\sin(2\pi s)$ (left table) and $x^\dagger(s) = 10 + \sqrt{2}\sin(8\pi s)$ and $x_0(s) = 10 + \sqrt{2}\sin(2\pi s)$ (right table).

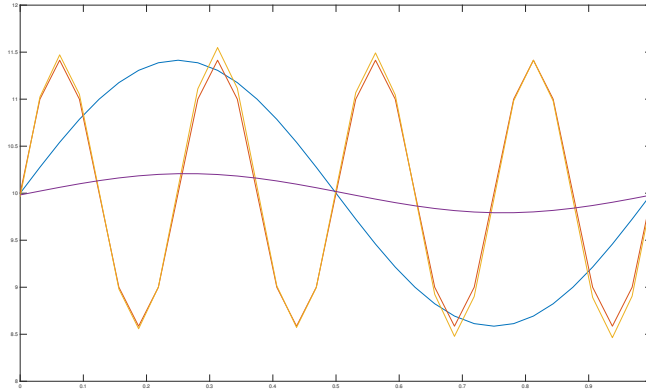


Figure 6.1: Auto-convolution example: Initial guess x_0 (blue), exact solution x^\dagger (red), Landweber (2.4) reconstruction (purple), Nesterov (4.4) reconstruction (yellow).

6.3 Magnetic Resonance Advection Imaging

For the third example, we take a look at the medical imaging technique of Magnetic Resonance Advection Imaging (MRAI), where one aims at estimating the spatially varying Pulse Wave Velocity (PWV) in blood vessels in the brain from dynamic echo planar imaging (EPI) data, such as acquired in functional and resting state functional Magnetic Resonance Imaging (MRI) experiments [80]. The underlying equation connecting the PWV vector field $v(x, y, z)$ to the dynamic MRI signal $\rho(x, y, z, t)$ is the advection equation

$$\frac{\partial}{\partial t}\rho(x, y, z, t) + v(x, y, z) \cdot \nabla\rho(x, y, z, t) = 0. \quad (6.11)$$

It has been suggested that MRAI may potentially serve as a biomarker for the health of the cerebrovascular system. The reason is that MRAI is designed to reflect the spatiotemporal properties of travelling waves, and pulse wave velocities (PWV) are a main indicator for the physical properties of blood vessels. By means of the well-known Moens-Korteweg equation (see (6.12) below), PWVs are related to vessel diameter, wall thickness, and wall stiffness. In particular wall thickness and stiffness are key parameters that change in vascular disease and with age.

In [80], a multiple local regression approach based on finite difference estimators of the differential operators in (6.11) was used to solve the MRAI problem. However, this approach suffered from the ill-posedness of the underlying parameter estimation problem. Hence, we here present a way of treating MRAI within the framework of Ill-Posed Problems and a solution approach based on TPG methods. For this, the problem is formulated as a nonlinear operator equation of the form (2.1). Afterwards, a space-time discretization is used and the resulting large-scale inverse problem is solved using a TPG method of the form (4.4) incorporating sparsity constraints and

utilizing a wavelet embedding. Numerical example problems and a real-world data test show a significant improvement over the results obtained by the previously used method. This section is based on and in parts taken from the research paper [37].

6.3.1 Medical Background

Pulse Wave Velocity

Cardiovascular pulse waves provide a natural physical perturbation to vascular dynamics, and their effects have been utilized in clinical diagnostics for a long time. For example, the PWV in major arteries can be measured directly and contains information about arterial compliance [50], defined as the ratio of blood volume change to blood pressure change. Arterial compliance is an important determinant of the state of the cerebrovascular system. With respect to the brain, aortic stiffness has been associated with cerebral small-vessel disease in hypertensive patients [33] and cognitive decline [64]. In addition, emerging concepts such as pulse wave encephalopathy would profit from diagnostic imaging methods of cerebral vasculature [4, 22].

The PWV in arteries, or Moens-Korteweg velocity [51], follows from the Moens-Korteweg formula [49, 55],

$$v = \sqrt{\frac{Eh}{\rho_B d}}. \quad (6.12)$$

The PWV depends on three parameters: the vascular diameter d , the wall thickness h , and the Young's modulus or distensibility E of the vessel wall, if the reasonable approximation of constant density of the blood, ρ_B , is made. Equation 6.12 models vessels as elastic tubes with isotropic walls [86]. Pressure gradients, which would be required to determine blood flow, do not appear in the Moens-Korteweg formula. In other words, PWVs can be modelled independently from blood flow velocity and in fact can be one to two orders of magnitude faster [51].

For a blood vessel along the direction of v , Equation (6.11) describes the pulsatile component of the blood flow velocity along that direction, with v being the PWV. Importantly, the same advection equation would also hold for blood pressure waves [19], which, by the Windkessel model [70], are a function of the integrated net flow into the vessel reservoir [1]. Since the local blood volume is related to local blood pressure by the compliance C as $dV = C dp$, the same advection equation applies to the pulsatile component of the blood volume as well. For the rest of this section, $\rho(x, y, z, t)$ should be understood as the MRI signal variability attributable to volume change, and we also interpret the three-dimensional velocity vector v as a PWV.

Though $\rho(x, y, z, t)$ depends on the blood flow velocity by the relationship between pulsatile flow, pressure, and volume, the constant component of the flow, or the average blood flow, decouples from Equation (6.11), as it does not cause any spatial or temporal signal change. It could cause signal variability, however, if blood is not assumed to have

homogeneous properties in the model domain Ω , which may be caused by variations in oxygenation or temperature, or any other property that might affect the particular MRI contrast. Here we assume that the MRI signal is not affected by any of these properties.

EPI Data



Figure 6.2: Example image of a clinical MRI scanner.

There are only few in-vivo options for imaging vascular dynamics in the human brain. Arterial spin labelling (ASL) is the most advanced method and has high spatial resolution [83]. It provides quantitative blood flow values in the capillary bed, assuming steady flow. However, arterial compliance depends on the pulsatile component of the flow. It can be imaged with specific ASL pulse sequences [82, 84]. Pulsatile flow components can also be imaged over the whole brain with 4D phase contrast angiography [24].

In this contribution we are aiming at deriving PWV related quantities from echo-planar imaging [77] (EPI) data. EPI is the method of choice for functional MRI [62]. Here we are less interested in the functional aspects of EPI, but in the fact that EPI can also yield fast dynamic data over the whole brain. Since the MRI signal intensity is proportional to the total amount of resonant spins within a voxel, it reflects the local proton distribution, which shows pulsatile information around vessels. This has been demonstrated with phase coherence maps before [79, 80], as well as with statistical parametric mapping [12, 78].

In EPI, images are acquired very rapidly to allow for whole brain coverage within seconds. A typical EPI data set consists of three-dimensional volumes acquired repeatedly in time with a repetition time TR. Each volume contains either the whole brain or always the same part of it. Volumes are acquired slice-by-slice. The typical

spatial resolution or voxel volume depends on the field-of-view, in-plane or slice matrix size, and slice thickness [18]. The field of view typically is 20 to 24 cm in order to include the whole head in axial slices. Slices are either acquired sequentially or interleaved. In sequential acquisition, first slice 1, then slice 2, etc., are acquired, where slice 1 is adjacent to slice 2 and so on. In interleaved acquisition, for example first all odd and then all even slices are acquired. Therefore, care has to be taken to assign the correct acquisition time to each slice, and the model that we are proposing can take slice acquisition order into account. It is described for sequential, specifically, ascending slices, but can easily be adapted to other acquisition schemes. It might be worth mentioning that we are not pursuing a *slice-time correction* [76], which is often performed in the analysis of functional MRI data and consists of an interpolation of intensity values to an evenly sampled time grid. Such a procedure is always of approximative nature and would not sufficiently take into account the fast dynamics of for example travelling pulse waves.

6.3.2 Mathematical Model

Our goal is to estimate velocities of travelling waves in blood vessels from spatiotemporal MRI data. As a first approximation, we neglect any frequency-dependence of the velocity, or dispersion, as well as reflected pulses travelling against the main blood flow direction. The latter assumption means that the back flow amplitude is considered to be much smaller than the forward flow amplitude. This assumption might be violated in some cerebral veins, though, see, e.g., [5].

Under those assumptions, the authors of [80] considered the following local model, defined on small subdomains Ω_S of the model domain Ω , e.g., $3 \times 3 \times 3$ voxels in size. On each subdomain, the dynamic MRI signal $\rho(x, y, z, t)$ is assumed to fulfill the advection equation

$$\frac{\partial}{\partial t} \rho(x, y, z, t) + \bar{v} \cdot \nabla \rho(x, y, z, t) = 0, \quad (6.13)$$

where ∇ is the gradient with respect to the space variables (x, y, z) and $\bar{v} = \bar{v}(\Omega_S)$ is a velocity assumed to be constant on each subdomain Ω_S . Using finite difference approximations of the derivatives of ρ , the authors of [80] used a multiple regression approach to get estimates for the local velocities \bar{v} . Although yielding maps of velocity estimates that reflect main cerebral arteries, those estimates were not quantitative. Furthermore, the local regression matrices used there were ill-conditioned for many of the data points and additionally, the finite difference operators in z -direction used to derive those matrices did not take into account the limited data due to the slice-time acquisition procedure and therefore lead to crude approximations of the z -derivatives.

Hence, here we use an approach which is global in nature, retains the underlying advection equation and gets rid of the numerical instabilities of the regression approach. Following the physical arguments of [81], one can see that ρ is in essence assumed to

be a conserved quantity, for which there holds the following continuity equation

$$\frac{\partial}{\partial t} \rho(x, y, z, t) + \operatorname{div}(\rho(x, y, z, t) v(x, y, z)) = 0, \quad (6.14)$$

where $v = v(x, y, z)$ is a constant-in-time velocity field now defined on the entire model domain Ω . Assuming v to be divergence-free, i.e., $\operatorname{div}(v) = 0$, which is reasonable since we consider a basically incompressible carrier medium (blood), the product rule yields

$$\frac{\partial}{\partial t} \rho(x, y, z, t) + v(x, y, z) \cdot \nabla \rho(x, y, z, t) = 0, \quad (6.15)$$

which is again an advection equation, now defined on the entire model domain Ω . Given measurements of $\rho(x, y, z, t)$, we want to recover the global but now space dependent velocity vector field v satisfying the above equation. This is an ill-posed problem, one reason being that derivatives of ρ are taken in (6.15), which, as the data ρ is subject to measurement errors, is an ill-posed procedure in itself.

Note that v is assumed to be independent of the time t . This assumption stems from the fact that the pulse-wave velocity is primarily dependent on time independent quantities such as vessel wall property parameters, see (6.12).

Note now that we are trying to reconstruct the vector valued quantity v from one single scalar equation. Even worse, assuming that v is a solution of (6.15), every $v + h$, where h satisfies $h \cdot \nabla \rho = 0$, is a solution as well. However, following again the physical arguments of [80], velocities h satisfying $h \cdot \nabla \rho = 0$ are of no interest to us and are in fact not detectable by our algorithm.

We could now consider the inverse problem in the continuous setting, first defining a nonlinear operator mapping between suitable function spaces, then choosing a solution method and finally discretizing. This approach turns out to be highly complicated, as the solution theory of advection equations with non-Lipschitz velocity vector fields is quite involved, see e.g., [17]. Most problematic is the fact that the Lax-Milgram framework commonly used for PDEs is no longer applicable in that case, resulting in solution concepts which are hard to handle.

Hence, we use a first-discretize-then-regularize approach, which simplifies the subsequent computations significantly. However, we use one fact from the classical theory, see [17], namely that v should be at least an H^1 , or locally H^1 vector field.

6.3.3 Discretization

Motivated by the above considerations, we assume that as the pulse wave travels through the brain, the dynamic MRI signal $\rho = \rho(x, y, z, t)$ fulfills the advection equation, i.e.,

$$\frac{\partial}{\partial t} \rho(x, y, z, t) + \nabla \rho(x, y, z, t) \cdot v(x, y, z) = 0, \quad (x, y, z) \in \Omega, t \in [0, T]. \quad (6.16)$$

where $v = (v_1, v_2, v_3)$ is a velocity vector field assumed to be independent of time t and which is additionally assumed to be divergence-free, i.e., satisfies $\text{div}(v) = 0$.

It is the aim to estimate v from measurements of ρ . We assume (for simplicity) that the brain domain Ω is a cuboid and that pointwise measurements are available at certain points. Unfortunately (see Section 6.3.1), the time coordinate is linked to the z -coordinate, i.e., measurements are available only at points

$$(x_i, y_j, z_k, t_{k,l}), \quad 0 \leq i \leq I, 0 \leq j \leq J, 0 \leq k \leq K, 0 \leq l \leq L, \quad (6.17)$$

where

$$x_i := x_0 + i\Delta x, \quad y_j := y_0 + j\Delta y, \quad z_k := z_0 + k\Delta z, \quad t_{k,l} := (k + (K + 1)l)\Delta t.$$

This corresponds to ascending slice acquisition and means that in each time step, only one z -slice can be measured and that after a full cycle, the measurement process restarts.

In a next step, the equation (6.16) is discretized according to the data, which leads to a space-time discretization, which we see below. The derivative with respect to t is approximated by a backwards differential quotient, the derivatives with respect to x, y, z by central quotients in the interior and by forward or backward quotients at the boundary. We then get the following discretized system of equations:

$$\frac{\rho_{i,j,k,l} - \rho_{i,j,k,l-1}}{(K + 1)\Delta t} + D_{x_i}\rho_{i,j,k,l}v_{1,i,j,k} + D_{y_j}\rho_{i,j,k,l}v_{2,i,j,k} + D_{z_k}\rho_{i,j,k,l}v_{3,i,j,k} = 0, \quad (6.18)$$

$0 \leq i \leq I, 0 \leq j \leq J, 0 \leq k \leq K$, and $1 \leq l \leq L$. Here

$$\rho_{i,j,k,l} = \rho(x_i, y_j, z_k, t_{k,l}) \quad \text{and} \quad v_{s,i,j,k} = v_s(x_i, y_j, z_k), \quad s = 1, 2, 3.$$

We still have to define the differential quotients $D_{x_i}, D_{y_j}, D_{z_k}$. One has to be very careful with D_{z_k} , since ρ does not exist at neighbouring z values at the same time steps. Therefore, the appropriate values are then obtained by interpolation or even extrapolation if $l = L$:

$$D_{x_i}\rho_{i,j,k,l} := \begin{cases} \frac{\rho_{i+1,j,k,l} - \rho_{i-1,j,k,l}}{2\Delta x}, & 1 \leq i \leq I - 1, \\ \frac{\rho_{1,j,k,l} - \rho_{0,j,k,l}}{\Delta x}, & i = 0, \\ \frac{\rho_{I,j,k,l} - \rho_{I-1,j,k,l}}{\Delta x}, & i = I, \end{cases} \quad (6.19)$$

$$D_{y_j}\rho_{i,j,k,l} := \begin{cases} \frac{\rho_{i,j+1,k,l} - \rho_{i,j-1,k,l}}{2\Delta y}, & 1 \leq j \leq J - 1, \\ \frac{\rho_{i,1,k,l} - \rho_{i,0,k,l}}{\Delta y}, & j = 0, \\ \frac{\rho_{i,J,k,l} - \rho_{i,J-1,k,l}}{\Delta y}, & j = J, \end{cases} \quad (6.20)$$

$$D_{z_k} \rho_{i,j,k,l} := \begin{cases} \frac{(1-r)(\rho_{i,j,k+1,l} - \rho_{i,j,k-1,l+1}) + r(\rho_{i,j,k+1,l-1} - \rho_{i,j,k-1,l})}{2\Delta z}, & 1 \leq k \leq K-1, 1 \leq l < L, \\ \frac{(1-r)\rho_{i,j,k+1,L} - (1+r)\rho_{i,j,k-1,L} + r(\rho_{i,j,k+1,L-1} + \rho_{i,j,k-1,L-1})}{2\Delta z}, & 1 \leq k \leq K-1, l = L, \\ \frac{(1-r)\rho_{i,j,1,l} + r\rho_{i,j,1,l-1} - \rho_{i,j,0,l}}{\Delta z}, & k = 0, 1 \leq l \leq L, \\ \frac{\rho_{i,j,K,l} - (1-r)\rho_{i,j,K-1,l+1} - r\rho_{i,j,K-1,l}}{\Delta z}, & k = K, 1 \leq l < L, \\ \frac{\rho_{i,j,K,L} - (1+r)\rho_{i,j,K-1,L} + r\rho_{i,j,K-1,L-1}}{\Delta z}, & k = K, l = L, \end{cases}$$

$$r := \frac{1}{K+1}.$$

Note that the denominator $(K+1)\Delta t$ in the approximation of the time derivative in (6.18) seems rather large. However, due to the slice-time acquisition procedure, i.e., since consecutive measurements at the same spatial position are made with a time difference of exactly $(K+1)\Delta t$, this time step is the smallest one available. We observe the consequences of this fact in the numerical simulations presented in Section 6.3.5.

We want to write the equations (6.18) in matrix-vector form. For this, we first collect all $\rho_{i,j,k,l}$ values ($l > 0$) in the vector $\vec{\rho}$ and all $\rho_{i,j,k,l}$ values ($l = 0$) in the vector $\vec{\rho}_0$, where we use the lexicographic ordering with respect to (i, j, k, l) to sort the values inside $\vec{\rho}$ and $\vec{\rho}_0$. The vector $\vec{\rho}$ then has length $m := (I+1)(J+1)(K+1)L$ and the vector $\vec{\rho}_0$ has length $n := (I+1)(J+1)(K+1)$. If we define the indices

$$\begin{aligned} \text{ind}_{i,j,k,l}^m &:= i(J+1)(K+1)L + j(K+1)L + kL + l, \\ \text{ind}_{i,j,k}^n &:= i(J+1)(K+1) + j(K+1) + k + 1, \end{aligned} \quad (6.21)$$

then the relationship between $\rho_{i,j,k,l}$ and $\vec{\rho}$ and $\vec{\rho}_0$ can be written precisely by

$$\begin{aligned} \rho_{i,j,k,l} &= (\vec{\rho})_{\text{ind}_{i,j,k,l}^m}, \\ \rho_{i,j,k,0} &= (\vec{\rho}_0)_{\text{ind}_{i,j,k}^n}. \end{aligned} \quad (6.22)$$

Next, we collect all $v_{s,i,j,k}$ values in a vector \vec{v} of length $3n$, using again a lexicographic ordering but now with respect to (s, i, j, k) , which leads to the relation

$$v_{s,i,j,k} = (\vec{v})_{(s-1)n + \text{ind}_{i,j,k}^n}. \quad (6.23)$$

We want to write (6.18) in the following matrix-vector form:

$$A(\vec{v})\vec{\rho} = b(\vec{v}, \vec{\rho}_0), \quad (6.24)$$

where $A(\vec{v})$ is an $m \times m$ matrix and $b(\vec{v}, \vec{\rho}_0)$ is a vector of length m . This is possible, since $\rho_{i,j,k,l}$ appears only linearly in (6.18). In order to assemble the system matrix $A(\vec{v})$, note first that (6.18) naturally divides into four parts, each part corresponding to the differential quotient with respect to one of the variables t, x, y or z . Hence, the system matrix $A(\vec{v})$ naturally splits up into four parts, i.e.,

$$A(\vec{v}) := A^t + A^x(\vec{v}) + A^y(\vec{v}) + A^z(\vec{v}), \quad (6.25)$$

where $A^t, A^x(\vec{v}), A^y(\vec{v})$ and $A^z(\vec{v})$ are $m \times m$ matrices corresponding to the differential quotients. They can be assembled by looping over all possible values of (i, j, k, l) and setting suitable values at the positions implicitly defined by the difference quotients. For example, for the matrix $A^x(\vec{v})$, considering the definition (6.19) of D_{x_i} , this assembly procedure looks as follows:

- Create an all-zero $m \times m$ matrix A .
- For $i = 0, \dots, I, k = 0, \dots, K, j = 0, \dots, J$ and $l = 1, \dots, L$ do:

Set $\text{ind} := \text{ind}_{i,j,k,l}^m$ and $\text{step} := (J + 1)(K + 1)L$.

If $(i = 0)$ {

$$\text{padding-left: 80px; } A_{\text{ind}, \text{ind} + \text{step}} = \vec{v}_{\text{ind}} / \Delta x,$$

$$\text{padding-left: 80px; } A_{\text{ind}, \text{ind}} = -\vec{v}_{\text{ind}} / \Delta x.$$

}

Elseif $(i = I)$ {

$$\text{padding-left: 80px; } A_{\text{ind}, \text{ind}} = \vec{v}_{\text{ind}} / \Delta x,$$

$$\text{padding-left: 80px; } A_{\text{ind}, \text{ind} - \text{step}} = -\vec{v}_{\text{ind}} / \Delta x.$$

}

Else {

$$\text{padding-left: 80px; } A_{\text{ind}, \text{ind} + \text{step}} = \vec{v}_{\text{ind}} / (2\Delta x),$$

$$\text{padding-left: 80px; } A_{\text{ind}, \text{ind} - \text{step}} = -\vec{v}_{\text{ind}} / (2\Delta x).$$

}

- Set $A^x(\vec{v}) := A$.

For the matrices $A^t, A^y(\vec{v})$ and $A^z(\vec{v})$, the assembly procedure looks similar, with obvious modifications due to the respective definitions of D_{y_j}, D_{z_k} and the backwards time difference quotient in (6.18).

From the assembly procedure, one can see that $A^t, A^x(\vec{v}), A^y(\vec{v})$ and $A^z(\vec{v})$ are sparse matrices, with A^t having only 2 non-zero (off-)diagonals, both $A^x(\vec{v})$ and $A^y(\vec{v})$ having 3 non-zero (off-)diagonals and $A^z(\vec{v})$ having 6 non-zero (off-)diagonals. Hence, the system matrix $A(\vec{v})$ is sparse as well, with (note that all four matrices share the non-zero main diagonal) only 11 non-zero (off-)diagonals.

As for the right-hand side in (6.24), one could again loop over all indices (i, j, k, l) to assemble it, or alternatively use the closed formula

$$b(\vec{v}, \vec{\rho}_0)_{\text{ind}_{i,j,k,l}^m} := \begin{cases} \frac{1}{(K+1)\Delta t}(\vec{\rho}_0)_{\text{ind}_{i,j,k}^n} - \frac{r}{2\Delta z}(\vec{\rho}_0)_{\text{ind}_{i,j,k+1}^n} (\vec{v})_{2n+\text{ind}_{i,j,k}^n}, & l = 1, 1 \leq k < K, \\ \frac{1}{(K+1)\Delta t}(\vec{\rho}_0)_{\text{ind}_{i,j,k}^n} - \frac{r}{\Delta z}(\vec{\rho}_0)_{\text{ind}_{i,j,k+1}^n} (\vec{v})_{2n+\text{ind}_{i,j,k}^n}, & l = 1, 1 \leq k < K, \\ 0, & \text{else.} \end{cases} \quad (6.26)$$

The forward problem consists in calculating $\vec{\rho}$ for given \vec{v} and given initial data $\vec{\rho}_0$, by solving (6.24). Let us denote this solution by $\rho(\vec{v}, \vec{\rho}_0)$.

Note that in order to guarantee unique solvability of (6.15), one usually prescribes boundary conditions on $\partial\Omega$. However, since for our problem sufficient boundary data are not available, we used forward and backward differential quotients in the definition of D_{x_i} , D_{y_j} and D_{z_k} at the boundary. It can easily be seen that this amounts to linear extrapolation of ρ and is also the reason why (6.24) turns out to be solvable.

The Inverse Problem

Let us now turn to the inverse problem. It consist in calculating the velocity \vec{v} and the initial data $\vec{\rho}_0$ for given measurements of $\vec{\rho}$ and $\vec{\rho}_0$. Introducing the nonlinear operator

$$F(\vec{v}, \vec{\rho}_0) := (\rho(\vec{v}, \vec{\rho}_0), \vec{\rho}_0) \in \mathbb{R}^{m+n}, \quad (6.27)$$

our inverse problem can be written in the standard form

$$F(\vec{v}, \vec{\rho}_0) = (\vec{\rho}, \vec{\rho}_0). \quad (6.28)$$

The additional equation $\rho_0 = \rho_0$ in (6.28) seems to be superfluous at first. Note however, that as a result of measurement errors, we are not really given $\vec{\rho}$ and $\vec{\rho}_0$, but only noisy data $\vec{\rho}^\delta$ and $\vec{\rho}_0^\delta$ and hence, including this equation becomes necessary.

Concerning the solvability of (6.28), note that in essence we are trying to reconstruct $\vec{v} \in (\mathbb{R}^n)^3$ from $\vec{\rho} \in \mathbb{R}^m$, which means that we are given m data points and try to solve for $3n$ unknowns. Hence, in general one can only hope for a unique solution to this problem in case that $m \geq 3n$, which is always satisfied given data with a large enough L , i.e., a long enough scanning time, is being used. This is always be the case in the tests below. If (6.28) happens to be overdetermined, our solution approach presented below picks a suitable solution out of all possible ones. Moreover, it could happen that even for $m \geq 3n$ problem (6.28) is underdetermined (compare with the well-known aperture problem). As described above, the main reason for this is that it could happen that the velocity vector field v is orthogonal to $\nabla\rho$ at certain points in space for the entire scanning period. In this very unlikely case, velocity components orthogonal to $\nabla\rho$ could not be detected at certain points. However, as noted above, those components are not of interest to us and the reconstruction algorithm introduced

below computes approximations of the velocity vector field without those orthogonal components in this case.

In order to solve (6.28), we need the derivative and its adjoint of F . For this, we consider F as an operator from \mathcal{X} to \mathcal{Y} , where

$$\begin{aligned}\mathcal{X} &= \{(\vec{v}, \vec{\rho}_0) \mid \vec{v} \in (\mathbb{R}^n)^3, \vec{\rho}_0 \in \mathbb{R}^n\}, \\ \mathcal{Y} &= \{(\vec{\rho}, \vec{\rho}_0) \mid \vec{\rho} \in \mathbb{R}^m, \vec{\rho}_0 \in \mathbb{R}^n\}.\end{aligned}\tag{6.29}$$

We equip \mathcal{X} and \mathcal{Y} with the inner products

$$\begin{aligned}\langle (\vec{v}, \vec{\rho}_0), (\vec{x}, \vec{w}_0) \rangle_{\mathcal{X}} &:= \vec{v}^T H \vec{x} + \vec{\rho}_0^T \vec{w}_0, \\ \langle (\vec{\rho}, \vec{\rho}_0), (\vec{w}, \vec{w}_0) \rangle_{\mathcal{Y}} &:= \vec{\rho}^T \vec{w} + \vec{\rho}_0^T \vec{w}_0,\end{aligned}\tag{6.30}$$

where H is a positive definite $3n \times 3n$ matrix chosen such that the inner product is an approximation of the H^1 -inner product of functions v , see also Section 6.3.3.

Before we proceed with the derivation of the Fréchet derivative and its adjoint, we introduce the following notation: Whenever we have an arbitrary Fréchet-differentiable function G between suitable spaces A and B and we are given $x \in A$ and $\Delta x \in A$, then we denote by $G'(x)\Delta x$ the Fréchet derivative of G at x in the direction of Δx . This notation is used multiple times in the following:

Lemma 6.3.1. *Let $F : \mathcal{X} \rightarrow \mathcal{Y}$ be given as in (6.27) and let $(\vec{v}, \vec{\rho}_0) \in \mathbb{R}^{3n+n}$ and $(\Delta\vec{v}, \Delta\vec{\rho}_0) \in \mathbb{R}^{3n+n}$. Then for the Fréchet derivative of F there holds*

$$F'(\vec{v}, \vec{\rho}_0)(\Delta\vec{v}, \Delta\vec{\rho}_0) = (\rho'(\vec{v}, \vec{\rho}_0)(\Delta\vec{v}, \Delta\vec{\rho}_0), \Delta\vec{\rho}_0),\tag{6.31}$$

where $\rho'(\vec{v}, \vec{\rho}_0)(\Delta\vec{v}, \Delta\vec{\rho}_0)$, the Fréchet derivative of ρ , is given as the solution of

$$A(\vec{v})[\rho'(\vec{v}, \vec{\rho}_0)(\Delta\vec{v}, \Delta\vec{\rho}_0)] = -(A'(\vec{v})\Delta\vec{v})\rho(\vec{v}, \vec{\rho}_0) + b'(\vec{v}, \vec{\rho}_0)(\Delta\vec{v}, \Delta\vec{\rho}_0),\tag{6.32}$$

where A' and b' are the Fréchet derivatives of A and b , respectively, and therefore $A'(\vec{v})\Delta\vec{v} \in \mathbb{R}^{m \times m}$ and $b'(\vec{v}, \vec{\rho}_0) \in \mathbb{R}^{m \times (3n+n)}$.

Proof. First, note that (6.31) follows immediately from the definition of the Fréchet derivative. Now, from equation (6.24), we know that

$$A(\vec{v})\rho(\vec{v}, \vec{\rho}_0) = b(\vec{v}, \vec{\rho}_0).\tag{6.33}$$

Applying the Fréchet-derivative at the point $(\vec{v}, \vec{\rho}_0)$ in the direction of $(\Delta\vec{v}, \Delta\vec{\rho}_0)$ to this equation and using the chain rule yields

$$(A'(v)\Delta\vec{v})\rho(\vec{v}, \vec{\rho}_0) + A(\vec{v})[\rho'(\vec{v}, \vec{\rho}_0)(\Delta\vec{v}, \Delta\vec{\rho}_0)] = b'(\vec{v}, \vec{\rho}_0)(\Delta\vec{v}, \Delta\vec{\rho}_0),\tag{6.34}$$

from which the statement of the lemma now immediately follows. \square

It follows from (6.31) and (6.32) that in order to calculate $F'(\vec{v}, \vec{\rho}_0)(\Delta\vec{v}, \Delta\vec{\rho}_0)$, a linear system of equations involving the vectors $(A'(v)\Delta\vec{v})\rho(\vec{v}, \vec{\rho}_0)$ and $b'(\vec{v}, \vec{\rho}_0)(\Delta\vec{v}, \Delta\vec{\rho}_0)$ needs to be solved. It is possible to calculate those vectors without assembling the matrices $(A'(v)\Delta\vec{v})$ and $b'(\vec{v}, \vec{\rho}_0)$. However, as we see in the lemma below, the assembly of three specific matrices is inevitable for calculating the adjoint of the derivative of F , and those matrices can then also be used to compute the two required vectors.

To arrive at these matrices, note first that it follows from the assembly procedure described above that $A^x(\vec{v})$, $A^y(\vec{v})$ and $A^z(\vec{v})$ depend only linearly on \vec{v} . Together with (6.25) and the definition of the Fréchet derivative, it follows that

$$A'(\vec{v})\Delta\vec{v} = A^x(\Delta\vec{v}) + A^y(\Delta\vec{v}) + A^z(\Delta\vec{v}), \quad (6.35)$$

and hence $A'(\vec{v})\Delta\vec{v}$ is not only linear in $\Delta\vec{v}$ but also independent of \vec{v} . As a result, it is possible to find a matrix $D_A(\rho) \in \mathbb{R}^{m \times 3n}$ such that

$$(A'(\vec{v})\Delta\vec{v})\rho(\vec{v}, \vec{\rho}_0) = D_A(\rho(\vec{v}, \vec{\rho}_0))\Delta\vec{v}. \quad (6.36)$$

As for the other two matrices, note that once one has assembled $b'(\vec{w}, \vec{\rho}_0)$, which can be calculated easily using (6.26), this matrix can be split up into two sub-matrices, i.e.,

$$b'(\vec{w}, \vec{\rho}_0) = (b'_{\Delta\vec{v}}(\vec{w}, \vec{\rho}_0) \mid b'_{\Delta\vec{\rho}_0}(\vec{w}, \vec{\rho}_0)), \quad (6.37)$$

where $b'_{\Delta\vec{v}}(\vec{w}, \vec{\rho}_0) \in \mathbb{R}^{m \times 3n}$ and $b'_{\Delta\vec{\rho}_0}(\vec{w}, \vec{\rho}_0) \in \mathbb{R}^{m \times n}$ are the derivatives corresponding to $\Delta\vec{v}$ and $\Delta\vec{\rho}_0$, respectively.

Thanks to the special structure of $A(\vec{v})$ and $b(\vec{v}, \vec{\rho}_0)$, when following the above derivation steps in detail, one finds out that most of the elements of the matrices

$$D_A(\rho) \quad \text{and} \quad b'(\vec{v}, \vec{\rho}_0) \quad (6.38)$$

are zero, with at most three non-zero elements in each row in both cases.

Using the above derivations, we can now prove the following

Lemma 6.3.2. *Let $F : \mathcal{X} \rightarrow \mathcal{Y}$ be given as in (6.27) and let $(\vec{v}, \vec{\rho}_0) \in \mathbb{R}^{3n+n}$ and $(\vec{w}, \vec{w}_0) \in \mathbb{R}^{m+n}$. Then for the adjoint of the Fréchet derivative of F there holds*

$$F'(\vec{v}, \vec{\rho}_0)^*(\vec{w}, \vec{w}_0) := \begin{pmatrix} H^{-1} \left(-D_A(\rho(\vec{v}, \vec{\rho}_0))^T + b'_{\Delta\vec{v}}(\vec{v}, \vec{\rho}_0)^T \right) A(\vec{v})^{-T} \vec{w} \\ b'_{\Delta\vec{\rho}_0}(\vec{v}, \vec{\rho}_0)^T A(\vec{v})^{-T} \vec{w} + \vec{w}_0 \end{pmatrix}. \quad (6.39)$$

Proof. To compute the adjoint, consider first

$$\begin{aligned} & \langle F'(\vec{v}, \vec{\rho}_0)(\Delta\vec{v}, \Delta\vec{\rho}_0), (\vec{w}, \vec{w}_0) \rangle_{\mathcal{Y}} = \\ & = \langle (-A(\vec{v})^{-1} D_A(\rho(\vec{v}, \vec{\rho}_0))\Delta\vec{v} + A(\vec{v})^{-1} b'(\vec{v}, \vec{\rho}_0)(\Delta\vec{v}, \Delta\vec{\rho}_0), \Delta\vec{\rho}_0), (\vec{w}, \vec{w}_0) \rangle_{\mathcal{Y}} \\ & = (-A(\vec{v})^{-1} D_A(\rho(\vec{v}, \vec{\rho}_0))\Delta\vec{v})^T \vec{w} + (A(\vec{v})^{-1} b'(\vec{v}, \vec{\rho}_0)(\Delta\vec{v}, \Delta\vec{\rho}_0))^T \vec{w} + \Delta\vec{\rho}_0^T \vec{w}_0 \\ & = -\Delta\vec{v}^T D_A(\rho(\vec{v}, \vec{\rho}_0))^T A(\vec{v})^{-T} \vec{w} + (\Delta\vec{v}, \Delta\vec{\rho}_0)^T b'(\vec{v}, \vec{\rho}_0)^T A(\vec{v})^{-T} \vec{w} + \Delta\vec{\rho}_0^T \vec{w}_0 \end{aligned}$$

Splitting up $b'(\vec{w}, \vec{\rho}_0)$ as in (6.37), we get

$$\begin{aligned} \langle F'(\vec{v}, \vec{\rho}_0)(\Delta\vec{v}, \Delta\vec{\rho}_0), (\vec{w}, \vec{w}_0) \rangle_{\mathcal{Y}} &= \Delta\vec{\rho}_0^T b'_{\Delta\vec{\rho}_0}(\vec{v}, \vec{\rho}_0)^T A(\vec{v})^{-T} \vec{w} + \Delta\vec{\rho}_0^T \vec{w}_0 \\ &\quad + \Delta\vec{v}^T (-D_A(\rho(\vec{v}, \vec{\rho}_0))^T + b'_{\Delta\vec{v}}(\vec{v}, \vec{\rho}_0)^T) A(\vec{v})^{-T} \vec{w} \end{aligned}$$

and hence, using the definition of the inner product in \mathcal{X} , the statement follows. \square

Incorporating the Divergence-Free Condition

Up to now, the divergence-free condition $\operatorname{div}(v) = 0$ on the velocity field to be reconstructed did not enter the reconstruction method. However, it is a modelling assumption and has to be taken care of.

One possible way to do so would be to incorporate the condition into the space \mathcal{X} , i.e., allowing only divergence-free vector fields in \mathcal{X} . This approach essentially, except at the boundary, implies $v_3 = v_3(v_1, v_2)$. This changes the derivative and its adjoint of F in a computationally unfavourable way and hence we avoid this approach.

Instead, we enforce the divergence-free condition in a weak way, by changing F to

$$F(\vec{v}, \vec{\rho}_0) := (\rho(\vec{v}, \vec{\rho}_0), \vec{\rho}_0, D\vec{v}), \quad (6.40)$$

where D is a matrix representing the divergence-free condition. The operator F now maps from \mathcal{X} to \mathcal{Y} with \mathcal{X} as before and

$$\mathcal{Y} = \{(\vec{\rho}, \vec{\rho}_0, \vec{w}) \mid \vec{\rho} \in \mathbb{R}^m, \vec{\rho}_0 \in \mathbb{R}^n, \vec{w} \in \mathbb{R}^n\}, \quad (6.41)$$

where we use the following inner product

$$\langle (\vec{\rho}, \vec{\rho}_0, \vec{v}_d), (\vec{w}, \vec{w}_0, \vec{w}_d) \rangle_{\mathcal{Y}} = \vec{\rho}^T \vec{w} + \vec{\rho}_0^T \vec{w}_0 + \vec{v}_d^T \vec{w}_d. \quad (6.42)$$

The resulting nonlinear inverse problem now reads as

$$F(\vec{v}, \vec{\rho}_0) = (\rho, \rho_0, \vec{0}). \quad (6.43)$$

An analogous calculation as before yields that the Fréchet derivative of F is given by

$$F'(\vec{v}, \vec{\rho}_0)(\Delta\vec{v}, \Delta\vec{\rho}_0) = (\rho'(\vec{v}, \vec{\rho}_0), \Delta\vec{\rho}_0, D\Delta\vec{v}), \quad (6.44)$$

and that the adjoint is given by

$$\begin{aligned} &F'(\vec{v}, \vec{\rho}_0)^*(\vec{w}, \vec{w}_0, \vec{w}_d) \\ &= \begin{pmatrix} H^{-1} [(-D_A(\rho(\vec{v}, \vec{\rho}_0))^T + b'_{\Delta\vec{v}}(\vec{v}, \vec{\rho}_0)^T) A(\vec{v})^{-T} \vec{w} + D^T \vec{w}_d] \\ b'_{\Delta\vec{\rho}_0}(\vec{v}, \vec{\rho}_0)^T A(\vec{v})^{-T} \vec{w} + \vec{w}_0 \end{pmatrix}. \end{aligned}$$

As for the choice of the matrix D , note that since, due to the Divergence Theorem,

$$\operatorname{div}(v)(x, y, z) = \lim_{|V| \rightarrow 0} \frac{1}{|V|} \int_{\partial V} v \, dS(x, y, z), \quad (6.45)$$

we may approximate the divergence in $\Omega_{i,j,k} := [x_{i-1}, x_i] \times [y_{j-1}, y_j] \times [z_{k-1}, z_k]$ by the integral above with $V = \Omega_{i,j,k}$. Assuming that each component of v is piecewise linear (tri-linear), divergence-free then means

$$D_1 v_{1,i,j,k} + D_2 v_{2,i,j,k} + D_3 v_{3,i,j,k} = 0, \quad (6.46)$$

where $1 \leq i \leq I$, $1 \leq j \leq J$, $1 \leq k \leq K$, and

$$D_1 v_{1,i,j,k} := \frac{1}{4\Delta x} (v_{1,i,j-1,k-1} - v_{1,i-1,j-1,k-1} + v_{1,i,j-1,k} - v_{1,i-1,j-1,k} + v_{1,i,j,k-1} - v_{1,i-1,j,k-1} + v_{1,i,j,k} - v_{1,i-1,j,k}), \quad (6.47)$$

$$D_2 v_{2,i,j,k} := \frac{1}{4\Delta y} (v_{2,i-1,j,k-1} - v_{2,i-1,j-1,k-1} + v_{2,i-1,j,k} - v_{2,i-1,j-1,k} + v_{2,i,j,k-1} - v_{2,i,j-1,k-1} + v_{2,i,j,k} - v_{2,i,j-1,k}), \quad (6.48)$$

$$D_3 v_{3,i,j,k} := \frac{1}{4\Delta z} (v_{3,i-1,j-1,k} - v_{3,i-1,j-1,k-1} + v_{3,i-1,j,k} - v_{3,i-1,j,k-1} + v_{3,i,j-1,k} - v_{3,i,j-1,k-1} + v_{3,i,j,k} - v_{3,i,j,k-1}). \quad (6.49)$$

The (sparse!) matrix D is now built such that $D\vec{v} = 0$ is equivalent to (6.46).

Whenever we speak of the *weak divergence-free option* in subsequent sections, we mean that we use F defined as in (6.40). As it turns out in our numerical tests below, using this option has a significant effect on the reconstructed solutions.

Choosing the Matrix H

We now turn to the choice of the matrix H in the inner product of \mathcal{X} . From the theory of transport equations (see e.g. [17]), we know that v should be at least an H^1 velocity field. Assuming as above that each component of v is piecewise linear and can hence be written in the form

$$v(x, y, z) = \sum_{i,j,k} \begin{pmatrix} v_{1,i,j,k} \\ v_{2,i,j,k} \\ v_{3,i,j,k} \end{pmatrix} \psi_{i,j,k}(x, y, z), \quad (6.50)$$

where the $\psi_{i,j,k}$ are the 3D hat functions commonly used to form a basis in H^1 -FEM, we find that the optimal choice of H in this case would be,

$$H = c_s \text{diag}(\tilde{H}, \tilde{H}, \tilde{H}), \quad \tilde{H} = [\langle \psi_{i,j,k}, \psi_{l,m,n} \rangle_{H^1}]. \quad (6.51)$$

where c_s is a suitable scaling constant. As can easily be seen, \tilde{H} is the FEM system matrix of the equation $-\Delta u + u = f$. However, in the computation of the adjoint of F we need to apply H^{-1} , or equivalently three times \tilde{H}^{-1} , which amounts to solving three perturbed Laplace equations in each iteration step. This is way too costly and hence we need to find a suitable alternative for inverting the matrix H .

One possibility is to approximate \tilde{H} by its diagonal part, which leads to a diagonal matrix H that is easy to assemble and to invert, i.e.,

$$H = c_s \text{diag}(\tilde{H}, \tilde{H}, \tilde{H}), \quad \tilde{H} = \text{diag}(\langle \psi_{i,j,k}, \psi_{i,j,k} \rangle_{H^1}). \quad (6.52)$$

The scaling constant c_s is chosen such that the two terms on the right hand side of (6.30) are balanced and that the H^1 and the L^2 norm approximations of constant vectors coincide, which leads to the choice

$$c_s = 3n \left(\sum_{i=1}^{3n} H_{ii} \right)^{-1}. \quad (6.53)$$

Another, more sophisticated possibility is to use an orthogonal system $\psi_{i,j,k}$, e.g., wavelets, since then the matrix \tilde{H} becomes diagonal. One can see that applying \tilde{H}^{-1} coincides with applying the operator i_1^* , where $i_1 : H^1 \rightarrow L^2$ is the embedding operator. For a given wavelet system $\{\phi, \psi\}$, every function $f \in L^2$ can be expanded as

$$f = \sum_{k \in \mathbb{Z}} \langle f, \phi_{0k} \rangle \phi_{0k} + \sum_{j=0}^{\infty} \sum_{k \in \mathbb{Z}} \langle f, \psi_{jk} \rangle \psi_{jk}, \quad (6.54)$$

where $\phi_{0k} = \phi(t - k)$ and $\psi_{jk}(t) = 2^{j/2} \psi(2^j t - k)$. If the wavelet system is sufficiently smooth, then for every Sobolev space, the H^s inner product of two functions f and g is equivalent to

$$\langle f, g \rangle_{H^s} = \sum_{k \in \mathbb{Z}} \langle f, \phi_{0k} \rangle \langle g, \phi_{0k} \rangle + \sum_{j=0}^{\infty} 2^{2js} \sum_{k \in \mathbb{Z}} \langle f, \psi_{jk} \rangle \langle g, \psi_{jk} \rangle. \quad (6.55)$$

Following [66], we see that the adjoint i_s^* of the embedding $i_s : H^s \rightarrow L^2$ is given by

$$i_s^* g = \sum_{k \in \mathbb{Z}} \langle g, \phi_{0k} \rangle \phi_{0k} + \sum_{j=0}^{\infty} \sum_{k \in \mathbb{Z}} \frac{\langle g, \psi_{jk} \rangle}{2^{2js}} \psi_{jk}. \quad (6.56)$$

Using this, we can, instead of applying \tilde{H}^{-1} to the components of \vec{v} , compute their discrete wavelet transforms, weight the resulting coefficients according to (6.56) and then apply the inverse discrete wavelet transforms. The computation of $\vec{v}^T H \vec{w}$ in (6.30) is then replaced by using a scaled version of (6.55), using again the discrete wavelet transform. Thus, whenever we speak of using the *wavelet embedding option* in subsequent sections, we mean that this procedure is being used.

Note that for the results presented below, due to the low spatial resolution, using the wavelet embedding option with $s = 1$ in (6.55) and (6.56) leads to an undesirably high amount of smoothing and subsequently to mediocre results. Using a smaller s and hence less smoothing yields much better results and therefore, the choice $s = 0.1$ was

used in all computations below. As for the choice of wavelets, Daubechies 3 wavelets (see [13]) were used in all cases.

Both approximations of H^{-1} , using only the diagonal entries of H and by the wavelet embedding are very fast (diagonal matrix inversion and $\mathcal{O}(n)$ wavelet decomposition). The use of wavelets has the additional advantage that it yields a very good approximation of the application of H^{-1} , as compared to using the diagonal approximation, which in essence only amounts to a scaling of the steps in the iterative solution method introduced below.

6.3.4 Solution Approach

In this section, we consider the solution of the inverse problems (6.28) and (6.43). Since we are dealing with an ill-posed problem, regularization has to be employed to get stable solutions of these problems. For this, we use a slight extension of the TPG method (2.22) based on (4.4) to incorporating sparsity constraints and combined with the discrepancy principle (2.6) as a stopping rule.

Implementation Details

The implementation of (2.22) seems very straightforward at first, since we have explicit expressions for F' and its adjoint available. However, even though we are dealing with a rather coarse space discretization, since we are essentially using a *space-time approach* with three space dimensions, the problem becomes large-scale, with around 3.3 million unknowns for one of the real-world data sets considered below. This causes severe numerical difficulties.

Please note that for the calculation of one iteration step it is necessary to solve three large sparse linear systems of equations, one for calculating F , one for F' and one for ω^δ . Since, due to the size of the problem, this can no longer be done directly, the iterative solver biCGstab with an incomplete LU factorization preconditioner was used.

The implementation of the method was done in MATLAB R2015b. Since some built-in MATLAB functions were too slow for our purposes, we had to rely on *fsparse.m*, a function for creating sparse matrices, see [20].

Enforcing Sparse Solutions

The relevant blood vessels in which the pulse waves travel constitute only a minor part of the brain. Hence, the velocity vector field v which we seek to reconstruct should take nonzero values in those blood vessels only.

In mathematical terms this means that v should be compactly supported and should have a sparse representation in the basis $\psi_{i,j,k}$. The reconstruction algorithm should take this into account, which leads directly to the concept of sparsity regularization.

Following [67] and [52], we seek to compute $(\vec{v}, \vec{\rho}_0)$ as a minimizer of the functional

$$\frac{1}{2} \left\| F(\vec{v}, \vec{\rho}_0) - (\vec{\rho}^\delta, \vec{\rho}_0^\delta) \right\|_y^2 + \alpha \left(\sum_{l=1}^3 \sum_{i,j,k} \omega_{i,j,k}^{\vec{v}_l} |v_{l,i,j,k}|^p + \sum_{i,j,k} \omega_{i,j,k}^{\vec{\rho}_0} |\rho_{i,j,k,0}|^p \right), \quad (6.57)$$

where $\omega_{i,j,k}^{\vec{v}_l}$ and $\omega_{i,j,k}^{\vec{\rho}_0}$ are positive weights bounded away from zero, α is a regularization parameter and $p \in [1, 2]$. The choice $p = 1$ yields sparse minimizers, while $1 < p < 2$ is suspected to promote sparsity.

For further use below, and for $1 \leq p < \infty$ and $\tau > 0$, we define the *real valued shrinkage function* $S_{\tau,p} : \mathbb{R} \rightarrow \mathbb{R}$ by

$$S_{\tau,p}(x) = \begin{cases} \operatorname{sgn}(x) \max(|x| - \tau, 0), & p = 1, \\ G_{\tau,p}^{-1}(x), & p \in (1, 2], \end{cases} \quad (6.58)$$

where

$$G_{\tau,p}(x) = x + \tau \operatorname{sgn}(x) |x|^{p-1}. \quad (6.59)$$

For a vector $\vec{x} = \{x_k\}_{k \in \Lambda}$ and weights $\omega = \{\omega_k\}_{k \in \Lambda}$ we define the shrinkage function $S_{\omega,p}$ by

$$S_{\omega,p}(\vec{x}) := [S_{\omega_k,p}(x_k)]_{k \in \Lambda}. \quad (6.60)$$

Following [52], a possible method for solving nonlinear inverse problems $F(x) = y^\delta$ involving sparsity constraints is given by the so-called *iterated soft shrinkage algorithm*, which reads as

$$x_{k+1}^\delta = S_{\omega_k \alpha \omega, p}(x_k^\delta + \omega_k F'(x_k^\delta)^*(y^\delta - F(x_k^\delta))), \quad x_0^\delta = x_0. \quad (6.61)$$

For our problem we combine this approach with method (2.22) to arrive, after collecting the $\omega^{\vec{v}_l}$ and $\omega^{\vec{\rho}_0}$ into a single sequence ω^s , at the following iterative scheme:

$$\begin{aligned} (\vec{w}_k^\delta, \vec{w}_{0,k}^\delta) &= (\vec{v}_k^\delta, \vec{\rho}_{0,k}^\delta) + \frac{k-1}{k+2} ((\vec{v}_k^\delta, \vec{\rho}_{0,k}^\delta) - (\vec{v}_{k-1}^\delta, \vec{\rho}_{0,k-1}^\delta)), \\ \omega_k^\delta &= \omega^\delta((\vec{w}_k^\delta, \vec{w}_{0,k}^\delta)), \\ (\vec{v}_{k+1}^\delta, \vec{\rho}_{0,k+1}^\delta) &= S_{\omega_k^\delta \alpha \omega^s, p}((\vec{w}_k^\delta, \vec{w}_{0,k}^\delta) + \omega_k^\delta F'(\vec{w}_k^\delta, \vec{w}_{0,k}^\delta)^*((\vec{\rho}^\delta, \vec{\rho}_0^\delta) - F(\vec{w}_k^\delta, \vec{w}_{0,k}^\delta))). \end{aligned}$$

This is essentially Nesterov's accelerated gradient method (2.19) applied to (6.57), as it is used in FISTA to solve linear inverse problems with sparsity constraints [7].

Note that for this algorithm, values for α , ω^s and p need to be specified. Moreover, if $p > 1$, $4n$ nonlinear equations need to be solved for approximating $G_{\tau,p}^{-1}$. This is very costly, hence we use $p = 1$ only. Furthermore, since we want to weight all $v_{l,i,j,k}$ and $\rho_{i,j,k}$ equally, ω^s was set to 1 for the numerical examples presented below.

Obviously, the above algorithm can also, with minor modifications, be applied to the case when F contains the divergence-free part as introduced in Section 6.3.3.

6.3.5 Numerical Results

In this section, we present several results obtained by using the method described above on simulated and real-world data. We compare different choices of parameters and the effects of the sparsity and the weak divergence-free option as well as the different approximations of H described in Section 6.3.3.

For all examples, a maximum intensity projection (MIP) over the z-axis of the norm of the velocity vector field was calculated. Afterwards, a colour direction MIP was created by assigning a RGB value to every pixel of the MIP. This was done by first considering, for every pixel of the MIP, that voxel whose velocity norm value was responsible for the entry of the MIP at that pixel. The absolute values of the \vec{v}_1 , \vec{v}_2 and \vec{v}_3 values of that voxel were then taken as the red, green and blue values of the RGB triplet at that pixel, respectively. This means that a red pixel in the colour direction MIP indicates movement along the x-axis, a green pixel along the y-axis and a blue pixel along the z-axis. Finally, all RGB values were divided by the maximum absolute RGB value of the colour direction MIP and the resulting map was divided by a factor of 0.6 in order to enhance colours.

Simulated Data

In this subsection, we test our algorithm on simulated data. For this purpose, a phantom of size $40 \times 30 \times 30$ was created, featuring several blood vessels, i.e., pipes, of variable thickness and orientation. A projection of this phantom over the z-axis can be seen in Figure 6.3, which not only shows the vessels themselves but also the norm of the velocity vector field (left figure) and the a colour direction MIP of the velocity (right figure) moving through the vessels.

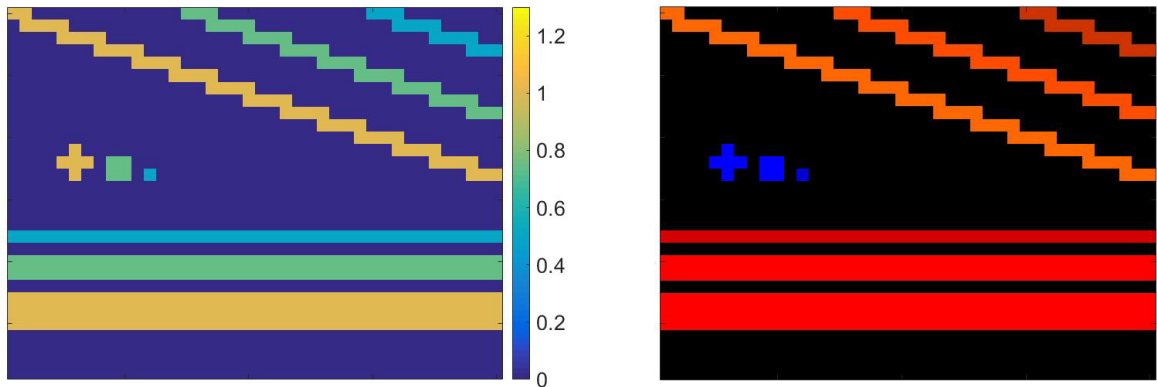


Figure 6.3: Simulation phantom: Magnitude of the norm of the velocity vector field (left figure) and colour direction MIP of the velocity (right figure).

Looking at the colour direction MIP in Figure 6.3, the three red horizontal vessels on the bottom of the phantom move along the x-axis and have a thickness of 1, 2 and

3 voxels, respectively. The three blue vessels above them move along the z -axis, and hence only a small part of them can be seen in the picture. Note that one of those vessels has a plus-shaped cross-section, which is also the case for the bottommost of the three red blood vessels. The three orange-red blood vessels move diagonally across the x - y -plane and have a z -thickness of 1 voxel each. Both the orange and the red vessels lie in the middle of the z -plane, while the blue vessels extend over the entire range of the z -axis.

As for the simulation of the data $\rho_{i,j,k,l}$, consider first the case of a signal $\rho_0(x, y, z)$ transported by a constant velocity field $\bar{v} = (\bar{v}_1, \bar{v}_2, \bar{v}_3)$. It can be easily seen that in this case

$$\rho(x, y, z, t) = \rho_0(x - \bar{v}_1 t, y - \bar{v}_2 t, z - \bar{v}_3 t), \quad (6.62)$$

solves the advection equation with initial guess ρ_0 . If in each vessel we prescribe a constant velocity vector field pointing in one of the two directions of the vessel, then for a given initial signal ρ_0 we can calculate the solution of the advection equation in that vessel by (6.62). Summing up those solutions for all the different vessels and sampling at the correct space-time points then gives us the data $\rho_{i,j,k,l}$. Adding a random data error of fixed magnitude, e.g., 1%, we arrive at the final data used in the simulation.

In our simulation, for a vessel with given velocity \bar{v} , we used the initial signal

$$\rho_0(x, y, z) = \sin \left(\frac{6\pi}{\|\bar{v}\|_2} \left(\frac{\bar{v}_1}{I\Delta x} x + \frac{\bar{v}_2}{J\Delta y} y + \frac{\bar{v}_3}{K\Delta z} z \right) \right). \quad (6.63)$$

To make the simulation procedure a bit clearer, consider the bottommost vessel in Figure 6.3. Prescribing for example the velocity $\bar{v} = (c, 0, 0)$ in that vessel leads to

$$\rho(x, y, z, t) = \sin \left(\frac{6\pi(x - ct)}{I\Delta x} \right), \quad (6.64)$$

and the data $\rho_{i,j,k,l}$, for those (i, j, k) for which (x_i, y_j, z_k) belongs to the vessel under consideration, is then defined by

$$\rho_{i,j,k,l} = \rho(x_i, y_j, z_k, t_{k,l}) = \sin \left(\frac{6\pi(x_i - ct_{k,l})}{I\Delta x} \right). \quad (6.65)$$

We apply the same procedure to all the remaining vessels and set $\rho_{i,j,k,l}$ to 0 whenever (i, j, k) does not correspond to any vessel. Finally, a randomly generated data error of magnitude δ is added.

Note that the velocity vector field v underlying this data simulation is constant in each vessel and hence locally, but not globally, in H^1 . Even though we have derived our solution method from the assumption of a globally H^1 velocity vector field, using

this simulation makes sense, since for real MRI data we also expect nonzero velocities to occur *inside* blood vessels only, which renders the velocity vector field to be reconstructed only locally H^1 as well.

For the results presented below, we have chosen $\Delta x = \Delta y = \Delta z = 1$ mm and, as mentioned above, $I = 39$, $J = 29$, $K = 29$ for the space discretization, as well as $L = 4$. As for the time discretization Δt , note that our forward solver belongs to the class of BTCS (backward in time, central in space) finite difference methods, which are implicit methods requiring no restriction on the time stepsize Δt to achieve stability. However, in order to get good accuracy of the forward solver, Δt should be chosen small enough. Denoting with ΔT the duration of a full measurement circle, i.e., $\Delta T = (K + 1)\Delta t$, it turned out that a suitable bound is given by the CFL-type condition

$$\Delta T \|v\|_2 \lesssim \frac{\Delta x}{10}. \quad (6.66)$$

Using a ΔT significantly greater than this bound was found to introduce large errors in the reconstructed velocity (see Figure 6.13). Hence, for our tests below, we used $\Delta T = 0.1$ s, which by (6.66) allows for velocities with a maximum norm of 1 mm/s.

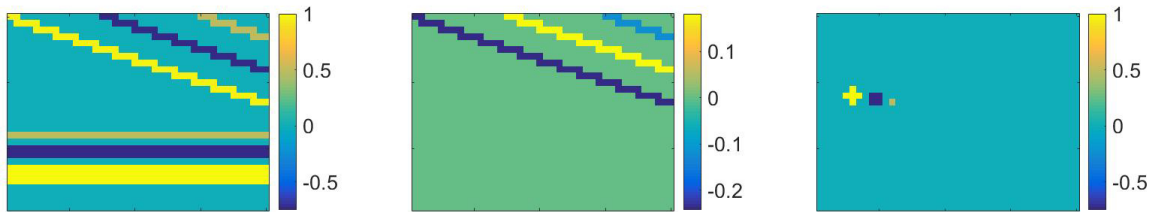


Figure 6.4: Magnitudes of the velocity vector field components. Left: First component. Middle: Second component. Right: Third component.

For our simulations, we have used velocities \bar{v} with three different magnitudes $\|\bar{v}\|_2$, which can be seen in Figure 6.3. The orientation of these velocity vector fields is depicted in more detail in Figure 6.4, which shows the values of the three velocity components, revealing also the different orientations of the simulated pulse waves.

For all tests below, a random data error of magnitude δ was added and the iteration was stopped using the discrepancy principle (2.6) together with the choice of $\tau = 1$. Furthermore, if not noted otherwise, the matrix H introduced in Section 6.3.3 is used instead of the wavelet embedding described in the same section.

As a first test, we use our method without any special options, i.e., neither using the weak divergence-free option, nor the sparsity or the wavelet embedding option. The resulting approximation, achieved after 90 iterations, can be seen in Figure 6.5. The structure of the vessels can clearly be identified and also the reconstructed velocity is

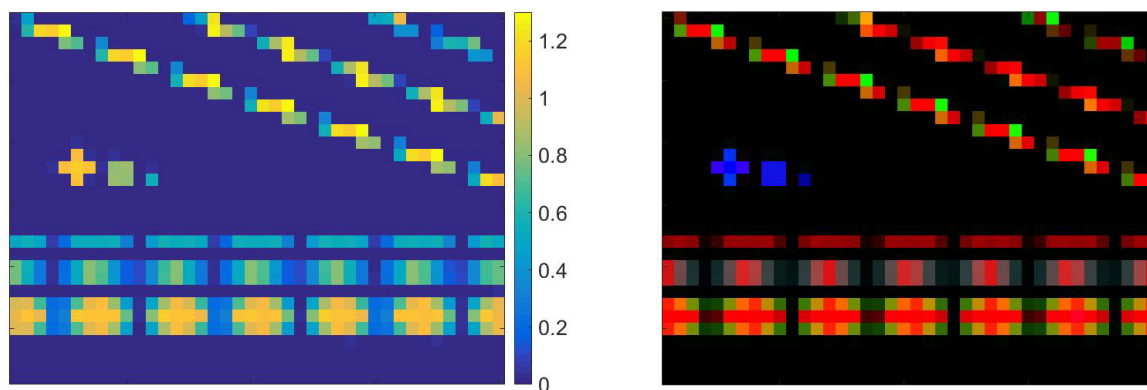


Figure 6.5: Result of the algorithm applied to the test problem ($\delta = 1\%$), using no additional options. Velocity norm MIP (left) and colour direction MIP (right).

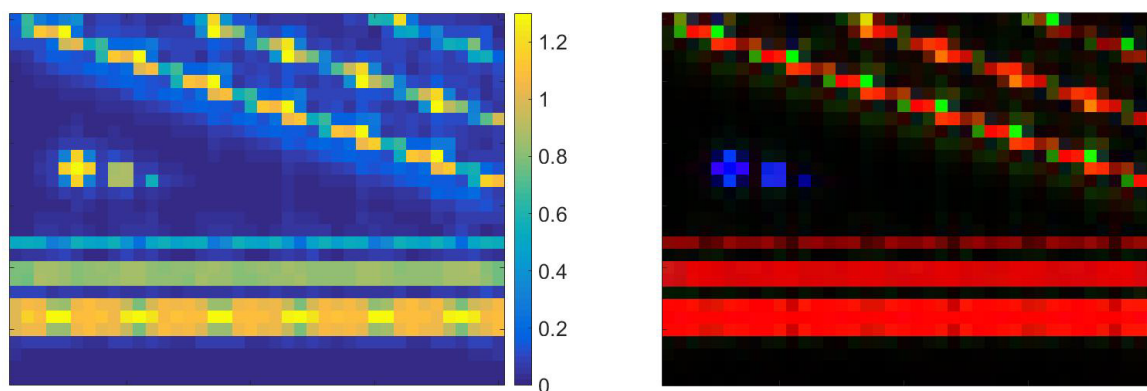


Figure 6.6: Result of the algorithm applied to the test problem ($\delta = 1\%$), using the weak divergence-free option. Velocity norm MIP (left) and colour direction MIP (right).

partially correct. However, the sinusoidal structure of the initial signal ρ_0 is visibly transferred to the reconstructed velocity.

Figure 6.6 shows the results of the second test: the weak-divergence free option was included in the reconstruction algorithm, which now stopped after 126 iterations. The reconstructed velocity is much smoother than before, now resembling the true solution much more closely. However, as could be expected, using the weak divergence-free calculation option leads to a smoothing of the solution, clearly visible in the reconstruction around the vessels.

For the next test, we apply the algorithm together with the wavelet embedding option. The stopping criterion was met after 121 iterations and the results can be seen in Figure 6.7. A comparison with Figure 6.5 shows that using this option mainly leads to a smoothing of the reconstructed velocity, comparable to but not as strong as using the weak divergence-free option.

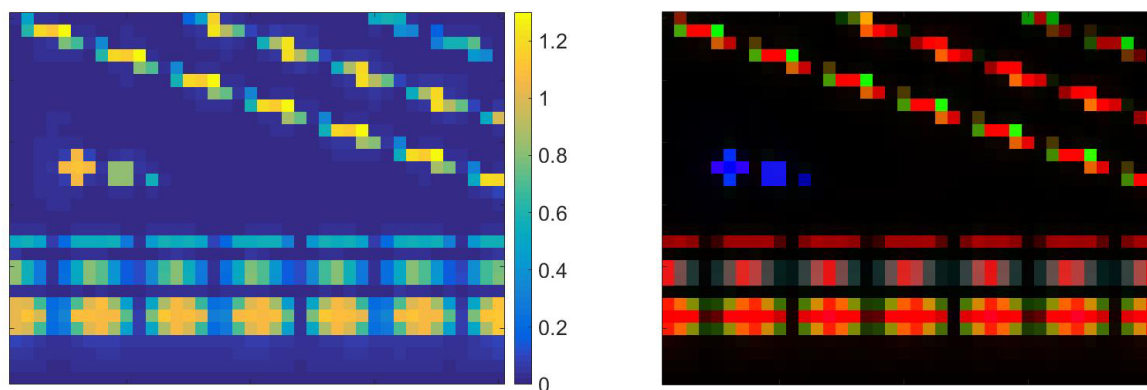


Figure 6.7: Result of the algorithm applied to the test problem ($\delta = 1\%$), using the wavelet embedding option. Velocity norm MIP (left) and colour direction MIP (right).

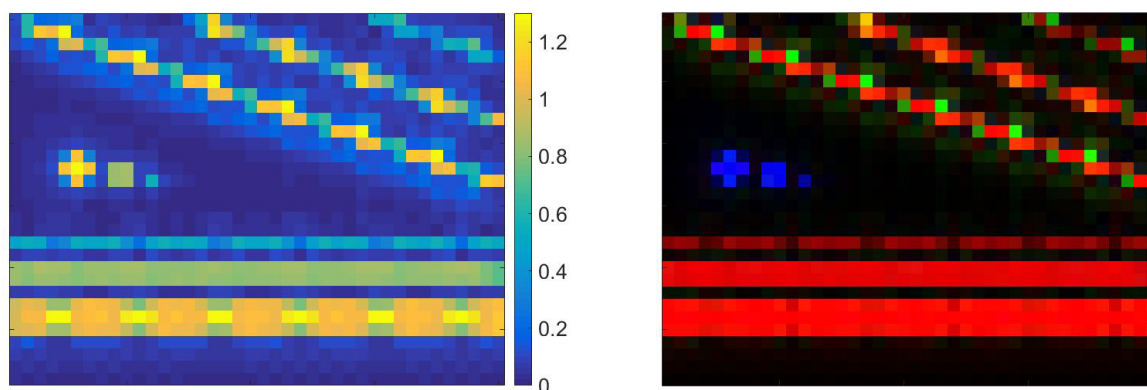


Figure 6.8: Result of the algorithm applied to the test problem ($\delta = 1\%$), using the weak divergence-free and the wavelet embedding option. Velocity norm MIP (left) and colour direction MIP (right).

The results of combining the weak-divergence free and the wavelet embedding options can be seen in Figure 6.8. This time, the iteration terminated after 162 iterations and once again one can see the strong smoothing effects of the two calculation options. As we later see in Table 6.3.5, of all the combinations of different reconstruction options, this one yields the third best result.

Next, we present some results of using the sparsity option, together with either the divergence-free or the wavelet embedding option. For this, we need to choose an α , see (6.3.4). A good choice turns out to be $\alpha = 10^{-3}$, which was used for computing all presented results. Figures 6.9, 6.10, 6.11 and 6.12 show the results of the different combinations, the iteration stopping after 71, 100, 99 and 138 steps, respectively. Note that all iterations involving the sparsity option were terminated before satisfying the discrepancy principle, since the residual stopped decreasing monotonously but rather started to oscillate around a certain value.

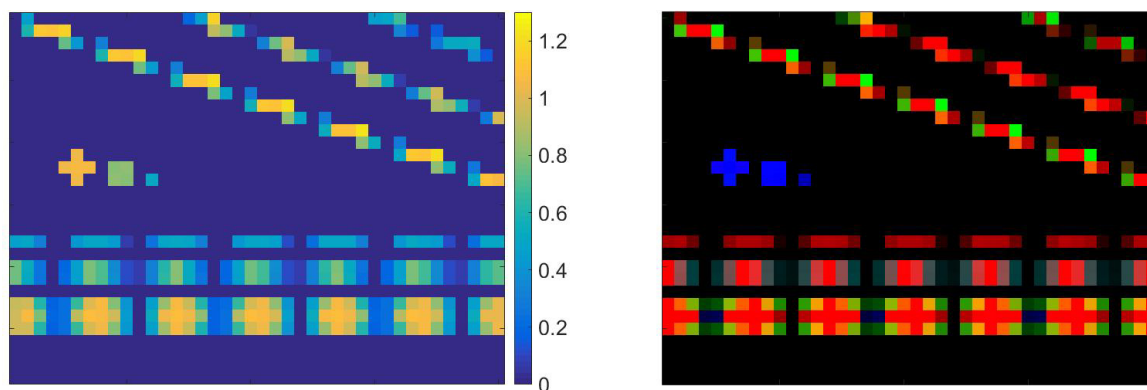


Figure 6.9: Result of the algorithm applied to the test problem ($\delta = 1\%$), using the sparsity option with $\alpha = 10^{-3}$. Velocity norm MIP (left) and colour direction MIP (right).

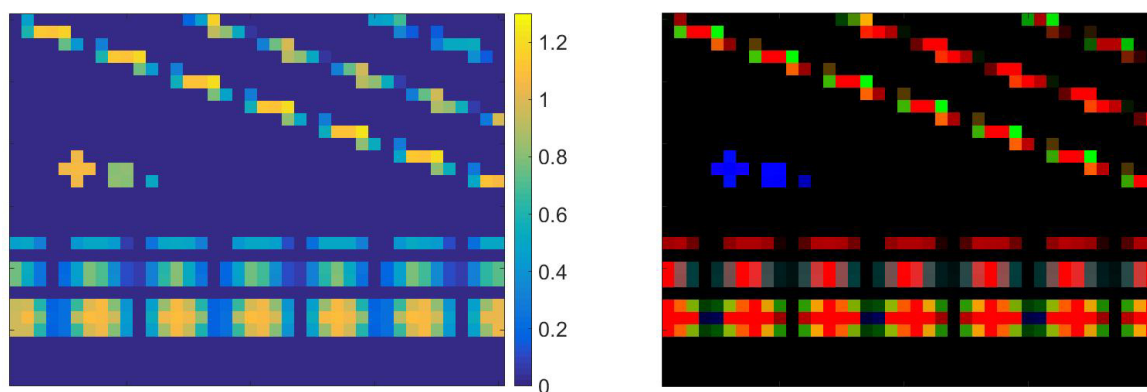


Figure 6.10: Result of the algorithm applied to the test problem ($\delta = 1\%$), using the wavelet embedding and the sparsity option with $\alpha = 10^{-3}$. Velocity norm MIP (left) and colour direction MIP (right).

Comparing Figure 6.7 and Figure 6.10, we see that the edges are now more sharply reconstructed, although the result itself does not look much better than when using no additional options at all. This also holds true for only using the sparsity option alone, see Figure 6.9. However, Figure 6.11 strongly shows the advantages of combining the divergence-free and the sparsity options. The initial signal ρ_0 only slightly affects the reconstructed solution and the sparsity option removes some of the smearing introduced by the divergence-free option, producing very nice results. Even better results are obtained when combining all three calculation options, which can be seen Figure 6.12, most notably at the plus shaped vessel in the centre of the figure and at the diagonal vessels, especially at the middle one of the three, which, despite the crude discretization and the smoothing introduced by the divergence-free and the wavelet embedding option, is reconstructed rather nicely.

In Table 6.3.5 we have collected some important information about the results pre-

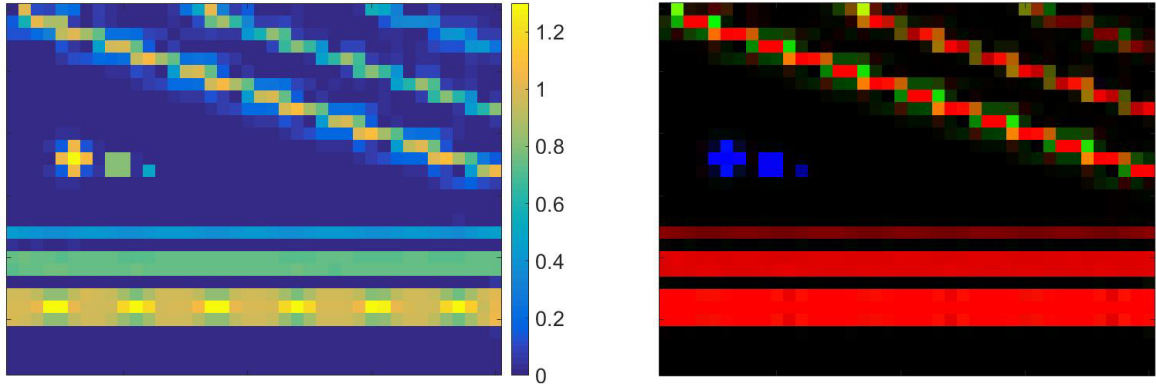


Figure 6.11: Result of the algorithm applied to the test problem ($\delta = 1\%$), using the weak divergence-free and the sparsity option with $\alpha = 10^{-3}$. Velocity norm MIP and colour direction MIP.

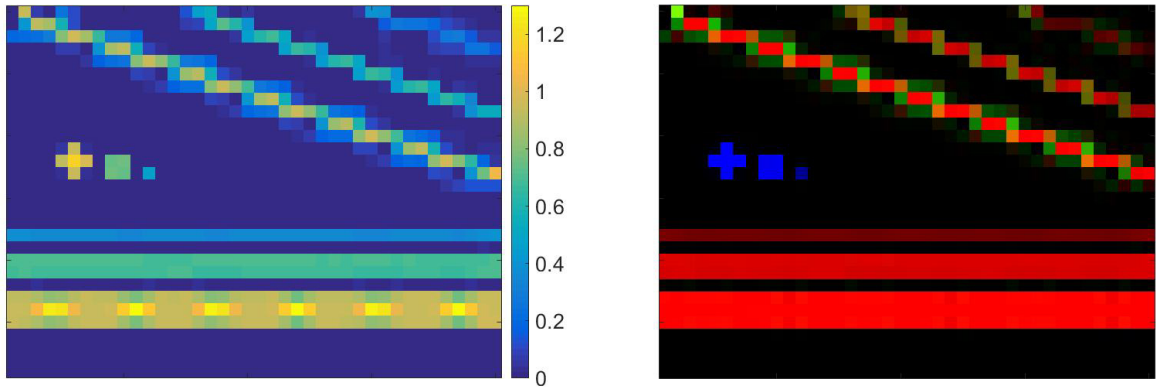


Figure 6.12: Result of the algorithm applied to the test problem ($\delta = 1\%$), using the weak divergence-free, the wavelet embedding and the sparsity option with $\alpha = 10^{-3}$. Velocity norm MIP and colour direction MIP.

sented above. The first three columns contain information about the used calculation options, the fourth column contains the iteration index k_* at which the algorithm was terminated and in the fifth column, the error between approximated and true solution (denoted by $(\vec{v}^\dagger, \vec{\rho}_0^\dagger)$) is given. Here we have used the standard Euclidean ℓ_2 -norm for measuring the error, in order to allow for a fair comparison between those results which were achieved using the wavelet embedding option and the ones not using it. Once again it can be seen that the best results are obtained using all three calculation options in the reconstruction algorithm.

For our next test in this section, we adapt the simulation parameters to better fit the natural stimulation data set considered below, i.e., we use the same simulation phantom as before but now with spatiotemporal resolution $\Delta x = \Delta y = \Delta z = 1.4$ mm and $\Delta t = 0.0417$ s (i.e., $\Delta T = 1.25$ s; note the difference in size between phantom and natural stimulation data set) together with $L = 9$. Furthermore, since the PWV

	div-free	wavelets	sparsity	k_*	$\ (\vec{v}_{k_*}^\delta, \vec{\rho}_{0,k_*}^\delta) - (\vec{v}_0^\dagger, \vec{\rho}_0^\dagger)\ _{\ell_2}$
Figure 6.5	no	no	no	90	16.9658
Figure 6.6	yes	no	no	126	9.2904
Figure 6.7	no	yes	no	121	16.4324
Figure 6.8	yes	yes	no	162	8.8878
Figure 6.9	no	no	yes	71	17.179
Figure 6.10	no	yes	yes	100	16.7834
Figure 6.11	yes	no	yes	99	5.6577
Figure 6.12	yes	yes	yes	138	5.5245

Table 6.3: Comparison of the results of the reconstruction algorithm applied to the test problem ($\delta = 1\%$), achieved using combinations of the different computation options.

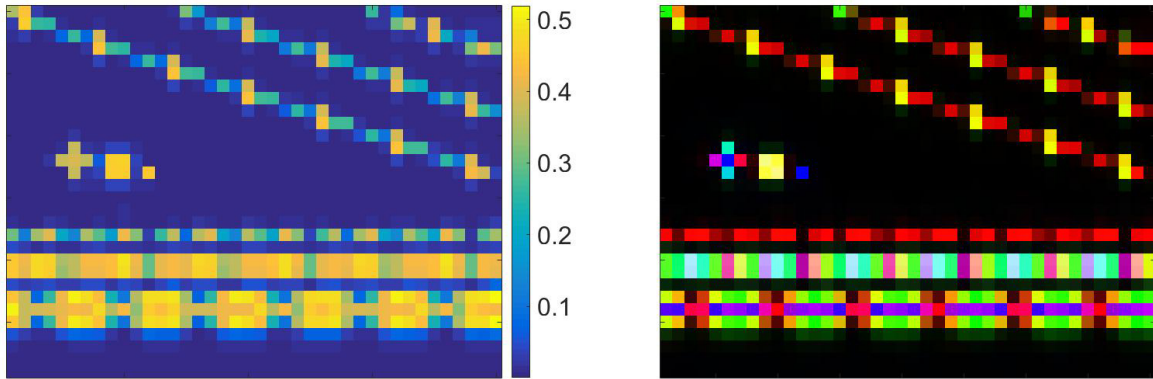


Figure 6.13: Result of the algorithm applied to the modified problem ($\delta = 1\%$), where all involved velocities were multiplied by a factor of 10^4 , using the weak divergence-free, the wavelet embedding and the sparsity option with $\alpha = 10^{-3}$. Velocity norm MIP (left) and colour direction MIP (right).

can reach up to 10 m/s, we multiply the velocities in all the vessels with a factor of 10^4 to simulate this fact. It is obvious that with those choices, condition (6.66) is far from being satisfied and hence, one can no longer expect to achieve similarly good results as before. The reconstructions computed with our algorithm using all three computation options can be seen in Figure 6.13, the iteration having stopped after 7 iterations due to a detected increase of the residual. One can clearly see that as a result of (6.66) not being satisfied, the velocities are strongly underestimated, which, even if one were to ignore the increase in residual and continue the iteration, could not be overcome. The problems related to high pulse velocities or large wavelengths, as well as the artefacts arising from them, can only be overcome by improved data acquisition techniques and have been discussed previously [79, 80]. However, the algorithm is still able to detect the location of the vessels as well as some small qualitative differences in the norm of the velocity vector field. Furthermore, it is also still able to extract some

information about the directions of the PWV, especially for vessels with a thickness of one voxel. Due to the high velocities in this simulation, in vessels thicker than one voxel neighbouring voxels perpendicular to the flow direction influence each other strongly, which leads to a somewhat distorted velocity vector field reconstruction in them.

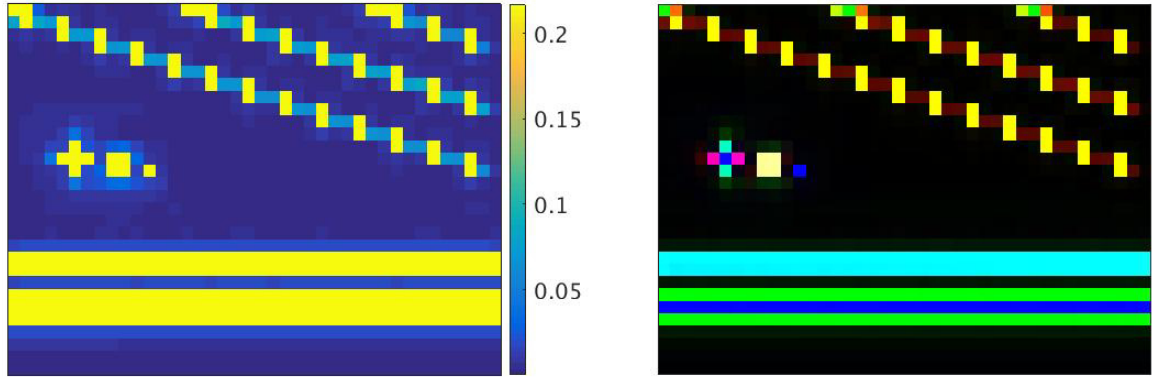


Figure 6.14: Result of the algorithm applied to the modified problem ($\delta = 1\%$), where all involved velocities were multiplied by a factor of 10^4 with initial signal (6.67), using the weak divergence-free and the wavelet embedding option. Velocity norm MIP (left) and colour direction MIP (right).

In the above examples, the initial signal ρ_0 defined by (6.63) was used to create the data. As can be seen from (6.64), this choice leads to a signal with a wavelength independent of the PWV. However, in the real world data set examined below one expects the wavelength to increase with the PWV, the signal having a pulse around 1 Hertz and a wavelength between 1 to 10 meters. In order to simulate this behaviour, we adapt our initial signal as follows:

$$\rho_0(x, y, z) = \sin\left(\frac{2\pi(x + y + z)}{\|\bar{v}\|_2}\right). \quad (6.67)$$

Prescribing for example the unidirectional velocity $\bar{v} = (c, 0, 0)$ as in (6.64), we now get

$$\rho(x, y, z, t) = \sin\left(\frac{2\pi(x - ct)}{c}\right), \quad (6.68)$$

from which we see that the wavelength of the signal now depends on the PWV in the desired way. Using the same phantom as in the previous test but with PWVs up to 10 m/s, the reconstruction algorithm using the weak divergence-free and the wavelet embedding options produces the results depicted in Figure 6.14. The calculation stopped after 6 iterations due to a detected increase of the residual. As expected, the periodic modulation in the horizontal vessel visible in some of the previous results disappears, but also the direction estimate in the same region becomes inaccurate; the

thinnest vessel disappears and the horizontal vessel direction is not visible anymore. These results might show the limits of our simplified phantom simulations but also should be considered as possible artefacts in interpreting real-world data, which is studied next.

Natural Stimulation Data Set

In this subsection, we test the applicability of our algorithm to real-world data sets. For this, we use a publicly available natural stimulation dynamic EPI data set obtained on a 7.0 T MRI scanner [31]. Subjects were listening to an audio version of a movie. The data set includes eight 15 minutes long segments for each subject, of which the first 20 seconds of the second one were used for analysis. The transversal slices covered most of the frontal and occipital cortex and the regions in between. Data was sampled with a pulse repetition time (TR) of 2 s and an isotropic spatial resolution of 1.4 mm. The data set also contains time-of-flight angiography images of about the same coverage as the EPI data, as well as pulse oximetry data.

We want to apply our algorithm to different subjects of this data set, for which Voss et al. have already tried to reconstruct the pulse wave velocity using their multiple regression approach [80]. In order to do so, we need to adapt our stopping rule, since the discrepancy principle defined in (2.6) relies essentially on knowledge of δ , which, as is usually the case in real-world situations, is not given explicitly. However, an estimate of the data error can be made by looking at the background voxels, i.e., those voxels which are known to lie outside the brain and which therefore should have value 0 if no noise were present. The corresponding calculations suggest that for our data set, the relative data error is approximately 2 - 3 %. This estimate, combined with the discrepancy principle and a check for monotonous decrease of the residual suggests to stop the iteration after 15 - 25 iterations.

The upper two figures of Figure 6.15 show the results of applying our algorithm with the above described changes to subject 16 of the real world data set. Here we used the divergence free, the wavelet embedding and the sparsity option, this time with $\alpha = 10^4$ and the computation was stopped after 20 iterations. As before, the upper left image shows the velocity norm MIP over the z-axis and the upper right image the colour direction MIP of the reconstructed velocity \vec{v} . One can clearly see the location of the major blood vessels and arteries, as well as their orientation, even though the expected PWV is severely underestimated (see below). The norm of the velocity vector field has maximum 0.1495, mean $\mu = 0.0011$ and standard deviation $\sigma = 0.0034$. In order to generate the figure, a slight scaling was introduced, cutting all values in the MIP which are above $\mu + 5\sigma$. The colour direction MIP was slightly brightened in order to enhance visibility.

For comparison of our proposed and the previously used method, the lower two figures of Figure 6.15 depict the results of the multiple regression approach, applied to the

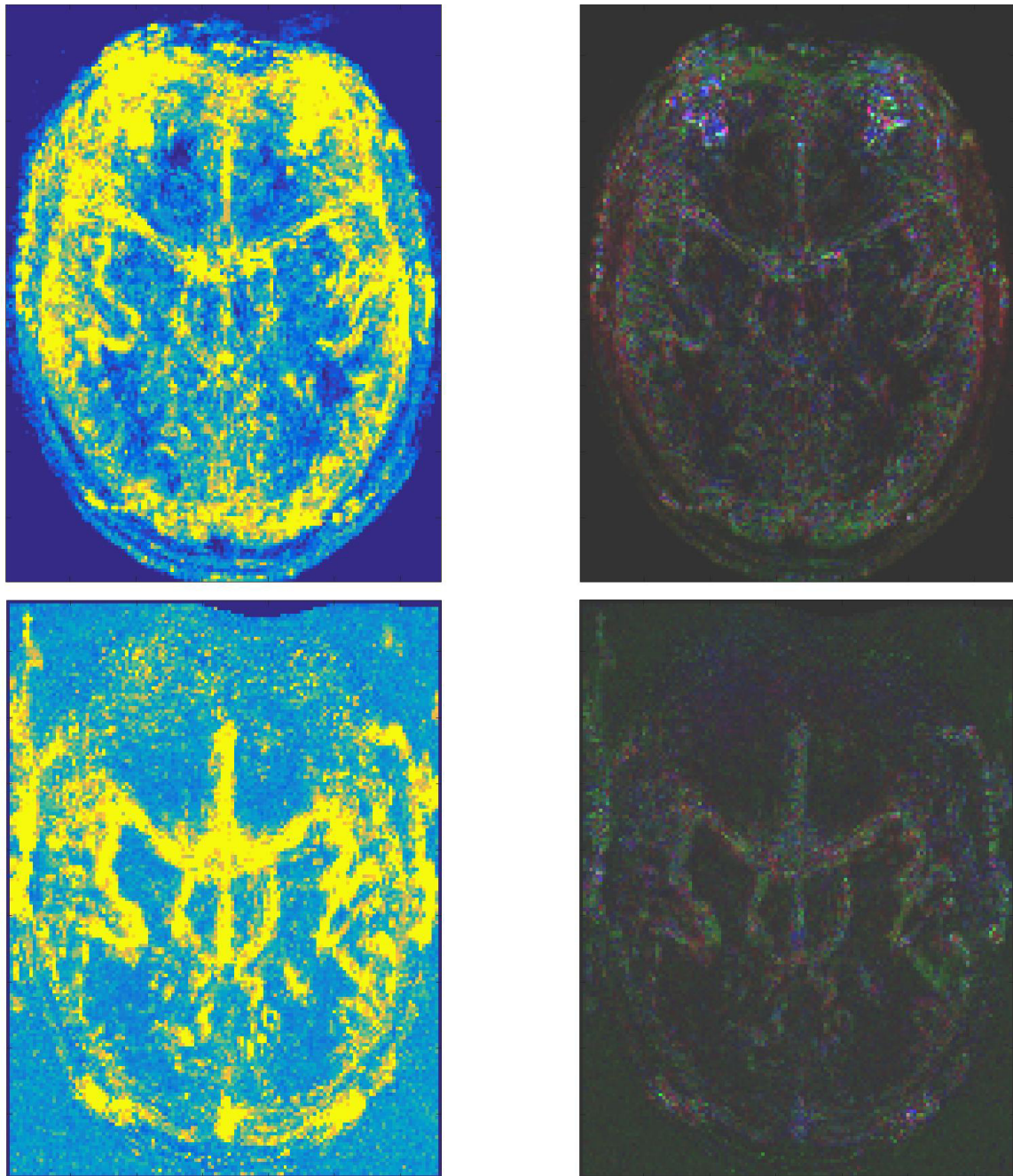


Figure 6.15: Results of our proposed algorithm (upper two figures, 20 seconds of data) and the regression-based algorithm (lower two figures, 15 minutes of data), applied to subject 16 of the data set. Velocity norm MIPs (left) and colour direction MIPs (right).

same subject 16 of the data set, using a 0.05 Hz cut-off filtering preprocessing step and all 15 minutes of the second segment of the data set. Again, a $\mu + 5\sigma$ scaling

and a slight brightening of the colour direction MIP were used for better visibility. One can see that while the previously used algorithm mainly yields estimates of the PWV in the main arteries and blood vessels, our new algorithm is able to resolve finer structures as well, using only a fraction of the data. Note that the previously used algorithm applied to 20 seconds of data would yield a result hardly distinguishable from white noise.

For certain subjects of the data set, the regression approach of [80] yields very unsatisfactory results. This appears to be due to the heart rate of the subjects having an unfavourable frequency and the data error being higher in those cases. The results of the regression approach and our proposed algorithm applied to one of those subjects, subject 2 of the data set, can be seen in Figure 6.16. The differences are quite obvious and can be attributed to two main reasons. Firstly, our algorithm works with much less data than the regression approach and secondly, by stopping the iteration after a certain amount of steps, we get a regularizing effect. Consequently, the effects of data error can partly be compensated and therefore, better reconstructions are obtained.

Please also note, that the calculated velocities using the real-world data set, which are around 10^{-5} m/s, differ by orders of magnitude from the expected pulse wave velocity, which can exceed 10 m/s. One reason for this is the high amount of noise in the data, which can only be partially controlled using appropriate filters. Another reason is the low spatiotemporal, in particular the low temporal resolution of the MRI data; condition (6.66) is far from being fulfilled and hence the algorithm, after a certain amount of iterations, is no longer able to improve the approximation, which leads to underestimated velocities. The same problem has already been observed in [79], where the velocities were severely underestimated as well. This phenomenon, although most clearly understandable from the point of view of the finite difference approximation and condition (6.66), is also quite likely to appear, in one or another form, when using other discretization techniques as well.

6.3.6 Discussion of Results

The advection model was intended to model travelling pulse waves, but there might be other travelling disturbances along blood vessels or nerves in the brain. For example, it has been observed that endothelially mediated vasodilation related to functional brain activation travels along small blood vessels [34]. High-resolution dynamic MRI data that would be potentially able to resolve this phenomenon with MRAI already exists [85], although on spatial scales much smaller than used here. Furthermore, due to its sensitivity to pulsatile components of the signal and due to dramatic advances in dynamic MRI data acquisition [54], MRAI might have future potential to contribute to the modelling of the cerebrovascular system and to serve as a biomarker for cerebrovascular disease. It should also be noted that the methods described herein are quite general and could in principle be applied to spatiotemporal dynamics across

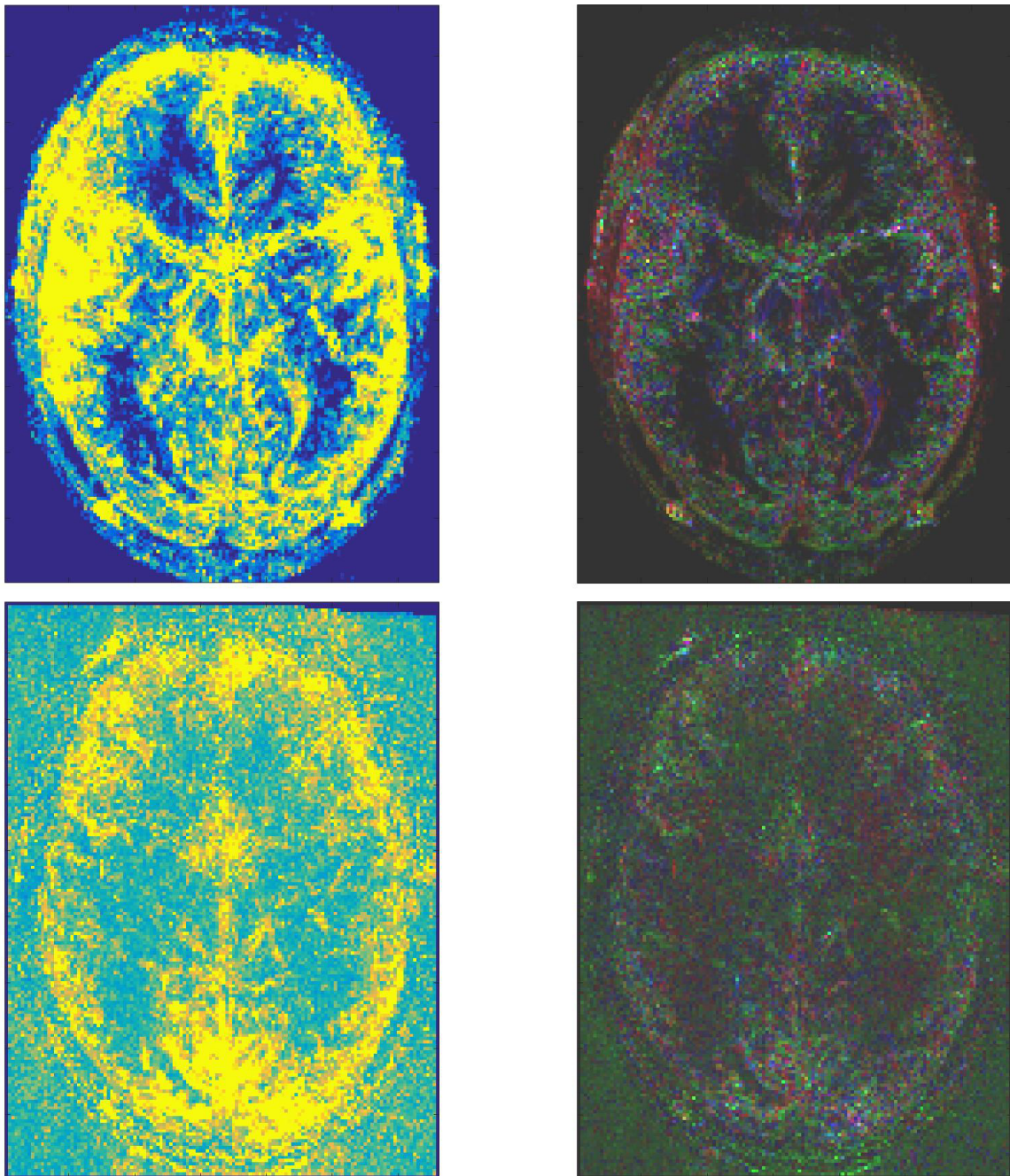


Figure 6.16: Results of our proposed algorithm (upper two figures, 20 seconds of data) and the regression-based algorithm (lower two figures, 15 minutes of data), applied to subject 2 of the data set. Velocity norm MIPs (left) and colour direction MIPs (right).

a wide range of dynamic imaging applications in medicine and other fields (with an adaptation of the PDE model to the specific situation).

Concerning our proposed velocity estimation algorithm, the numerical simulation re-

sults of Section 6.3.5 clearly demonstrate the good reconstruction abilities of our method, especially when used with a suitable combination of the currently available options (weak divergence-free, sparsity, wavelets). This points to an advantage over the regression approach of Voss et al. [80], namely the high flexibility of our approach. Considering the parameter estimation problem of MRAI in the framework of inverse problems, a vast array of techniques becomes available, leading to improved results. While the regression based method is more or less inflexible, our proposed approach can easily be adapted to include different or newly developed reconstruction options.

Another advantage of our algorithm is its ability to produce appealing results with only a small amount of data. Where the multiple regression approach requires at least a couple of minutes of measurements, our algorithm, as we have seen in Section 6.3.5, can produce nice qualitative results from only a couple of seconds of measurements. This might prove advantageous in practice, where long scan times often need to be avoided.

Although working on numerical phantom simulations, when applied to the real-world data sets, both the regression based approach and our proposed reconstruction method produce qualitative results only. As mentioned above, the most important reasons for this are the high amount of data error and the low spatiotemporal resolution of the data when compared to the expected magnitude of the PWV. Hence, in order to achieve better results, MRI data with higher resolutions and less noise need to be used in our algorithm. One possible way towards this would be to use advanced imaging methods such as multiband EPI [54], where a whole stack of slices is acquired in a time that normally allows only for the acquisition of a single slice, which leads to a much higher spatiotemporal resolution.

6.4 Further Examples

In this section, we want to comment on further examples in which TPG methods or variants thereof have been successfully employed to solve ill-posed problems.

Perhaps the first time Nesterov's accelerated gradient method was used methodically within the area of Inverse Problems is the *Fast Iterative Shrinkage-Thresholding Algorithm (FISTA)* [7]. There, it is used to solve linear inverse problems with sparsity constraints. More precisely, given a matrix $A \in \mathbb{R}^{m \times n}$ and data $b \in \mathbb{R}^m$, the minimization problem of Tikhonov type

$$\min_x \|Ax - b\|_2^2 + \lambda \|x\|_1, \quad (6.69)$$

is solved using the algorithm

$$\begin{aligned} z_k &= x_k + \frac{k-1}{k+2}(x_k - x_{k-1}), \\ x_{k+1} &= \mathcal{S}_{\lambda t} \left(z_k - 2tA^T(Az_k - b) \right), \end{aligned}$$

where t is a stepsize and $\mathcal{S}_\alpha : \mathbb{R}^n \rightarrow \mathbb{R}^n$ is the shrinkage operator defined by

$$\mathcal{S}_\alpha(x)_i = (|x_i| - \alpha)_+ \operatorname{sgn}(x_i).$$

Note that this is just Nesterov's acceleration scheme in its extended version (2.19), applied to the minimization problem (6.69).

As noted in Chapter 2, the use of the TPG method (2.22) as a regularization method for linear ill-posed problems was first investigated by Neubauer in [61]. In this paper, the author presents examples based on a Fredholm integral equation of the first kind.

Possibly the first application of a TPG method of the form (2.22) to nonlinear ill-posed problems was given in [44], where the author uses a variant of (2.22) in Banach spaces to speed up a Landweber-Kaczmarz method with inexact inner solvers. In both a numerical example concerning the estimation of the parameter c in

$$-\Delta u + cu = f, \quad \text{in } \Omega, \quad (6.70)$$

$$u = g, \quad \text{on } \partial\Omega, \quad (6.71)$$

from measurements of u and an example from computed tomography, the idea of (2.22) was used to speed up the employed iterative procedure.

Finally, the TPG method (2.22) was recently used in [40, 75] to solve an inverse problem of *quantitative elastography with internal measurements*, namely the estimation of the spatially varying Lamé parameters (λ, μ) from displacement field measurements u induced by external forces. The underlying model connecting these quantities are the equations of linearized elasticity

$$\begin{aligned} -\operatorname{div}(\sigma(u)) &= f, & \text{in } \Omega, \\ u|_{\Gamma_D} &= g_D, \\ \sigma(u)\vec{n}|_{\Gamma_T} &= g_T, \end{aligned} \quad (6.72)$$

where \vec{n} is an outward unit normal vector of $\partial\Omega$ and the stress tensor σ defining the stress-strain relation in Ω is defined by

$$\sigma(u) := \lambda \operatorname{div}(u) I + 2\mu \mathcal{E}(u), \quad \mathcal{E}(u) := \frac{1}{2} (\nabla u + \nabla u^T), \quad (6.73)$$

where I is the identity matrix and \mathcal{E} is called the strain tensor. This problem was formulated as a nonlinear operator equation and the strong tangential cone condition (2.7) was proven for the (realistic) case that λ, μ are known in a neighbourhood of the boundary. Afterwards, the TPG method (2.22) was used to obtain various numerical reconstructions on both simulated and experimental data.

Chapter 7

Conclusion and Outlook

In this chapter, we summarize the contributions of this thesis and present a short outlook with possible future work in connection with the presented results.

7.1 Conclusion

In the first part of this thesis, we considered general TPG methods of the form (2.23) as regularization methods for nonlinear ill-posed problems in Hilbert spaces. It was shown that under the standard assumption of a tangential cone condition and combined with a suitable stopping rule, many TPG methods give rise to convergent regularization methods. In particular, this includes TPG methods based on constant stepsizes as well as the steepest descent and the minimal error stepsize. Additionally, different choices for the combination parameters λ_k^δ were investigated and proven to lead to convergent regularization methods. Furthermore, a TPG method based on the original choice for λ_k^δ of Nesterov's accelerated gradient method was investigated and convergence was shown under a local convexity assumption on the residual functional.

In the second part of this thesis, we considered various numerical examples in which TPG methods were applied to both academic and practically relevant problems. The academic examples based on a nonlinear Hammerstein operator and a diagonal operator served to show that the assumptions required for the convergence analysis can indeed be satisfied for particular problems, and the presented numerical results are clearly in favour of TPG methods compared to other gradient-based methods. This motivated us to look at more practical problems based on SPECT and Auto-Convolution. While the local convexity assumption is satisfied for the Auto-Convolution problem under a sparsity assumption, it is not clear whether this is also true for SPECT. However, also in this case the numerical results clearly illustrate the advantages of TPG methods. Finally, numerical results on the medical imaging technique of MRAI were presented, for which TPG methods are especially important due to the large datasets involved.

Although no analytical results are yet available proving that indeed less iterations are required when using TPG methods (2.23) compared to other first-order methods, these numerical results clearly show their advantages in practise. Besides the fact that much fewer iterations are necessary to arrive at suitable solutions, the implementation of TPG methods is exceedingly simple. Furthermore, they requiring hardly more computation time than their non-accelerated counterparts per iteration step. Due to the numerically demonstrated great reduction of the required number of iterations, TPG methods can serve as a viable alternative to commonly used second-order iterative methods, especially when dealing with large-scale inverse problems, where the latter ones often become impracticable.

7.2 Outlook

Various further directions and extensions of the work presented in this thesis are possible, some of which are listed here:

- First, it would be interesting to find out whether weak convergence of the TPG method based on the original Nesterov choice for λ_k^δ can be proven under the assumption of a tangential cone condition instead of a local convexity assumption and whether the result can be strengthened to strong convergence.
- Secondly, as for other iterative regularization methods, convergence rate results under source conditions or variational inequalities are desirable.
- Thirdly, it would be interesting to see what would happen analytically if sparsity conditions or other projections are built into the TPG methods via the proximal operator and whether or not convergence can still be guaranteed in this case.
- Fourth, the task of finding weaker and more inclusive convergence conditions both for TPG methods and for iterative regularization methods in general is a pressing task for future work.
- Fifth, the improvement of the MRAI technique to obtain quantitative results for example by using different PDE models or using new higher resolution datasets will go a long way to make MRAI a medical imaging technique for the future.
- Sixth and finally, proving a nonlinearity or local convexity condition for SPECT would guarantee local convergence of iterative regularization methods and hence place SPECT on a more sturdy theoretical foundation.

List of Figures

5.1	Activity function f_* (left) and attenuation function μ_* (right).	56
5.2	The generated data $y = A(f_*, 0)$ (left) and $y = A(f_*, \mu_*)$ (right).	56
5.3	Results of using the TPG methods with steepest descent stepsize α_k^{SD} and various choices of λ_k^δ , using a relative data error of 0.25%. Left: Plot of the values of λ_k over the iteration number k . Right: Plot of the residual $\ A(f_k, \mu_k) - y^\delta\ $ over the iteration number k . Dashed red line: $\lambda_k^\delta = \lambda_k^N$, solid blue line: $\lambda_k^\delta = \lambda_k^B$, dash-dotted black line: $\lambda_k^\delta = \lambda_k^E$, solid magenta line in the right sub-figure (extending up to the y-axis value 1500): $\lambda_k^\delta = 0$	59
5.4	Results of the TPG method using the steepest descent stepsize α_k^{SD} together with $\lambda_k^\delta = \lambda_k^B$ for the SPECT example problem with a relative data error of $\delta = 0.25\%$. Activity function f_{k_*} (left) and attenuation function μ_{k_*} (right).	60
6.1	Auto-convolution example: Initial guess x_0 (blue), exact solution x^\dagger (red), Landweber (2.4) reconstruction (purple), Nesterov (4.4) reconstruction (yellow).	68
6.2	Example image of a clinical MRI scanner.	70
6.3	Simulation phantom: Magnitude of the norm of the velocity vector field (left figure) and colour direction MIP of the velocity (right figure).	84
6.4	Magnitudes of the velocity vector field components. Left: First component. Middle: Second component. Right: Third component.	86
6.5	Result of the algorithm applied to the test problem ($\delta = 1\%$), using no additional options. Velocity norm MIP (left) and colour direction MIP (right).	87
6.6	Result of the algorithm applied to the test problem ($\delta = 1\%$), using the weak divergence-free option. Velocity norm MIP (left) and colour direction MIP (right).	87
6.7	Result of the algorithm applied to the test problem ($\delta = 1\%$), using the wavelet embedding option. Velocity norm MIP (left) and colour direction MIP (right).	88
6.8	Result of the algorithm applied to the test problem ($\delta = 1\%$), using the weak divergence-free and the wavelet embedding option. Velocity norm MIP (left) and colour direction MIP (right).	88

6.9	Result of the algorithm applied to the test problem ($\delta = 1\%$), using the sparsity option with $\alpha = 10^{-3}$. Velocity norm MIP (left) and colour direction MIP (right).	89
6.10	Result of the algorithm applied to the test problem ($\delta = 1\%$), using the wavelet embedding and the sparsity option with $\alpha = 10^{-3}$. Velocity norm MIP (left) and colour direction MIP (right).	89
6.11	Result of the algorithm applied to the test problem ($\delta = 1\%$), using the weak divergence-free and the sparsity option with $\alpha = 10^{-3}$. Velocity norm MIP and colour direction MIP.	90
6.12	Result of the algorithm applied to the test problem ($\delta = 1\%$), using the weak divergence-free, the wavelet embedding and the sparsity option with $\alpha = 10^{-3}$. Velocity norm MIP and colour direction MIP.	90
6.13	Result of the algorithm applied to the modified problem ($\delta = 1\%$), where all involved velocities were multiplied by a factor of 10^4 , using the weak divergence-free, the wavelet embedding and the sparsity option with $\alpha = 10^{-3}$. Velocity norm MIP (left) and colour direction MIP (right).	91
6.14	Result of the algorithm applied to the modified problem ($\delta = 1\%$), where all involved velocities were multiplied by a factor of 10^4 with initial signal (6.67), using the weak divergence-free and the wavelet embedding option. Velocity norm MIP (left) and colour direction MIP (right).	92
6.15	Results of our proposed algorithm (upper two figures, 20 seconds of data) and the regression-based algorithm (lower two figures, 15 minutes of data), applied to subject 16 of the data set. Velocity norm MIPs (left) and colour direction MIPs (right).	94
6.16	Results of our proposed algorithm (upper two figures, 20 seconds of data) and the regression-based algorithm (lower two figures, 15 minutes of data), applied to subject 2 of the data set. Velocity norm MIPs (left) and colour direction MIPs (right).	96

List of Tables

5.1	Comparison of different stepsizes α_k^δ and combination parameters λ_k^δ : Number of iterations k_* and total amount of time necessary to satisfy the discrepancy principle. A relative data error of 0.001% was used. . .	54
5.2	Comparison of different stepsizes α_k^δ and combination parameters λ_k^δ : Number of iterations k_* and total amount of time necessary to satisfy the discrepancy principle. A relative data error of 0.25% was used. . .	58
5.3	Comparison of different stepsizes α_k^δ and combination parameters λ_k^δ : Number of iterations k_* and total amount of time necessary to satisfy the discrepancy principle. A relative data error of 0.2% was used. . .	60
6.1	Comparison of Landweber iteration (2.4) and its Nesterov accelerated version (4.4) when applied to the diagonal operator problem considered in Example 6.1.1.	64
6.2	Comparison of Landweber iteration (2.4) and its Nesterov accelerated version (4.4) when applied to the auto-convolution problem considered in Example 6.2.1 for the choice $x^\dagger(s) = 10 + \sqrt{2} \sin(2\pi s)$ and $x_0(s) =$ $10 + \frac{27}{28} \sqrt{2} \sin(2\pi s)$ (left table) and $x^\dagger(s) = 10 + \sqrt{2} \sin(8\pi s)$ and $x_0(s) =$ $10 + \sqrt{2} \sin(2\pi s)$ (right table).	67
6.3	Comparison of the results of the reconstruction algorithm applied to the test problem ($\delta = 1\%$), achieved using combinations of the different computation options.	91

Bibliography

- [1] R. Aaslid. *Transcranial Doppler Sonography*. Springer-Verlag, Wien; New York, 1986.
- [2] S. W. Anzengruber, S. Bürger, B. Hofmann, and G. Steinmeyer. Variational regularization of complex deautoconvolution and phase retrieval in ultrashort laser pulse characterization. *Inverse Problems*, 32(3):035002, 2016.
- [3] H. Attouch and J. Peypouquet. The Rate of Convergence of Nesterov’s Accelerated Forward–Backward Method is Actually Faster Than $o(1/k^2)$. *SIAM Journal on Optimization*, 26(3):1824–1834, 2016.
- [4] G. A. Bateman. Pulse-wave encephalopathy: A comparative study of the hydrodynamics of leukoaraiosis and normal-pressure hydrocephalus. *Neuroradiology*, 44(9):740–8, 2002.
- [5] O. V. Batson. The Vertebral Vein System - Caldwell Lecture, 1956. *American Journal of Roentgenology Radium Therapy and Nuclear Medicine*, 78(2):195–212, 1957.
- [6] H. H. Bauschke and P. L. Combettes. *Convex analysis and monotone operator theory in Hilbert spaces*. Springer, 2017.
- [7] A. Beck and M. Teboulle. A Fast Iterative Shrinkage-Thresholding Algorithm for Linear Inverse Problems. *SIAM J. Imaging Sci.*, 2(1):183–202, 2009.
- [8] S. Birkholz, G. Steinmeyer, S. Koke, D. Gerth, S. Bürger, and B. Hofmann. Phase retrieval via regularization in self-diffraction-based spectral interferometry. *J. Opt. Soc. Am. B*, 32(5):983–992, 2015.
- [9] B. Blaschke, A. Neubauer, and O. Scherzer. On convergence rates for the Iteratively regularized Gauss-Newton method. *IMA Journal of Numerical Analysis*, 17(3):421, 1997.
- [10] S. Bürger, J. Flemming, and B. Hofmann. On complex-valued deautoconvolution of compactly supported functions with sparse Fourier representation. *Inverse Problems*, 32(10):104006, 2016.

- [11] S. Bürger and B. Hofmann. About a deficit in low-order convergence rates on the example of autoconvolution. *Applicable Analysis*, 94(3):477–493, 2015.
- [12] M. S. Dagli, J. E. Ingeholm, and J. V. Haxby. Localization of cardiac-induced signal change in fMRI. *NeuroImage*, 9(4):407–415, 1999.
- [13] I. Daubechies. *Ten Lectures on Wavelets*. Society for Industrial and Applied Mathematics, 1992.
- [14] I. Daubechies, M. Defrise, and C. De Mol. An iterative thresholding algorithm for linear inverse problems with a sparsity constraint. *Communications on Pure and Applied Mathematics*, 57(11):1413–1457, 2004.
- [15] V. Dicken. *Simultaneous activity and attenuation reconstruction in single photon emission computed tomography, a nonlinear ill-posed problem*. PhD thesis, Universität Potsdam, 1998.
- [16] V. Dicken. A new approach towards simultaneous activity and attenuation reconstruction in emission tomography. *Inverse Problems*, 15(4):931, 1999.
- [17] R. J. DiPerna and P. L. Lions. Ordinary differential equations, transport theory and Sobolev spaces. *Invent. Math.*, 98(3):511–547, 1989.
- [18] W. A. Edelstein, G. H. Glover, C. J. Hardy, and R. W. Redington. The intrinsic signal-to-noise ratio in NMR imaging. *Magnetic Resonance in Medicine*, 3(4):604–618, 1986.
- [19] P. Elter. *Methoden und Systeme zur nichtinvasiven, kontinuierlichen und belastungsfreien Blutdruckmessung*. Thesis, Karlsruher Institut für Technologie, 2001.
- [20] S. Engblom and D. Lukarski. FSPARSE. <http://user.it.uu.se/~stefane/freeware.html>, 2014.
- [21] H. W. Engl, M. Hanke, and A. Neubauer. *Regularization of inverse problems*. Dordrecht: Kluwer Academic Publishers, 1996.
- [22] M. C. Henry Feugeas, G. De Marco, I. I. Peretti, S. Godon-Hardy, D. Fredy, and E. S. Claeys. Age-related cerebral white matter changes and pulse-wave encephalopathy: observations with three-dimensional MRI. *Magnetic Resonance Imaging*, 23(9):929–37, 2005.
- [23] G. Fleischer and B. Hofmann. On inversion rates for the autoconvolution equation. *Inverse Problems*, 12(4):419, 1996.
- [24] A. Frydrychowicz, C. J. Francois, and P. A. Turski. Four-dimensional phase contrast magnetic resonance angiography: Potential clinical applications. *European Journal of Radiology*, 80(1):24–35, 2011.

- [25] D. Gerth, B. Hofmann, S. Birkholz, S. Koke, and G. Steinmeyer. Regularization of an autoconvolution problem in ultrashort laser pulse characterization. *Inverse Problems in Science and Engineering*, 22(2):245–266, 2014.
- [26] S. F. Gilyazov and N.L. Gol’dman. *Regularization of Ill-Posed Problems by Iteration Methods*. Mathematics and Its Applications. Springer Netherlands, 2013.
- [27] R. Gorenflo and B. Hofmann. On autoconvolution and regularization. *Inverse Problems*, 10(2):353, 1994.
- [28] J. Hadamard. Sur les problèmes aux dérivés partielles et leur signification physique. *Princeton University Bulletin*, 13:49–52, 1902.
- [29] M. Hanke. Accelerated landweber iterations for the solution of ill-posed equations. *Numerische Mathematik*, 60(1):341–373, 1991.
- [30] M. Hanke. A regularizing Levenberg - Marquardt scheme, with applications to inverse groundwater filtration problems. *Inverse Problems*, 13(1):79, 1997.
- [31] M. Hanke, F. J. Baumgartner, P. Ibe, F. R. Kaule, S. Pollmann, O. Speck, W. Zinke, and J. Stadler. A high-resolution 7-Tesla fMRI dataset from complex natural stimulation with an audio movie. *Scientific Data*, 1:140003:1–18, 2014.
- [32] M. Hanke, A. Neubauer, and O. Scherzer. A convergence analysis of the Landweber iteration for nonlinear ill-posed problems. *Numerische Mathematik*, 72(1):21–37, 1995.
- [33] L. H. G. Henskens, A. A. Kroon, R. J. van Oostenbrugge, E. H. B. M. Gronenschild, M. M. J. J. Fuss-Lejeune, P. A. M. Hofman, J. Lodder, and P. W. de Leeuw. Increased aortic pulse wave velocity is associated with silent cerebral small-vessel disease in hypertensive patients. *Hypertension*, 52(6):1120–U72, 2008.
- [34] E. M. C. Hillman. Coupling mechanism and significance of the BOLD Signal: A status report. *Annual Review of Neuroscience*, 37:161–181, 2014.
- [35] B. Hofmann. Approximate source conditions in Tikhonov-Phillips regularization and consequences for inverse problems with multiplication operators. *Mathematical Methods in the Applied Sciences*, 29(3):351–371, 2006.
- [36] B. Hofmann and O. Scherzer. Local ill-posedness and source conditions of operator equations in hilbert spaces. *Inverse Problems*, 14(5):1189, 1998.
- [37] S. Hubmer, A. Neubauer, R. Ramlau, and H. U. Voss. On the parameter estimation problem of magnetic resonance advection imaging. *Inverse Problems and Imaging*, 12(1):175–204, 2018.

- [38] S. Hubmer and R. Ramlau. Convergence analysis of a two-point gradient method for nonlinear ill-posed problems. *Inverse Problems*, 33(9):095004, 2017.
- [39] S. Hubmer and R. Ramlau. Nesterov's Accelerated Gradient Method for Nonlinear Ill-Posed Problems with a Locally Convex Residual Functional. 2018. Submitted, available from <https://arxiv.org/abs/1803.01757>.
- [40] S. Hubmer, E. Sherina, A. Neubauer, and O. Scherzer. Lamé Parameter Estimation from Static Displacement Field Measurements in the Framework of Nonlinear Inverse Problems. *SIAM Journal on Imaging Sciences*, 2018. Accepted.
- [41] V. Isakov. *Inverse Problems for Partial Differential Equations*. Applied Mathematical Sciences. Springer, New York, NY, 2006.
- [42] J. A. Terry and B. M. W. Tsui and J. R. Hendricks and G. T. Gullberg. The design of a mathematical phantom of the upper human torso for use in 3D SPECT imaging research. *Proc. 1990 Fall Mtg of the Biomedical Engineering Society (Blacksburg, VA)*, pages 1467–74, 1990.
- [43] Q. Jin. On a regularized Levenberg–Marquardt method for solving nonlinear inverse problems. *Numerische Mathematik*, 115(2):229–259, 2010.
- [44] Q. Jin. Landweber-Kaczmarz method in Banach spaces with inexact inner solvers. *Inverse Problems*, 32(10):104005, 2016.
- [45] Q. Jin and U. Tautenhahn. On the discrepancy principle for some Newton type methods for solving nonlinear inverse problems. *Numerische Mathematik*, 111(4):509–558, 2009.
- [46] B. Kaltenbacher, A. Neubauer, and O. Scherzer. *Iterative regularization methods for nonlinear ill-posed problems*. Berlin: de Gruyter, 2008.
- [47] S. Kindermann. Convergence of the gradient method for ill-posed problems. *Inverse Problems and Imaging*, 11(4):703–720, 2017.
- [48] M. V. Klivanov. Inverse problems and Carleman estimates. *Inverse Problems*, 8(4):575, 1992.
- [49] D. J. Korteweg. Über die fortpflanzungsgeschwindigkeit des schalles in elastischen röhren. *Annalen der Physik*, 241(12):525–542, 1878.
- [50] S. Laurent, J. Cockcroft, L. Van Bortel, P. Boutouyrie, C. Giannattasio, D. Hayoz, B. Pannier, C. Vlachopoulos, I. Wilkinson, H. Struijker-Boudier, and European Network Non-invasive. Expert consensus document on arterial stiffness: Methodological issues and clinical applications. *European Heart Journal*, 27(21):2588–2605, 2006.

- [51] J. K. J. Li. *Dynamics of the Vascular System*. Series on Bioengineering and Biomedical Engineering. World Scientific, River Edge, N.J., 2004.
- [52] D. A. Lorenz, P. Maass, and P. Q. Muoi. Gradient descent for Tikhonov functionals with sparsity constraints: theory and numerical comparison of step size rules. *Electron. Trans. Numer. Anal.*, 39:437–463, 2012.
- [53] A. K. Louis. *Inverse und schlecht gestellte Probleme*. Teubner Studienbücher Mathematik. Vieweg+Teubner Verlag, 1989.
- [54] S. Moeller, E. Yacoub, C. A. Olman, E. Auerbach, J. Strupp, N. Harel, and K. Ugurbil. Multiband multislice GE-EPI at 7 Tesla, with 16-fold acceleration using partial parallel imaging with application to high spatial and temporal whole-brain fMRI. *Magnetic Resonance in Medicine*, 63(5):1144–1153, 2010.
- [55] A. I. Moens. *Over de voortplantingssnelheid van den pols [On the speed of propagation of the pulse]*. PhD thesis, University of Leiden, Leiden, The Netherlands, 1877.
- [56] F. Natterer. *The Mathematics of Computerized Tomography*. Society for Industrial and Applied Mathematics, 2001.
- [57] Y. Nesterov. A method of solving a convex programming problem with convergence rate $O(1/k^2)$. *Soviet Mathematics Doklady*, 27(2):372–376, 1983.
- [58] A. Neubauer. On Landweber iteration for nonlinear ill-posed problems in Hilbert scales. *Numer. Math.*, 85(2):309–328, 2000.
- [59] A. Neubauer. Some generalizations for Landweber iteration for nonlinear ill-posed problems in Hilbert scales. *Journal of Inverse and Ill-posed Problems*, 24(4):393–406, 2016.
- [60] A. Neubauer. A New Gradient Method for Ill-Posed Problems. *Numerical Functional Analysis and Optimization*, 0(0):1–26, 2017.
- [61] A. Neubauer. On Nesterov acceleration for Landweber iteration of linear ill-posed problems. *J. Inv. Ill-Posed Problems*, 25(3):381–390, 2017.
- [62] S. Ogawa, T. M. Lee, A. R. Kay, and D. W. Tank. Brain magnetic-resonance-imaging with contrast dependent on blood oxygenation. *Proceedings of the National Academy of Sciences of the United States of America*, 87(24):9868–9872, 1990.
- [63] R. Ramlau. TIGRA - an iterative algorithm for regularizing nonlinear ill-posed problems. *Inverse Problems*, 19(2):433, 2003.

- [64] S. W. Rabkin. Arterial stiffness: Detection and consequences in cognitive impairment and dementia of the elderly. *Journal of Alzheimers Disease*, 32(3):541–549, 2012.
- [65] R. Ramlau. A modified Landweber method for inverse problems. *Numerical Functional Analysis and Optimization*, 20(1-2):79–98, 1999.
- [66] R. Ramlau. Regularization properties of Tikhonov regularization with sparsity constraints. *Electron. Trans. Numer. Anal.*, 30:54–74, 2008.
- [67] R. Ramlau and G. Teschke. A Tikhonov-based projection iteration for nonlinear ill-posed problems with sparsity constraints. *Numerische Mathematik*, 104(2):177–203, 2006.
- [68] A. Rieder. Inexact Newton Regularization Using Conjugate Gradients as Inner Iteration. *SIAM Journal on Numerical Analysis*, 43(2):604–622, 2005.
- [69] R. T. Rockafellar, M. Wets, and T. J. B. Wets. *Variational Analysis*. Grundlehren der mathematischen Wissenschaften. Springer Berlin Heidelberg, 2009.
- [70] K. Sagawa, R. K. Lie, and J. Schaefer. Translation of Otto Frank’s paper “Die Grundform des Arteriellen Pulses” *Zeitschrift für biologie* 37: 483-526 (1899). *Journal of Molecular and Cellular Cardiology*, 22(3):253–4, 1990.
- [71] O. Scherzer. Convergence Criteria of Iterative Methods Based on Landweber Iteration for Solving Nonlinear Problems. *Journal of Mathematical Analysis and Applications*, 194(3):911–933, 1995.
- [72] O. Scherzer. A convergence analysis of a method of steepest descent and a two-step algorithm for nonlinear ill-posed problems. *Numerical Functional Analysis and Optimization*, 17(1-2):197–214, 1996.
- [73] O. Scherzer, M. Grasmair, H. Grossauer, M. Haltmeier, and F. Lenzen. *Variational Methods in Imaging*. Applied Mathematical Sciences. Springer New York, 2008.
- [74] T. Schuster, B. Kaltenbacher, B. Hofmann, and K. S. Kazimierski. *Regularization Methods in Banach Spaces*. Radon series on computational and applied mathematics. De Gruyter, 2012.
- [75] E. Sherina and K. Knudsen. *Iterative Reconstruction Methods for Inverse Problems in Tomography with Hybrid Data*. PhD thesis, Technical University of Denmark, 2017.
- [76] R. Sladky, K. J. Friston, J. Troestl, R. Cunnington, E. Moser, and C. Windischberger. Slice-time effects and their correction in functional MRI. *NeuroImage*, 58:588–594, 2011.

- [77] M. K. Stehling, R. Turner, and P. Mansfield. Echo-planar imaging - magnetic-resonance-imaging in a fraction of a second. *Science*, 254(5028):43–50, 1991.
- [78] Y. J. Tong, L. M. Hocke, and B. D. Frederick. Short Repetition Time Multiband Echo-Planar Imaging with Simultaneous Pulse Recording Allows Dynamic Imaging of the Cardiac Pulsation Signal. *Magnetic Resonance in Medicine*, 72(5):1268–1276, 2014.
- [79] H. U. Voss, J. P. Dyke, K. Tabelow, N. D. Schiff, and D. J. Ballon. Mapping cerebrovascular dynamics with magnetic resonance advection imaging (MRAI): modeling challenges and estimation bias. *Meeting of the Society for Neuroscience*, 2015.
- [80] H. U. Voss, J. P. Dyke, K. Tabelow, N. D. Schiff, and D. J. Ballon. Magnetic resonance advection imaging (MRAI) of cerebrovascular pulse dynamics. *Journal of Cerebral Blood Flow and Metabolism*, 37:1223 – 1235, 2017.
- [81] H. U. Voss and N. D. Schiff. Searching for conservation laws in brain dynamics-BOLD flux and source imaging. *Entropy*, 16(7):3689–3709, 2014.
- [82] E. A. H. Warnert, K. Murphy, J. E. Hall, and R. G. Wise. Noninvasive assessment of arterial compliance of human cerebral arteries with short inversion time arterial spin labeling. *Journal of Cerebral Blood Flow and Metabolism*, 35(3):461–468, 2015.
- [83] E. C. Wong, R. B. Buxton, and L. R. Frank. Quantitative perfusion imaging using arterial spin labeling. *Neuroimaging Clinics of North America*, 9(2):333–342, 1999.
- [84] L. Yan, C. Y. Liu, R. X. Smith, M. Jog, M. I. Langham, K. Krasileva, Y. Chen, J. M. Ringman, and D. J. J. Wang. Assessing intracranial vascular compliance using dynamic arterial spin labeling. *NeuroImage*, 124, Part A:433–441, 2016.
- [85] X. Yu, Y. He, M. Wang, H. Merkle, S. J. Dodd, A. C. Silva, and A. P. Koretsky. Sensory and optogenetically driven single-vessel fMRI. *Nature Methods*, 13(4):337–40, 2016.
- [86] M. Zamir. *The Physics of Pulsatile Flow*. Biological physics series. AIP Press; Springer, New York, 2000.

Eidesstattliche Erklärung

Ich erkläre an Eides statt, dass ich die vorliegende Dissertation selbständig und ohne fremde Hilfe verfasst, andere als die angegebenen Quellen und Hilfsmittel nicht benutzt bzw. die wörtlich oder sinngemäß entnommenen Stellen als solche kenntlich gemacht habe. Die vorliegende Dissertation ist mit dem elektronisch übermittelten Textdokument identisch.

Linz, März 2018

Simon Hubmer

Curriculum Vitae

Name: Simon Hubmer

Nationality: Austria

Date of Birth: 20 March, 1993

Place of Birth: Wels, Austria

Education:

1999–2002

Elementary School
Volksschule GV2 Marchtrenk

2002–2010

High School, A-level with distinction
Bundesrealgymnasium Wels Wallererstraße

Oct. 2010
– Sept. 2013

Bachelor in Technical Mathematics, JKU Linz, with distinction
Bachelor Thesis: “Theorie von CreditRisk⁺”

Oct. 2013
– May 2015

Master in Industrial Mathematics, JKU Linz, with distinction
Master Thesis: “On Stopping Rules for Landweber Iteration for the Solution of Ill-Posed Problems”
Supervisor: Prof. Andreas Neubauer

Jun. 2015
– April 2018

PhD in Technical Sciences (Industrial Mathematics), JKU Linz
PhD Thesis: “Fast Gradient-Based Iterative Regularization Methods for Nonlinear Ill-Posed Problems - Theory and Applications”
Supervisor: Prof. Ronny Ramlau

Positions:

Jun. 2015
– March 2018

Research Assistant at the Doctoral Program “Computational Mathematics” and the Industrial Mathematics Institute, JKU Linz

Scientific Publications:

- S. Hubmer, R. Ramlau.
Convergence analysis of a two-point gradient method for nonlinear ill-posed problems.
Inverse Problems 33(9), 2017.
- S. Hubmer, A. Neubauer, R. Ramlau., H. Voss.
On the parameter estimation problem of magnetic resonance advection imaging.
Inverse Problems and Imaging 12(1):175–204, 2018.
- S. Hubmer, E. Sherina, A. Neubauer, O. Scherzer
Lame parameter estimation from static displacement field measurements in the
framework of nonlinear inverse problems.
SIAM Journal on Imaging Sciences, accepted 2018.
- S. Hubmer, R. Ramlau.
Nesterov’s accelerated gradient method for nonlinear ill-posed problems with a locally
convex residual functional.
Available from <https://arxiv.org/abs/1803.01757>, submitted 2018.
- S. Hubmer, K. Knudsen, C. Li, E. Sherina.
Limited angle electrical impedance tomography with power density data.
Available from <https://arxiv.org/abs/1712.08009>, submitted 2017.

Scientific Posters:

- S. Hubmer, A. Neubauer, R. Ramlau., H. Voss.
Inverse Problems and MRAI - Mapping the pulse wave velocity, *2nd International
Conference on Mathematical Neuroscience (ICMNS), Juan Le Pins, France*, May 2016.
- S. Hubmer, E. Sherina.
On the Inverse Problem of Linearized Elasticity, *100 Years of the Radon Transform
Workshop, Linz, Austria*, March 2017.
- S. Hubmer, E. Sherina.
On the Inverse Problem of Linearized Elasticity, *DTU PhD Bazaar, Lyngby, Denmark*
May 2017.
- S. Hubmer, A. Neubauer, R. Ramlau, H. Voss.
Fast Pulse Wave Velocity Estimation from Magnetic Resonance Imaging Data
Kepler Science Day, Linz, Austria, November 2017

Talks at Workshops, Conferences, and Universities:

- 09/2015 DK-Statusseminar, Strobl, Austria
03/2016 Inverse Problems in the Alps Minisymposium, Obergurgl, Austria

- 09/2016 Chemnitz Symposium on Inverse Problems 2016, Chemnitz, Germany
- 09/2016 DK-Statusseminar, Strobl, Austria
- 12/2016 IFIP WG 7.4 Workshop on Inverse Problems and Imaging, Mülheim
a.d. Ruhr, Germany
- 04/2017 HD Tomo Seminar, Technical University of Denmark, Lyngby, Denmark
- 05/2017 Applied Inverse Problems Conference, Minisymposium Discontinuity
Preserving Variational Methods in Imaging, Hangzhou, China
- 07/2017 DK-Mini-Workshop Computational Mathematics and Symbolic
Computation, Linz, Austria
- 08/2017 PCH60 Computational Inverse Problems - Insight and Algorithms
- 09/2017 DK-Statusseminar, Strobl, Austria
- 02/2018 DK Workshop Computational Mathematics in Numerical Analysis and
Symbolic Computation, Linz, Austria
- 03/2018 Inverse Problems in the Alps II, Obergurgl, Austria

Research Stays:

- Apr. 2017 **Technical University of Denmark**, visiting Prof. Per Christian Hansen
– May 2017
- Mar. 2018 **Technical University of Denmark**, visiting Prof. Kim Knudsen

Teaching:

- Fall 2015 **Tutorials** “Mathematics III” for Mechatronics Students
- Feb. 2016 **Project Instructor** at Project Week “Applied Mathematics”
for High School Students, Project: Numerical Methods
- Fall 2016 **Tutorials** “Mathematics I” for Chemistry Students
- Feb. 2017 **Project Instructor** at Project Week “Applied Mathematics”
for High School Students, Project: Differential Equations
- Fall 2017 **Tutorials** Integral Equations and Boundary Value Problems

Awards:

- 2013/14 **Merit-based Scholarship**, JKU Linz